CLIMATE MONITORING USING COLLOCATED AVHRR AND HIRS OBSERVATIONS
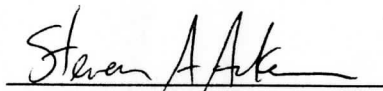
Final Report
National Oceanic and Atmospheric Administration
Climate and Global Change Program

Submitted by

Board of Regents of the University of Wisconsin System

on behalf of

Cooperative Institute for Meteorological Satellite Studies
Space Science and Engineering Center
at the University of Wisconsin-Madison
1225 West Dayton Street
Madison, Wisconsin 53706
608/262-0544

Steven A. Ackerman
Assistant Professor
Principal Investigator

SUMMARY

This two year grant supported the <u>development and testing</u> of an operational algorithm which combines observations from the AVHRR and HIRS/2 instruments with NMC forecast model temperature and moisture profiles to generate: global distributions of cloud altitudes and amount; the spectral radiative forcing of clouds; and the spectral greenhouse effect of water vapor. The algorithm was run in a real-time, hands-off mode for three months: July 1993, January 1994 and then again in July 1994. These three month tests using the NOAA-12 satellite demonstrated the operational nature of the algorithm. A brief description of the algorithm is given below. Some of the science results are detailed in the accompanying papers.

Algorithm Overview

The algorithm designed to operate in near-real time for the purpose of monitoring climate parameters and which makes use of collocated radiance measurements from the Advanced Very High Resolution Radiometer (AVHRR) and the High Resolution Infrared Sounder/2 (HIRS/2) is referred to as CHAPS - Collocated HIRS/2 and AVHRR ProductS. Observations from instruments aboard NOAA-12 space platform were used in conjunction with forecast model output from the National Meteorological Center (NMC) to produce global distributions of cloud altitude and amount, the spectral greenhouse effect of the atmosphere, and spectral cloud radiative forcing. *The feasibility of collocating measurements from two instruments and analyzing the combined data in near real-time was clearly demonstrated.* The technique discussed below can therefore be adapted into an operational algorithm or applied to historical data sets.

The spatial resolution of the HIRS/2 is nominally 17 km at nadir, while that of the AVHRR is 1 km. The present study utilized AVHRR Global Area Coverage (GAC) data, where every third scan-line was recorded and four of each five-pixel group along these scan lines were averaged, resulting in a nominal resolution of 4 km. The NOAA-12 space platform is in near-terminator sun-synchronous orbit with an inclination of approximately 110 degrees and height of 850 km. Such an orbit provides near-global coverage in 24 hours, with observations near 07:30 and 19:30 local time for most latitudes. This allows monitoring of day to day changes in clear-sky radiative properties due to variations in atmospheric moisture and temperature. This is particularly important in areas of the world which are otherwise very data-sparse.

The radiance data were acquired in near-real time from the Man-computer Interactive Data Access System (McIDAS) at the University of Wisconsin-Madison. Calibrated and navigated AVHRR and HIRS/2 measurements are stored on an IBM 4381 mainframe several hours after the completion of each orbit by the spacecraft. These data

sets remain on the computer for approximately 24 hours, until being overwritten by more recent observations. Global fields of vertical temperature and moisture profiles were obtained from the NMC in Camp Springs, MD. These "final analysis" fields are output for 0 and 12 hours UTC and are available approximately 10 hours later. Weekly global Reynolds' blended sea-surface temperatures (SSTs) were also received from the NMC.

Because of the tremendous volume of data, particularly from the AVHRR, processing had to be completed in a timely fashion to reduce the amount and cost of storage space. This was accomplished with the use of an IBM RISC 6000 computer. When new orbital data appeared on the mainframe, it was transferred to the RISC 6000 by use of the standard File Transfer Protocol (ftp) software. A pre-processing program was run periodically to ascertain which ancillary data sets would be needed (e.g. NMC profiles which would not be available for several hours), to match up the HIRS/2 and AVHRR orbital data sets, and to generate any other parameters necessary for processing. The input NMC temperature and moisture fields were linearly time-interpolated when necessary, to the nearest hour of the orbital start times. Such a scheme is adequate for processing over the ocean surface. This software acted as a funnel, gathering data from several machines, usually at several different times, and providing the main processing stream with all of the information needed to process one complete orbit.

The central and most CPU-intensive task of the data processor is the collocation of the AVHRR GAC pixels within the larger HIRS/2 footprints. The method described by Aoki (1980) was chosen, but where GAC data is used in place of the 1 km Local Area Coverage (LAC) type. This method has been used with good success by the present authors. Although the attempt was made to process as much data as possible, in order to minimize problems associated with limb measurements, sun glint, and angular effects on visible measurements, fields of view (FOVs) beyond 30 degrees of nadir were eliminated from the collocation. Also, poleward of 70 degrees latitude only one of four HIRS/2 FOVs was collocated with AVHRR pixels, due to the over sampling by polar orbiters in these regions. By restricting scan width, the amount of time needed to achieve truly global coverage is lengthened to two days, but any given geographical area is observed at least once for four consecutive days near the equator and more often nearer the poles. Even with the above restrictions, approximately 20,000 collocated HIRS/AVHRR FOVs were produced per orbit with about 30 AVHRR GAC observations for each HIRS/2. The collocated measurements (as well as all derived products) were mapped onto a 2.5 latitude equal-surface-area grid according to the International Satellite Cloud Climatology Project (ISCCP) binning scheme.

A check on the quality of the collocations is readily accomplished by comparison of the 11 micron window channel measurements of each instrument. Given that the atmosphere is nearly transparent at this wavelength, both instruments sense a wide variety of scene temperatures as the spacecraft progresses in its orbit. AVHRR pixel radiances were averaged over the corresponding HIRS/2 FOVs and converted to equivalent temperatures, then compared to those of the single HIRS/2 measurements. AVHRR data were also corrected for the known non-linearity of calibration in the three infrared channels. Correlations over an orbit were generally greater than 0.99.

Because it is convenient in terms of computer processing efficiency, three other algorithms are executed during the collocation step. First is the CO_2-slicing method of cloud altitude determination using five of the HIRS/2 infrared channels. This information is used as part of a quality control system for clear-sky determination later in the processing stream. Secondly, histograms of AVHRR pixel values for each of its five channels are produced for each ISCCP region viewed. The class widths are 0.5K for infrared channels and 1% for the visible. Only those pixels found to be located within HIRS/2 FOVs are incorporated into the histograms, which saves considerable amounts of computer time. Third, an estimate of total precipitable water at the location of each HIRS/2 FOV is computed based on spatially and temporally interpolated NMC temperature and moisture profiles.

PUBLICATIONS
Publications in Refereed Journals

Frey, R. A., S. A. Ackerman, and B. J. Soden, 1995: Climate parameters from satellite spectral measurements. Part I: Collocated AVHRR and HIRS/2 observations of the spectral greenhouse parameter. Accepted for the *Jour. Clim.*

Ackerman, S. A., 1994: Brightness temperature difference analysis of global satellite observations. Under revision for the *J. Atmos Sci.*

Ackerman, S. A., and K. I. Strabala, 1994: Satellite remote sensing of H_2SO_4 aerosol using the 8-12 μm window region: Application to Mount Pinatubo. *J. Geo. Res.* **99**, 18,639-18,649.

Papers Submitted or in Preparation

Ackerman, S. A., M. Kaestner, S. Pryzbylak, K. T. Kriebel and H. Mannstein, 1995: A comparison of cloud amounts derived from two satellite retrieval techniques..

Ackerman, S. A. and R. A. Frey, 1995: Climate parameters from satellite spectral measurements. Part II: Observations of spectral cloud forcing.

Conference Proceedings

Ackerman, S. A. and R. A. Frey, 1995: Climate parameters from collocated AVHRR and HIRS/2 observations: Clear-sky spectral greenhouse parameter. AMS Sixth Symposium on Global Change Studies. Dallas, Tx. 15-20 January.

Ackerman, S. A. and R. A. Frey, 1994: Cloud type indentification from collocated AVHRR and HIRS/2 observations. Conference on Passive Infrard remote Sensing of Clouds and the Atmosphere II. Rome, Italy. Sept. 26-30.

Ackerman, S. A., and R. A. Frey, 1994: Real time analysis of Collcoated AVHRR and HIRS/2 Observations. Seventh Conference on Satellite Meterology and Oceanography.

Ackerman, S. A., R. A. Frey, C. Moeller, K. I. Strabala, W. P. Menzel and W. L. Smith, 1994: Negative 11 micron minus 12 micron brightness temperature differences; instrument calibration of reality. Seventh Conference on Satellite Meterology and Oceanography.

Ackerman, S. A. and R. A. Frey, 1994: Climate monitoring using collocated AVHRR and HIRS/2 observations. AMS Eighth Conference on Atmospheric Radiation. Jan. 23-27, Opryland, TN.

Ackerman, S. A. and K. Strabala, 1994: Monitoring the Mt. Pinatubo aerosol with HIRS/2 observations.. AMS Eighth Conference on Atmospheric Radiation. Jan. 23-27, Opryland, TN.

Ackerman, S. A., R. A. Frey, W. L. Smith, W. P. Menzel and C. M. Hayden, 1993: Use of collocated AVHRR and HIRS/2 measurements as an approach to global climate monitoring. IAMAP and IAHS Joint International Meeting, July 11-23 Yokohama, Japan.

A Comparison of Cloud Amounts Derived from Two Satellite Retrieval Techniques

S. A. Ackerman[1], M. Kästner[2], S. Przybylak[2], K. T. Kriebel[2], H. Mannstein[2] and R. A. Frey[3]

[1]Department of Atmospheric and Oceanic Sciences
[3]Cooperative Institute for Meteorological Satellite Studies
University of Wisconsin
Madison WI, 53706

[2]Deutsche Forschungsanstalt für Luft- und Raumfahrt
Institute of Atmospheric Physics
Oberpfaffenhofen, FRG

ABSTRACT

This paper presents a quantitative comparison of two cloud detection techniques using satellite observations. The AVHRR (Advanced Very High Resolution Radiometer) Processing scheme Over cLoud Land and Ocean (APOLLO) makes use of five spectral channels with a spatial resolution of 1.1 km. The Collocated HIRS/2 and AVHRR ProductS (CHAPS) operates with more spectral channels but at lower spatial resolution. Both techniques have been designed to work in an automated mode, collecting and analyzing satellite data in real-time. Major differences between the two methods include sub- sampling of the AVHRR pixels by CHAPS, inclusion of HIRS/2 observations by CHAPS, and differing approaches in selecting clear radiance thresholds.

Over oceans, the agreement in total cloud cover between the two satellite techniques is very good (r=0.92). Application of a dependent sample *t*- test to the two cloud amount data sets indicates that there is a greater than 99.9% probability that the two samples were drawn from the same population. This demostrates that the subsampling of AVHRR pixels in the CHAPS processing is appropriate for deriving cloud amounts over a 2.5 degree oceanic region. For such a region, there is a tendancy for CHAPS to derive higher cloud amounts than APOLLO. This is attributed to differences in clear-sky radiance thresholds derived from the CHAPS spatial variability test.

2

Over land, the derived cloud amount products from the two methods are considerably different. The CHAPS product is an effective cloud amount, defined for each HIRS field of view, which is the product of cloud fraction and cloud emissivity, rather than a simple areal percentage. Also, the HIRS/2 footprint size (17 km at nadir) is much larger than that of the AVHRR. There is a good correlation of the two cloud products (r=0.82); however, a t-test indicates the two techniques are deriving fundamentally different parameters. This is consistent with the above differences.

To reference the satellite derived cloud amounts to more traditional observations, APOLLO results are compared with surface observations of cloud amount. The APOLLO cloud amount and surface observations of cloud cover are generally within ±5%.

Recommendations for improving the two cloud retrieval techniques are suggested.

3

1 Introduction

Radiance measurements from meteorological satellites provide the best means of routinely monitoring the global distribution of various climate parameters. One such parameter is cloud amount. Various approaches to cloud detection using satellite data have been developed (Smith and Platt, 1978; Coakley and Bretherton, 1982; Liljas, 1984; Arking and Childs, 1985; Saunders and Kriebel, 1988; Stowe et al, 1991; Derrien at al 1993). The most comprehensive effort so far is the International Satellite Cloud Climatology Project (ISCCP) (Rossow and Gardner, 1993a and b) which derives cloud cover and cloud optical depth on a global scale using observations from multiple satellites.

Verification of satellite derived cloud parameters is a complex task due to difficulties in establishing "ground truth" values. There are three basic steps in validating a cloud retrieval algorithm from satellite observations:

(1) Empirical image analysis is based on the visual inspection of a cloud masked image, with comparisons to images of various satellite spectral channels (Simpson and Humphrey, 1990). This validation proceedure is important in the development of a cloud detection algorithm as it provides a human interpretation of over-all performance.

(2) Validation is also accomplished through comparisons of satellite estimates with surface based observations (Smith and Platt, 1978; Platt et

4

al 1980; Ackerman and Cox 1981; Ackerman and Cox, 1987, Rossow and Gardner 1993c) or aircraft observations (Kriebel et al 1989; Kästner et al 1993). Comparisons with aircraft observations or ground-based active sensors are often limited to case studies and are not straight forward due to variations in the physical definition of what is a cloud, and differences in the volume of the atmosphere sampled.

(3) Comparing the results of different satellite retrieval schemes (Rossow and Gardner, 1993c) is another method of validation. As with the satellite versus surface or aircraft comparisons, an intercomparison between two satellite techniques provide a tool for understanding the strengths and weaknesses of each retrieval approach.

This study compares derived cloud amounts from two satellite algorithms. In addition, one of the techniques is compared with surface observations. The objective of these comparisons was to determine the consistency between the two techniques and to identify potential problems with the algorithms. An overview of the algorithms is presented in Section 2. In the first comparison (Section 3.3) the two methods are applied to ocean scenes. Section 3.4 presents a comparison of results from the operational runs of the two algorithms of land. Potential improvements and conclusions are presented in Section 4.

2 Algorithm Overviews

This section presents a brief overview of the two cloud retrieval schemes used in the study. Specific details of the algorithms can be found in the references cited.

2.1 APOLLO

The AVHRR Processing scheme Over cLoud Land and Ocean (APOLLO) has been discussed in detail by Saunders and Kriebel (1988), Kriebel et al (1989) and Gesell (1989). The scheme uses AVHRR channels 1 through 5 at full spatial resolution, nominally 1.1 km at nadir. The 5 spectral bandpasses are approximately 0.58-0.68μm, 0.72-1.10μm, 3.55-3.93μm, 10.3- 11.3μm and 11.5-12.5μm. The technique is based on 5 threshold tests. A pixel is called cloudy if it is brighter or colder than a threshold, if the reflectance ratio of channels 2 to 1 is between 0.7 and 1.1, if the temperature difference between channel 4 and 5 is above a threshold, and if the spatial uniformity over ocean is less than a threshold (Kriebel et al, 1989). The pixel is defined as cloud contaminated if it fails any single test. Two of those tests are then used with different thresholds to identify fully cloudy pixels from the partially cloud contaminated ones (Kriebel et al, 1989). During daytime, AVHRR channel 3 reflectance is used to help discriminate between water and ice clouds. During night time, a different scheme is applied which makes use of temperature differences between the 3 IR channels. Cloud

6

cover is derived from all pixels, whereas cloud optical properties are derived from fully cloudy pixels only (Kriebel et al, 1989). The derivation of cloud radiative properties is based on parameterizations which relate the channel 1 reflectance to optical depth in case of water clouds and to IR emissivity in case of ice clouds. Liquid/ice water path is also derived. Validations with airborne in situ data show uncertainties in the derived liquid water path of approximately 30% (Kriebel, 1989).

2.2 CHAPS

A near real-time algorithm to derive climate parameters using collocated HIRS/2 (High-resolution InfraRed Sounder) and AVHRR observations has been developed and implemented at the Cooperative Institute of Meteorological Satellite Studies (CIMSS). The Collocated HIRS/2 and AVHRR ProductS (CHAPS) combines observations from the AVHRR and HIRS/2 instruments with NMC (National Meteorological Center) analysis fields to derive the global distribution of various climate products (e.g., global distributions of cloud altitudes and amount; the spectral radiative forcing of clouds; and the spectral greenhouse effect). CHAPS was developed not only to determine cloud amount and cloud type, but also for investigating their impact on the radiative energy budget, a fundamental climate parameter.

Many algorithms have been developed for analyzing observations of the AVHRR instruments (e.g., cloud coverage and Normalized Difference Vege-

tation Index). The main advantage of the AVHRR is its high spatial resolution. Its five channels are in spectral regions where atmospheric absorption is weak and therefore the AVHRR is often applied to surface studies and cloud and aerosol detection. Nearly as many algorithms have been developed for the HIRS/2 data stream. The advantage of the HIRS/2 is not its spatial resolution, approximately 17 km at nadir, but rather its multi-spectral observations. HIRS/2 spectral channels (19 infrared and 1 visible) were selected to study atmospheric characteristics (e.g., temperature and moisture retrievals). By collocating the AVHRR pixels within the larger HIRS/2 footprint, we take advantage of the strength of each instrument to derive an enhanced climate product. CHAPS incorporates many of the published algorithms for cloud detection. A detailed description of the clear-sky radiance retrieval is discussed in Frey et al (1994).

The AVHRR and HIRS/2 collocation is based on the method described by Aoki (1980). The collocation analysis id performed daily for each satellite orbit. To reduce the amount of data processed and to minimize problems associated with limb measurements, FOVs beyond 30 degrees of nadir were eliminated from the collocation procedure. The cloud type classification combines a variety of well-known approaches, such as the split window, CO_2-slicing (Smith and Platt 1978) and spatial variability, along with new methods based on 8, 11 and 12 micron observations (Strabala et al 1994). Over oceans, CHAPS makes use of AVHRR single-pixel information to derive a clear-sky threshold and a total cloud cover product. If the

8

CO_2-slicing method detects a cloud top pressure less than 500 mb, than an effective cloud amount (the product of emissivity and cloud amount) is derived from the HIRS/2 observations. The CHAPS analysis scheme was run in near-real time for the months of July 1993 and January and July 1994. While CHAPS global processing makes use of GAC (Global Area Coverage) data, the algorithm can also be applied to the LAC (Local Area Coverage) data. The LAC data is the full spatial resolution AVHRR data with a 1.1 km FOV at nadir. The GAC data resolution is often referred to as 4 km resolution as it is derived by averaging 4 out of 5 LAC pixels on every third scan line. Over land, CHAPS relies heavily on the CO_2 slicing approach (Wylie et al 1994).

3 Comparison Results

3.1 Satellite Algorithm Differences

There are fundamental differences between CHAPS and APOLLO that need to be remembered in the comparisons presented below.

(a) CHAPS operates at the 17 km pixel resolution of the HIRS/2 instrument and analyzes only AVHRR pixels that lie within those footprints. As the HIRS/2 FOVs do not overlap, spacing is approximately 30 km, CHAPS does not make use of all the AVHRR observations in a given scene. APOLLO's fundamental resolution is 1.1 km, and it makes use of all AVHRR pixels within the specified scene.

9

(b) CHAPS relies mostly on the infrared channels of the AVHRR and HIRS/2 collocated data. A visible reflectance threshold test is conducted by CHAPS only over the ocean regions, while APOLLO makes use of visible thresholds tests as well as the ratio of reflectances between channel 2 and channel 1 (Saunders and Kriebel 1988).

(c) While both techniques use AVHRR observations, CHAPS incorporates collocated HIRS/2 observations.

(d) CHAPS was designed for global application while APOLLO was developed for regional applications.

3.2 Comparison of APOLLO with Surface Observations

Before comparing the two satellite cloud retrievals, it is worthwhile to compare APOLLO derived cloud amounts with conventional surface observations. It is difficult to compare CHAPS derived cloud amounts with surface observations because of the large FOV of the HIRS/2 instrument. Through this analysis we attempt to establish APOLLO as a reference in the comparison with CHAPS. Figure 1 displays the geographic location of 25 German synoptic weather stations where open circles, triangles and filled circles represent land, mountain and city locations, respectively. The monthly mean cloud amount from these surface stations during July 1993 and January 1994 were compared to the APOLLO derived cloud amount over a 15 km

10

grid interval. The results are shown in Figure 2, where the symbols represent the surface types as noted in the legend. The very good agreement between the two cloud cover products is demonstrated in Figure 3, which shows a histogram of the surface cloud amount minus the APOLLO cloud amount. APOLLO has a slightly higher, 4.5%, mean cloud cover amount. The majority of the differences in cloud amount are within ±5%, with a skew towards larger APOLLO cloud amounts. The APOLLO derived cloud cover is greater in January than July, in agreement with seasonal changes observed at the surface (Branicki, 1963).

3.3   Ocean Scene Comparisons of APOLLO and CHAPS

In this section, APOLLO and CHAPS algorithms are applied to oceanic scenes, and cloud amounts derived over 2.5 degree regions. We have chosen ocean scenes in this first comparison to simplify the retrievals, as ocean surfaces are generally more uniform than land surfaces. In addition, CHAPS currently focuses on water regions, making the inter- comparisons more appropriate. In deriving clear-sky thresholds over oceans, both CHAPS and APOLLO make use of threshold, histogram and spatial variability tests using the AVHRR data. Thus, one would expect to see similar cloud amounts from the two techniques. APOLLO processes every pixel while CHAPS subsamples, so this comparison will indicate the potential impact of the CHAPS subsampling on the 2.5° grid mean cloud cover estimates.

CHAPS uses the AVHRR pixels within the HIRS/2 FOV to derive a total cloud amount, in addition to the effective cloud amount derived using the HIRS/2 15 μm CO_2 channels (Menzel et al 1994). Emphasis is put on comparisons of total cloud amounts derived by the two algorithms at the AVHRR pixel level.

Figure 4 depicts a comparison between APOLLO and CHAPS total cloud amounts for Pacific ocean regions viewed by the NOAA-10 satellite in July 1987. Each point represents an average cloud amount over a 2.5 degree grid box. Agreement is very good, with a correlation coefficient of 0.92. A histogram summary of the cloud amounts is depicted in Figure 5. Averaging the individual 2.5 degree scenes together, CHAPS results in a mean cloud cover of 89.9% ±10.5 and APOLLO yields 87.3% ±10.9. The 95% confidence intervals of the mean, which gives us the range of values where the "true" mean is located, is 86.4-93.3 percent for CHAPS and 83.7-91.0 for APOLLO. Thus the means of each algorithm lie within the 95% confidence levels of the others. A dependent sample t-test was applied to the two cloud amount data sets, indicating that there is greater than a 99.9% probability (p-level less than 0.001) that the two samples were drawn from the same population. This demostrates that the subsampling in the CHAPS processing of AVHRR pixels is appropriate for deriving cloud amounts over a 2.5° oceanic region. This is an important result in that CHAPS was designed for global processing, and subsampling allows a substantial reduction in processing time and data storage.

12

Figure 4 demonstrates that over the 2.5° region, CHAPS' cloud amounts are greater than APOLLO's. These differences are not solely attributed to the AVHRR subsampling of the CHAPS; it suggests the two techniques are deriving slightly different cloud threholds. Over ocean scenes, both algorithms make use of spatial variability tests for cloud threshold detection. APOLLO scene uniformity tests are applied to 3×3 groups of pixels. Figure 6a is an example of a spatial variability test using such groups. Clear-sky scenes are found in these very cloudy regions where 3×3 groups of radiance measurements are both warm and show little variance. CHAPS, because of its interest in detecting clear-sky HIRS/2 footprints needed for the spectral greenhouse parameter and spectral cloud forcing (Frey et al, 1994), conducts spatial variability tests at that resolution. That is, uniformity tests are applied by averaging all AVHRR pixels within a HIRS/2 footprint (more than 200 of the 1 km pixels). Figure 6b is similar to Figure 6a, but shows the results of the CHAPS variability test over the same region. Due to larger spatial averaging associated with Figure 6b, the standard deviations over the HIRS/2 FOV are generally greater than the 3×3 grouping of APOLLO. The effect, is to define a uniform scene at the HIRS/2 spatial scale that may include some clouds. The result, is CHAPS selects an AVHRR clear-sky radiance threshold that is slightly colder than APOLLO, and thus produces a higher cloud amount. In addition, since APOLLO processes all pixels within the scene, it has a higher probability of finding

13

a uniform scene than CHAPS, which processes only those AVHRR pixels that lie within a HIRS/2 footprint.

3.4 Comparison of Operationally Derived Products

Since September 1991, the APOLLO scheme has been retrieving cloud properties over a region which includes the Alps (44.25N to 49.25N latitude by 6.4E to 13.6E longitude). One of the APOLLO derived operational products for this region is total cloud amount at a spatial scale of approximately 15 km. In operational mode, APOLLO works with observations from the mid-afternoon NOAA polar orbiting satellite (e.g., NOAA-11).

CHAPS has been applied to global NOAA-12 data during July 1993, January and July 1994. CHAPS focuses on deriving climate parameters over oceanic regions. Over land, CHAPS currently relies heavily on the CO_2-slicing algorithm, similar to Wylie et al (1994). In the analysis that follows, the collocated AVHRR data are used by CHAPS in a simplified method to assess the uniformity of the HIRS/2 footprints in an attempt to improve clear-sky determination. For example, during summer, if the HIRS/2 $11\mu m$ brightness temperature is 8 or more degrees warmer then the National Meteorological Center (NMC) surface analyzed temperature, and the variation of the AVHRR collocated channel 4 pixels is less than 1.5K, the scene is assumed to be completely clear. This test is not applied over mountainous regions, such as the Alps, where large variations in

surface temperature can be expected. Unlike the analysis of ocean scenes, CHAPS currently does not derive a total cloud amount over land using the individual AVHRR pixels.

In this section, we compare the APOLLO retrieval of monthly mean total cloud cover for this geographic region with a similar product derived from CHAPS, the effective cloud amount derived from the CO_2-slicing method. Both cloud cover products were derived from the automated runs of the two algorithms. The APOLLO scheme used data from the NOAA-11 mid-day overpasses, while CHAPS processed both ascending and descending node of the NOAA-12. There are time differences in the two schemes due to the use of different satellite platforms. This may impact the comparisons if there is a large diurnal variation in cloud amount. In addition, due to diurnal variations in surface properties, we cannot make direct comparisons of clear-sky radiances. A 60 year analysis of surface observed cloud amounts in Germany (Branicki, 1963) indicates that the diurnal differences in cloud amount during these time periods should be less than $\pm 10\%$.

Due to the large footprint size of the HIRS/2 and because of the limitation in view angle applied by CHAPS, it is not possible to re-sample CHAPS at the high spatial resolution of the APOLLO. Thus the results of the two algorithms were averaged over a 0.5° latitude by 1° longitude grid. As the CHAPS relies mostly on the CO_2-slicing method over land, the APOLLO cloud amounts are compared with the CHAPS effective cloud amounts, defined as the product of cloud amounts and cloud emissivities. Results of

15

the comparison are shown in Figure 7. Circles represent comparisons for the month of July (open circles for 1993, filled circles for July 1994), while the stars are results from January 1994. The ellipse, oriented along a linear regression between the two cloud products, denotes the 95% confidence level. The small circles on the right axis denote the CHAPS retrieved effective cloud amounts while those on the top represent the APOLLO cloud amounts. These small circles allow one to easily compare the cloud distributions of the two techniques (e.g., maximum, minimum and median values). As expected, the CHAPS effective cloud amounts are generally less than the APOLLO derived cloud amounts. The CHAPS effective cloud amount ($N\varepsilon$) is derived from the HIRS/2 11μm window radiance using

$$I_{meas} = I_{clear} - N\varepsilon(I_{clear} - I_{cloud})$$

where I_{clear} and I_{cloud} are the clear-sky and cloud radiances respectively. The cloud radiance is determined from the CO_2 slicing derived cloud temperature and the Planck function. Since the cloud emissivity is less than or equal to 1, the effective cloud amount of the CHAPS should be less than the APOLLO derived cloud amount. Another factor contributing to the smaller CHAPS cloud amounts is the different techniques used by the two cloud retrieval algorithms. Over land, CHAPS relies solely on infrared tests. APOLLO, on the other hand, uses infrared and visible tests in its cloud detection over land. The visible tests are useful for detecting low

level clouds where the temperature difference between the cloud and surface is small. In addition, the higher spatial resolution of APOLLO allows for better detection of small clouds.

The linear correlation coefficient between the two samples is 0.81. The average difference between the two techniques is approximately 24%, which cannot be explained solely as a result of the different sampling times of the two satellites. Based on 60 years of surface observations (Branicki, 1963) in Germany, the expected diurnal differences in the monthly mean cloudiness induced by the different satellite overpasses is less than ±10% in July and ±5% in January. Another notable feature of Figure 7 is the difference in the range of cloud amounts derived by the two techniques. The APOLLO cloud amount ranges from approximately 30%-95% while the CHAPS ranges from 5% to 90%. The mean cloud amount from these months is 48.6% and 72.9%, with the 95% confidence intervals of 45.6-51.7 and 71-74.8 % for CHAPS and APOLLO respectively. The means of each data set lie well outside the expected mean of the other. Applying a t-test for independent samples to test the significance of this difference between the means of the two samples of observations, demonstrates that it is highly significant (>99%). Thus while the two data samples are correlated, the cloud properties that are inferred are different (e.g., cloud amount versus effective cloud amount).

A histogram of the frequency of occurrence of total cloud amount in categories of 5% is shown in Figure 8. As with the means, the CHAPS

median value is approximately 22% smaller than APOLLO. The CHAPS also has a larger standard deviation (19% versus 12%) and a larger range. The mean and median values of each technique are similar. Both techniques are skewed to smaller cloud amounts, though APOLLO has a larger skew towards smaller cloud amounts. The smaller cloud amounts are generally associated with the summer observations.

It is worthwhile to note that while there are large significant differences between the means, the two techniques have similar month-to-month variations. This is demonstrated in a box-whisker diagram (Figure 9) where the points represent the monthly mean cloud amount of the region (circles – CHAPS and squares – APOLLO) and the whiskers are ± 2 standard deviations about the mean. Both techniques have a larger cloud amount in January than in July, in agreement with surface observations of cloud amount. Both approaches have largest variability during the month of July 1994.

4 Summary

A quantitative comparison of cloud amounts derived from two satellite cloud detection techniques is presented. APOLLO makes use of five spectral channels of the AVHRR with a spatial resolution of 1.1 km. The APOLLO cloud detection tests treat each pixel separately. Neighbors are considered only in the case of the spatial uniformity test. CHAPS performs similar

18

infrared tests as APOLLO, but includes more spectral channels by combining AVHRR observations with lower spatial resolution HIRS/2 (17 km at nadir) data. Both techniques have been designed to work in a real-time analysis mode.

A comparison of APOLLO derived total cloud amount with surface observations showed most differences being within ±5%.

When applied to 2.5° latitude and longitude ocean scenes containing stratus, there is excellent agreement (r=0.92) in total cloud cover between the two satellite techniques. A dependent sample t-test was applied to the two cloud amount data sets, indicating that there is greater than a 99.9% probability that the two samples were drawn from the same population. Thus, for global monitoring of cloud amount over oceans, processing only AVHRR pixels within the HIRS/2 FOV should not bias the CHAPS cloud amount results. While the means of each algorithm were within the 95% confidence levels of the other's, CHAPS tends towards higher cloud amounts for each 2.5° ocean region. This results from conducting the CHAPS spatial variability tests over a larger region (HIRS/2 FOV) than the APOLLO (3×3 pixels).

Over land regions, CHAPS tended to produce a lower cloud amount, which was expected given that it actually derives an effective cloud amount (the product of cloud amount and cloud emissivity). There is a good correlation of the two satellite cloud products; however, a histogram analysis and

t-test implies that the two techniques are retrieving fundamentally different parameters. This is due to differences between spatial and spectral resolutions of the cloud detection techniques. While the two retrieval techniques result in different cloud amounts over land, they do capture the differences in the three months analyzed. Both have larger cloud amounts in January than in July, which is in agreement with surface based observations (e.g., Branicki, 1963).

These comparisons suggests the following improvements to CHAPS processing:

- Clear-sky thresholds using spatial variability tests can be improved by conducting the averaging over a smaller region than the HIRS/2 FOV. Groups of 3×3 pixels within the HIRS/2 FOV can be used to set the thresholds in future applications.

- Incorporating APOLLO's AVHRR cloud detection test using the ratio of channel 2 to channel 1. Currently CHAPS uses a simple threshold on the reflectance in channel 2.

- CHAPS over land should make use the collocated AVHRR pixel values independent of the HIRS/2 analysis, similar to APOLLO processing.

5   References

Ackerman, S. A., and S. K. Cox, 1981: Comparison of satellite and all-sky camera estimates of cloud cover during GATE. J. Appl. Meteor., 20, 581-587.

Ackerman, S. A., and S. K. Cox, 1987: Radiative energy budget estimates for the 1979 southwest summer monsoon. *J. Atmos. Sci.*, 44, 3052-3078.

Arking, A. and J.D.Childs, 1985: Retrieval of cloud cover parameters from multispectral satellite images, *J. Clim. Appl. Meteor.*, **24**, 322-333.

Aoki, T., 1980: A method for matching the HIRS-2 and AVHRR pictures of TIROS-N satellites. *Meteorological Satellite Center Tech. Note 2*, Tokyo, Japan, 15-26.

Branicki, O., 1963: Das Klima von Potsdam. Ergebnisse 60jähriger Beobachtungen am Meteorologischen Observatorium 1893-1952. Meteorologische Abhandlungen, **32**, Freie Universifät Berlin, pp.123.

Coakley, J. A. and F.P.Bretherton. 1982: Cloud cover from high-resolution scanner data: Detecting and allowing for partially filled fields of view, *J. Geophys. Res.*, **87**, 4917-4932.

Derrien, M., B.Farki, L.Harang, H.LeGleau, A.Noyalet, 1993: Automatic Cloud Detection Applied to NOAA-11/AVHRR Imagery. *Remote Sens. Environ.*, **46**, 246 - 267.

Frey, R. A., S. A. Ackerman and B. J. Soden, 1994: Climate Parameters from Satellite Spectral Measurements Part I: Collocated AVHRR and HIRS/2 Observations of Spectral Greenhouse Parameter. Submitted to the *J. Climate*.

Gesell, G., 1989: An algorithm for snow and ice detection using AVHRR data: An extension to the APOLLO software package, *Int. J. Remote Sens.*, **10**, 897-905.

Kästner,M., K.T.Kriebel, R.Meerkoetter, W.Renger, G.H.Ruppersberg, and P.Wendling, 1993: Comparison of cirrus height and optical depth derived from satellite and aircraft measurements, *Mon. Wea. Rev.*, **121**, 2708-2717.

Kriebel, K. T., 1989: Cloud liquid water path derived from AVHRR data using APOLLO, *Int. J. Remote Sens.*, **10**, 723-729.

Kriebel, K. T., R.W.Saunders and G.Gesell, 1989: Optical properties of clouds derived from fully cloudy pixels, *Contrib. Phys. Atmos.*, **62**, 165-171.

Liljas,E., 1984: Processed satellite imageries for operational forecasting. *Swedish Space Corporation*, 43 pp.

Platt,C. M. R., D.W.Reynolds, and N.L.Abshire, 1980: Satellite and lidar observations of the albedo, emittance and optical depth of cirrus compared to model calculations, *Mon. Wea. Rev.*, **108**, 195-204.

Rossow, W. B. and L. C. Garder, 1993a: Cloud detection using satellite measurements of infrared and visible radiances for ISCCP. *Jour. Climate*, **6**, 23341-2369.

Rossow, W. B., and L.C.Garder, 1993b: Validation of ISCCP cloud detections, *J. Clim.*, **6**, 2370-2393.

Rossow, W. B., A.W.Walker, and L.C.Garder, 1993: Comparison of ISCCP and other cloud amounts, *J. Clim.*, **6**, 2394-2418.

Saunders, R. W., and K.T.Kriebel, 1988: An improved method for detecting clear sky and cloudy radiances from AVHRR data, *Int. J. Remote Sens.*, **9**, 123-150.

Simpson, J. J., and C. Humphrey, 1990: An automated cloud screening algorithm for daytime Advanced Very High Resolution Radiometer imagery, *Jour. Geo. Res.*, **95**, 13,459-13,481.

Strabala, K. I., S. A. Ackerman and W. P. Menzel, 1994: Cloud properties inferred from 8-12 μm data, *Jour. App. Met.*, **2**, 212-229.

Stowe, L. L., McClain, E. P. Carey, R., et al. 1991: Global distributions of cloud cover derived from NOAA/AVHRR operational satellite data. *Adv. Space Res.*, **11**, 51-54.

Smith, W. L., and C. M. R. Platt, 1978: Intercomparison of radiosonde, ground based laser and satellite deduced cloud heights. *J. Appl. Meteor.*, **17**, 1796-1802.

Wylie, D.P., Menzel, W.P., H. M. Woolf and K.I. Strabala, 1994: Four years of global cirrus cloud statistics using HIRS. *Jour. Climate.*
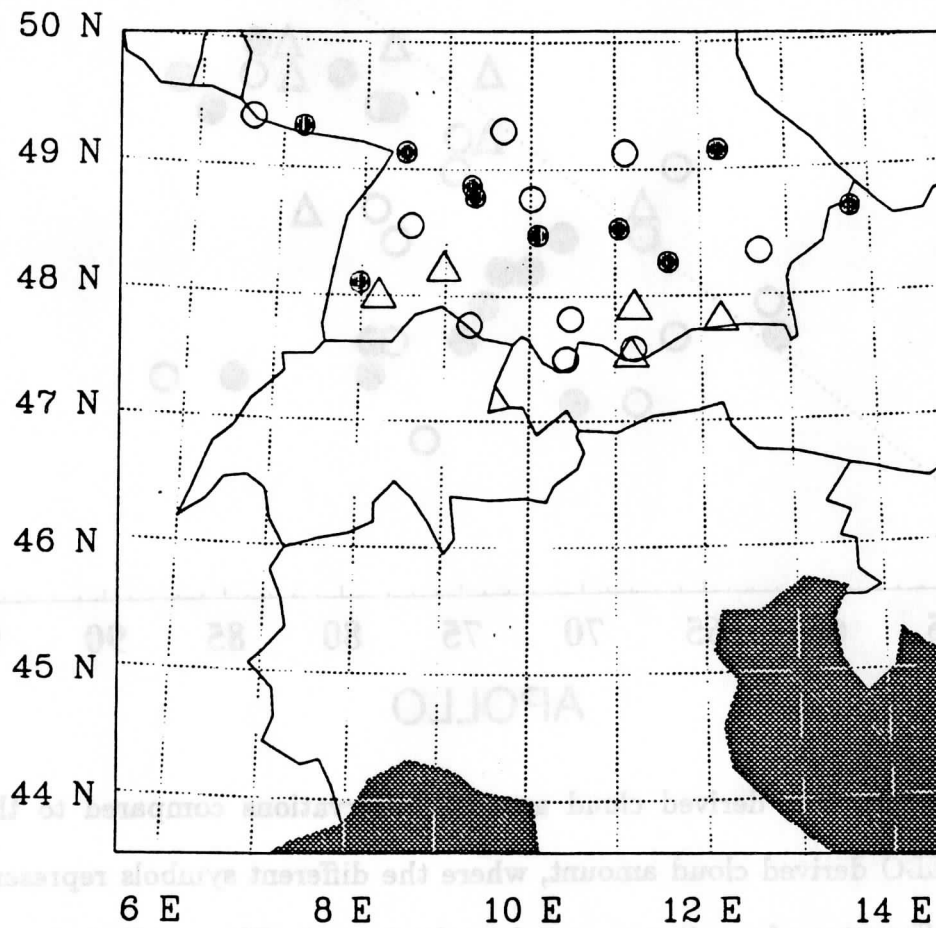
6   List of Figures

Figure 1. Geographic location of 25 German weather stations where circles, triangles and filled circles represent rural, mountain and city locations, respectively.
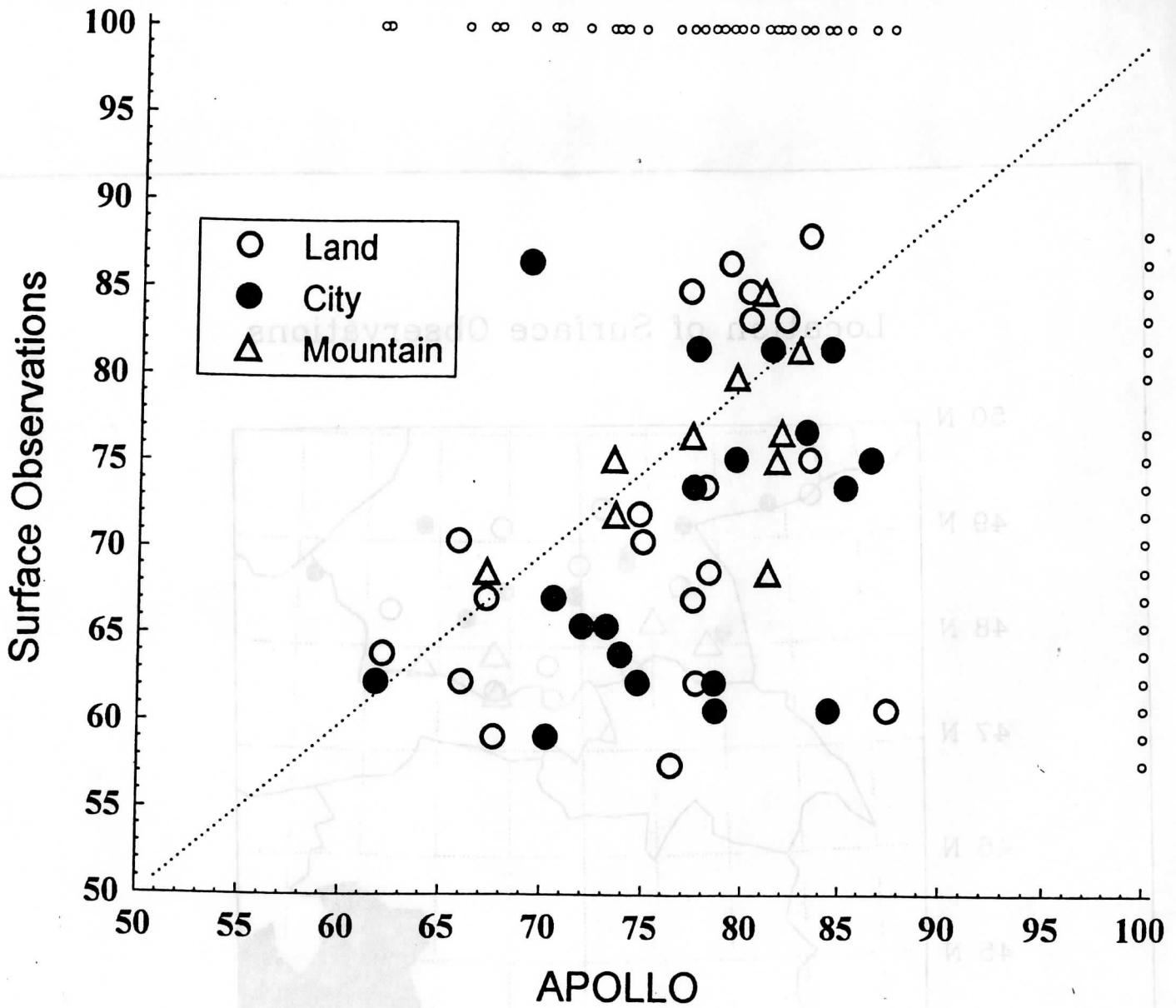
Figure 2. Surface derived cloud amount observations compared to the APOLLO derived cloud amount, where the different symbols represent the different surface sites as noted in the legend. The small circles on the right axis denote the surface cloud amounts while those on the top represent the APOLLO total cloud amounts.
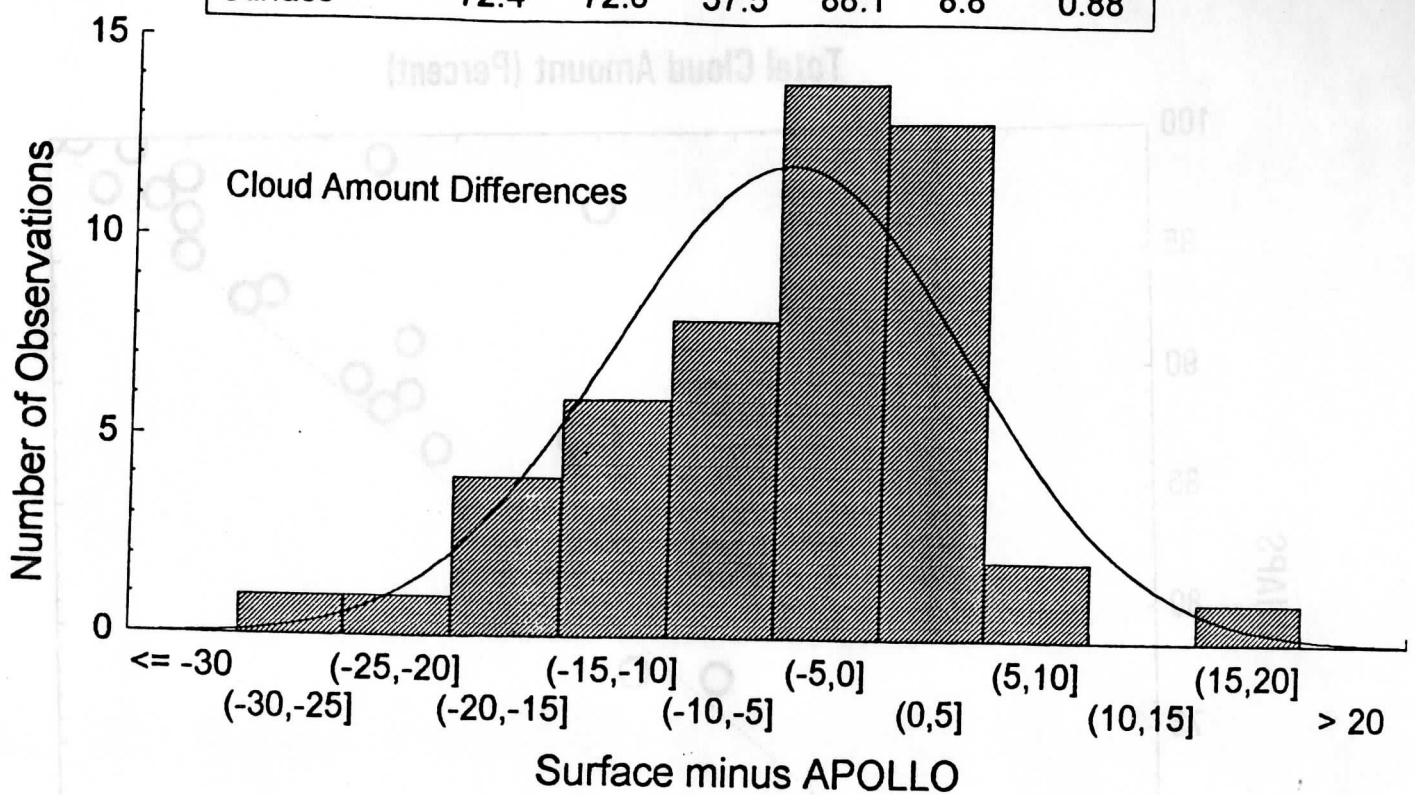
Figure 3. Histogram analysis of the surface cloud amount minus the APOLLO cloud amount. Also shown is a least squares fitted normal curve.
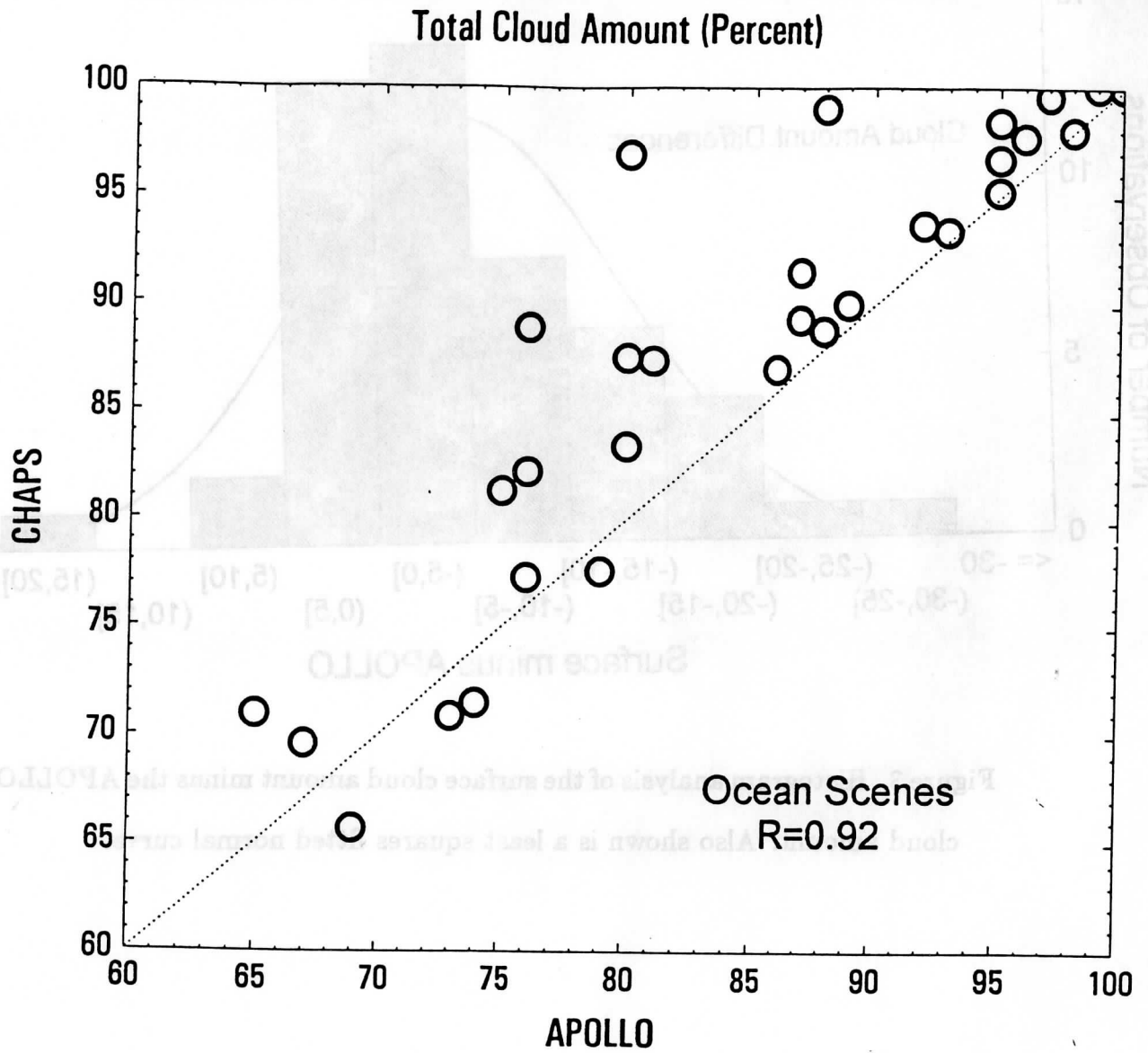
Figure 4. Comparison of APOLLO and CHAPS total cloud amount for the Pacific ocean regions. Each point represents an average cloud amount over a 2.5 degree grid box.
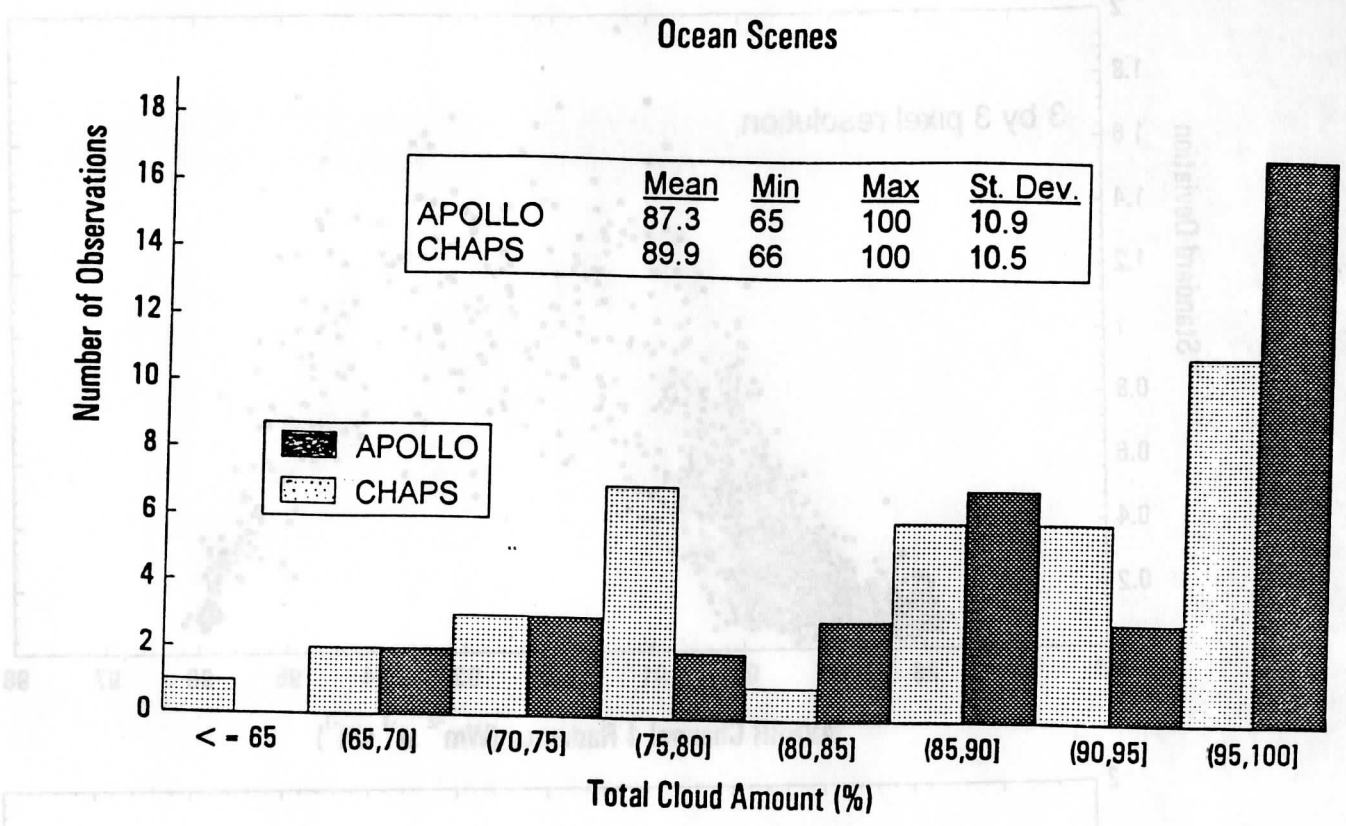
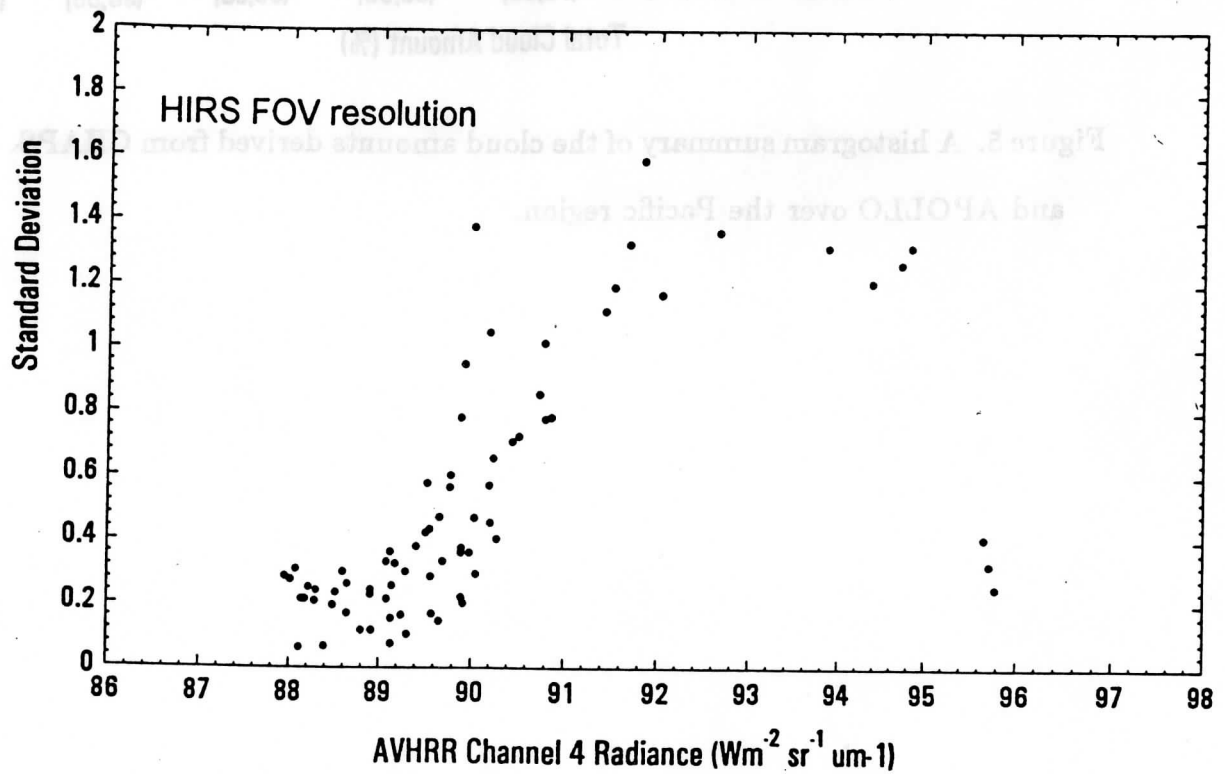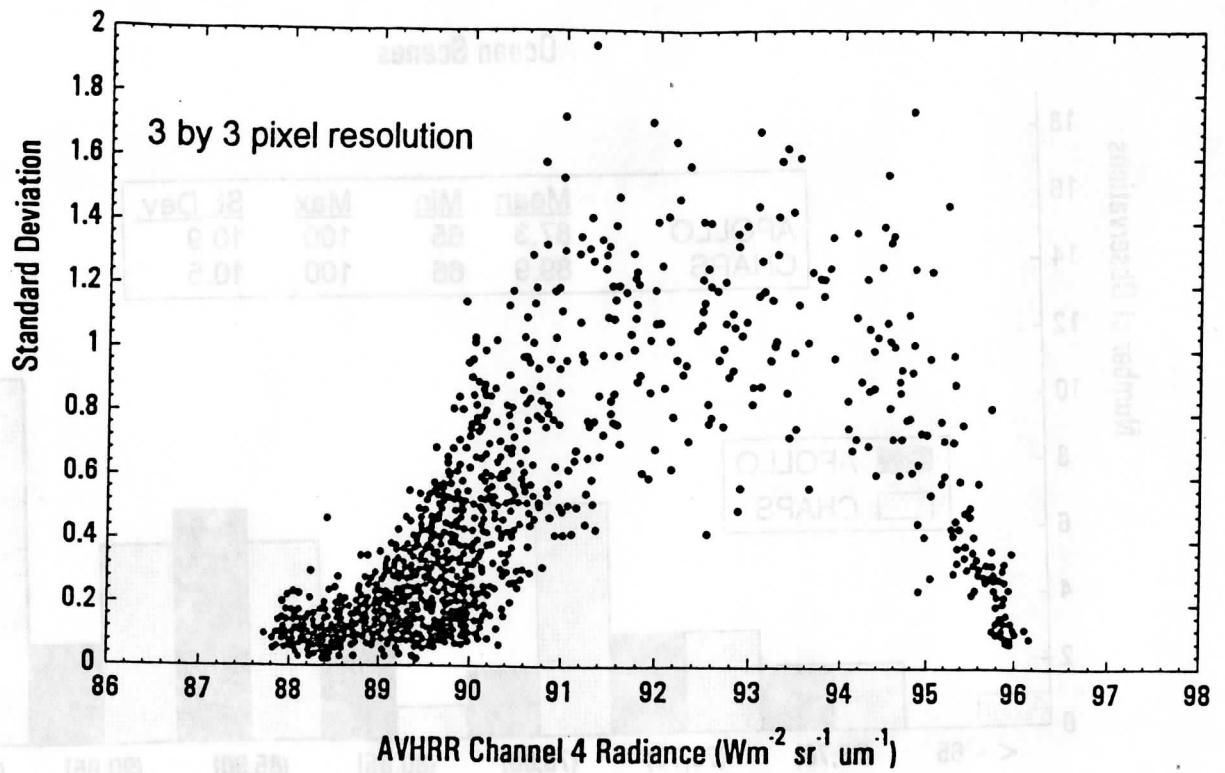Figure 5. A histogram summary of the cloud amounts derived from CHAPS and APOLLO over the Pacific region.

Figure 6. Spatial coherence diagram using (a) groups of 3×3 pixels and (b) averaging over the entire HIRS/2 footprint.
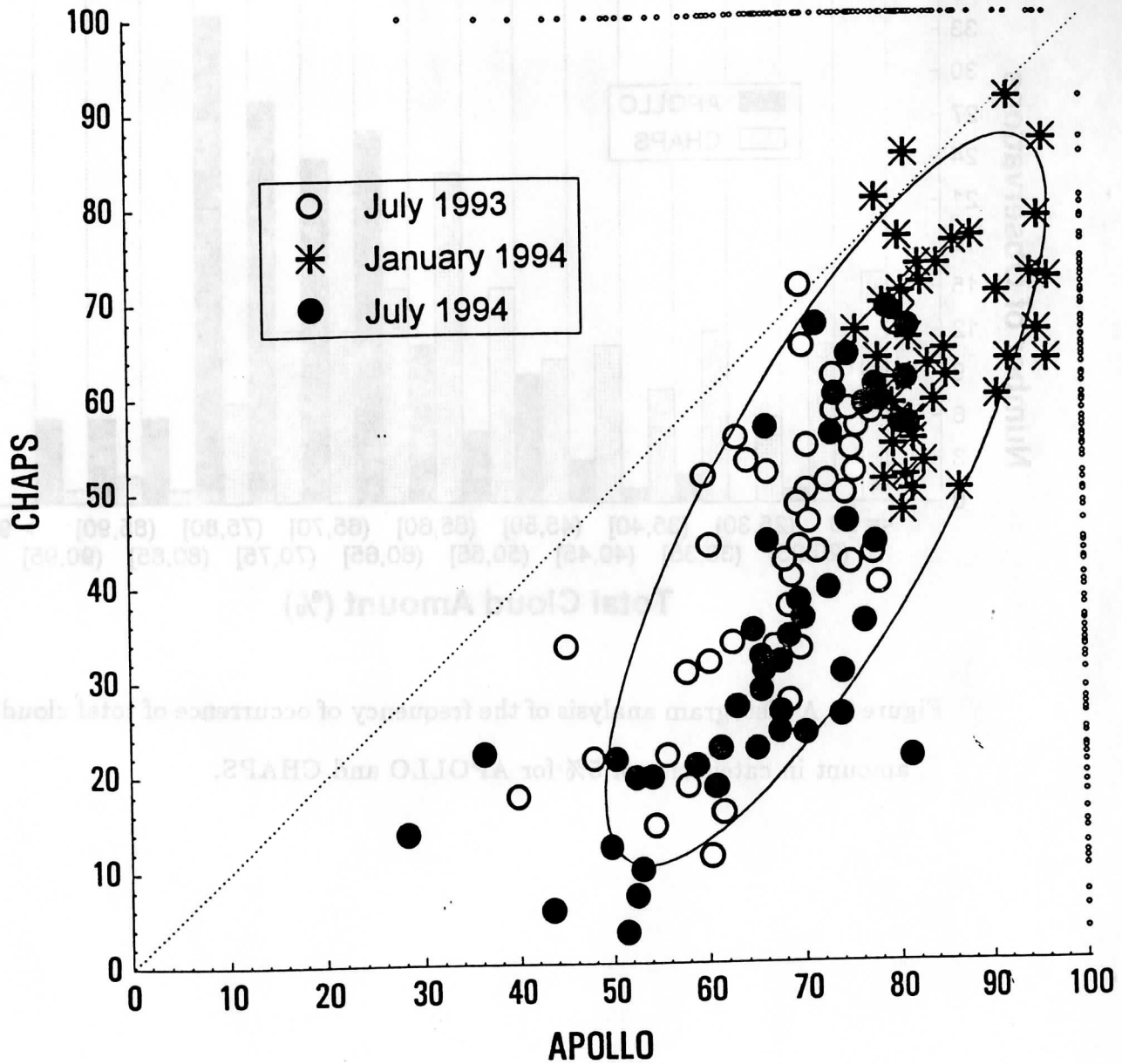
Figure 7. Regional cloud amounts of APOLLO versus the CHAPS effective cloud amounts. Circles represents comparisons for the month of July,

while the stars are results from January 1994. The ellipse, oriented along a linear regression between the two cloud products, denotes the 95% confidence interval. The small circles on the right axis denote the CHAPS retrieved effective cloud amounts while those on the top represent the APOLLO cloud amounts.

Figure 8. A histogram analysis of the frequency of occurrence of total cloud amount in categories of 5% for APOLLO and CHAPS.

Figure 9. Box-whisker diagram of CHAPS and APOLLO derived cloud amounts. The points represent the monthly mean cloud amount (circles – CHAPS and squares – APOLLO). The whiskers are ±2 standard deviations about the mean.

Figure 1. Geographic location of 25 German weather stations where circles, triangles and filled circles represent rural, mountain and city locations, respectively.

Figure 2. Surface derived cloud amount observations compared to the
APOLLO derived cloud amount, where the different symbols represent
the different surface sites as noted in the legend. The small circles on
the right axis denote the surface cloud amounts while those on the top
represent the APOLLO total cloud amounts.

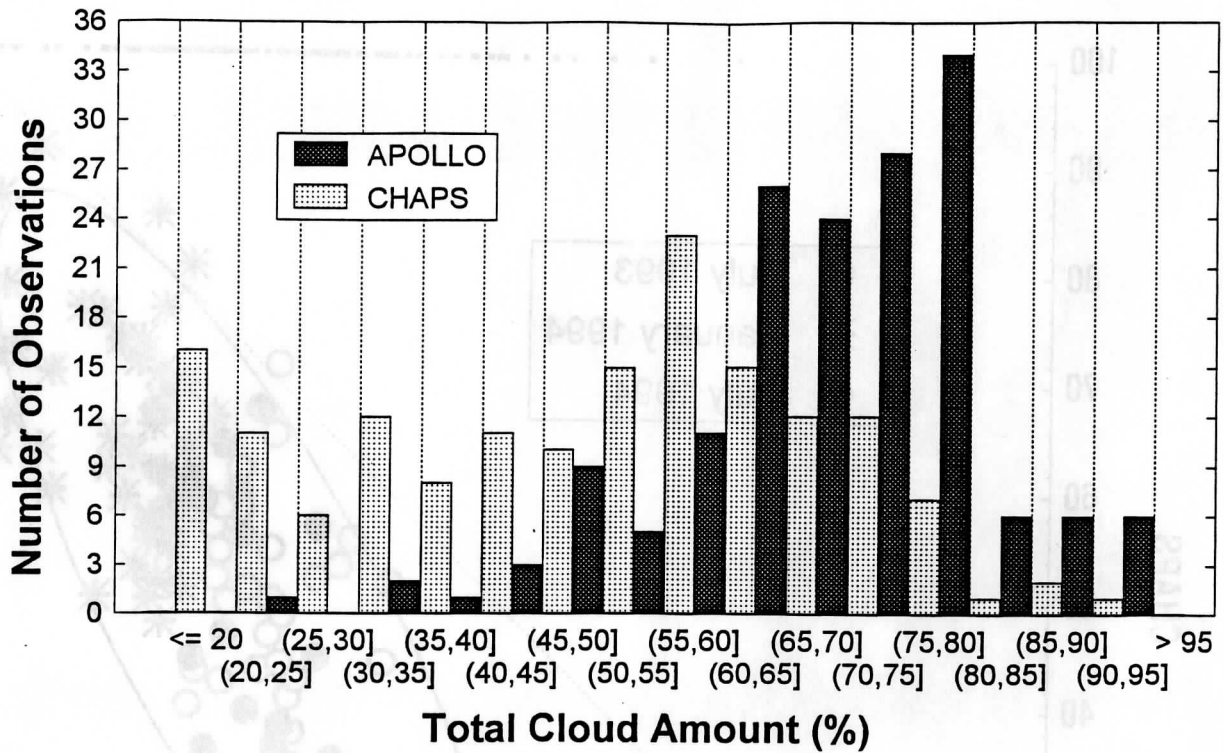|	Mean	Median	Min.	Max.	Std. Dev.	Skew
APOLLO	76.9	77.8	61.8	87.4	6.3	-0.64
Surface	72.4	72.8	57.5	88.1	8.8	0.88

Cloud Amount Differences

Number of Observations (y-axis)

15

10

5

0

x-axis labels:
<= -30
(-30,-25]
(-25,-20]
(-20,-15]
(-15,-10]
(-10,-5]
(-5,0]
(0,5]
(5,10]
(10,15]
(15,20]
> 20

Surface minus APOLLO

Figure 3. Histogram analysis of the surface cloud amount minus the APOLLO cloud amount. Also shown is a least squares fitted normal curve.

Figure 4. Comparison of APOLLO and CHAPS total cloud amount for the Pacific ocean regions. Each point represents an average cloud amount over a 2.5 degree grid box.

Ocean Scenes

	Mean	Min	Max	St. Dev.
APOLLO	87.3	65	100	10.9
CHAPS	89.9	66	100	10.5

Number of Observations

Total Cloud Amount (%)

Figure 5. A histogram summary of the cloud amounts derived from CHAPS and APOLLO over the Pacific region.

Figure 6. Spatial coherence diagram using (a) groups of 3×3 pixels and (b) averaging over the entire HIRS/2 footprint.

Figure 7. Regional cloud amounts of APOLLO versus the CHAPS effective cloud amounts. Circles represents comparisons for the month of July, while the stars are results from January 1994. The ellipse, oriented along a linear regression between the two cloud products, denotes the 95% confidence interval. The small circles on the right axis denote the CHAPS retrieved effective cloud amounts while those on the top represent the APOLLO cloud amounts.

Figure 8. A histogram analysis of the frequency of occurrence of total cloud amount in categories of 5% for APOLLO and CHAPS.

Figure 9. Box-whisker diagram of CHAPS and APOLLO derived cloud amounts. The points represent the monthly mean cloud amount (circles – CHAPS and squares – APOLLO). The whiskers are ±2 standard deviations about the mean.

BRIGHTNESS TEMPERATURE DIFFERENCE ANALYSIS
OF GLOBAL SATELLITE OBSERVATIONS[1]

Steven A. ACKERMAN
Cooperative Institute for Meteorological Satellite Studies
Space Science and Engineering Center
University of Wisconsin-Madison
Madison, Wisconsin

ABSTRACT

Field experiments such as FIRE are crucial to developing new remote sensing techniques and parameterizations suitable for global climate modeling. Field experiments are also extremely important in confirming satellite inferred properties, which may then be extended to the global scale and incorporated as parameterizations in General Circulation Models. This study employs a global satellite data set in a simplified analysis in an attempt to distinguish similarities between different cloud types and of similar clouds in different geographic locations.

It appears from the brightness temperature differences, that extremely cold clouds, those likely associated with convective cores, exhibit different radiative properties than clouds warmer than 215K. Large variations in spectral brightness temperature differences exist for clouds warmer than 215K, though they generally tend to align along a single envelope. The exception was differences between some clouds located over land in January, though it is pointed out that these clouds may be mis-identified clear-regions. Brightness temperature differences between 11 and 6.7 μm observations are suggested as a method of detecting tropical convective cores. An analysis of brightness temperature differences of three different oceanic stratus regimes at night suggests seasonal and regional differences in cloud properties.

Distinguishing clear and cloudy regions from satellite infrared radiances is a challenging problem in polar winter conditions due to the small temperature differences between the surface and the effective cloud temperature. Brightness temperature differences between 11 and 6.7 μm may provide a technique to determine clear-sky conditions over high-altitude polar regions during nighttime.

---

[1]A portion of this work was completed during the author's visit to the Institute of Atmospheric Physics, DLR, Germany.

1. INTRODUCTION

Global analysis of cloud amounts, types and optical properties using satellite measurements have been developed and are currently operational (e.g., the International Satellite Cloud Climatology Project; Rossow et al 1988, Rossow and Garder, 1993; CO_2 Slicing; Menzel et al 1994). Assessment of the reliability of satellite derived products requires intensive satellite, ground and aircraft observations during regional scale experiments such as FIRE (First ISCCP Regional Experiment). To date, the primary clouds observed during the FIRE field campaigns have been mid-latitude cirrus and stratus over oceans. These clouds are difficult to detect using passive satellite radiance measurements and are important cloud types in terms of the energy budget of the planet. As a result of the FIRE program there have been improvements in detecting these clouds and inferring their radiative properties using satellite passive measurements (This issue; Wielicki et al 1990; Ackerman et al 1990; Minnis et al, 1992; Baum et al 1992; Minnis et al 1993a; Strabala et al 1994).

The field experiments also provide the data base to develop new satellite cloud detection techniques and develop parameterizations of cloud radiative properties for use in weather and climate prediction models. While this data set is invaluable, the question remains as to how representative these observations are of clouds in other regions of the world, particularly the tropics and polar regions. The FIRE Pilot Tropical Cirrus Experiment, which occurred in conjunction with the TOGA COARE (Tropical Ocean and Global Atmosphere-Coupled Ocean Atmosphere Regional Experiment), and the Central Equatorial Pacific Experiment (CEPEX) has begun to address this question. This paper considers similarities and differences of clouds with respect to brightness temperature differences measured from a current meteorological satellite.

Radiance measurements from satellites provide the best means of routinely monitoring the global distribution of various climate parameters. The National Oceanic and Atmospheric Administration (NOAA) polar orbiting satellites have two instruments

2

useful for cloud detection and analysis, the Advanced Very High Resolution Radiometer (AVHRR) and the High-resolution Infrared Sounder/2 (HIRS/2). A near real-time algorithm to derive climate parameters using collocated HIRS/2 and AVHRR observations has been developed and implemented at the Cooperative Institute for Meteorological Satellite Studies (CIMSS). The Collocated HIRS/2 and AVHRR ProductS (CHAPS) include, among its oceanic cloud products, cloud amount and effective emissivity and cloud spectral radiative forcing. This paper makes use of these global observations to investigate differences between mid-latitude and tropical cirrus cloud characteristics. The paper also applies satellite brightness temperature difference retrievals developed under the FIRE program to investigate spectral variations of stratus clouds over different oceanic regions. In addition, a method is proposed to detect the presence of clouds over high-altitude geographic regions during winter nights (e.g., polar land regions during winter). Section 2 presents the data set used in the study. Section 3 analyzes high clouds. Section 4 presents an approach to detect clear sky conditions over high-altitude snow covered regions during night. Section 5 investigates difference between different stratocumulus regimes.

2. DATA ANALYSIS

The data base consists of collocated observations from the AVHRR and the HIRS/2 radiance measurements, and National Meteorological Center (NMC) analysis fields, derived as part of a global cloud retrieval algorithm using the operational NOAA meteorological polar orbiting satellites. This algorithm was run in a real-time mode during July 1993 and 1994 and January 1994 using observations made from the NOAA-12 spacecraft. This study presents results from July 1993 and January 1994. The NOAA-12 satellite is in an approximately 102 minute sun-synchronous orbit with local observations made near 0730 and 1930 LST for most latitudes.

Accurate discrimination between cloudy and clear scenes is essential to deriving accurate cloud products such as distributions of cloud altitude, amount and spectral cloud radiative forcing. The clear-sky detection method of this algorithm is described in detail by Frey and Ackerman (1994). Many cloud classification algorithms have been developed that are based on multi-spectral observations and are applicable to an individual satellite pixel or group of independent pixels. The present cloud type classification combines a variety of well-known approaches, such as the histogram method, split-window analysis, CO_2 slicing and spatial variability, along with new methods based on 8, 11 and 12 micron observations. An outline of the basic steps that constitute the classification method is presented below.

The first step in the cloud detection algorithm is to identify uniform scenes using the AVHRR data. This is performed using a statistical coherence type approach (e.g., Coakley and Bretherton, 1982). Classification of these uniform scenes is a function of the spectral properties; for example, low albedo during the day will likely be clear sky ocean. Individual pixels with similar spectral properties as the uniform scenes are then classified, with the remaining pixels as either non-uniform or multi-layered clouds. To further improve cloud classification, we combine the AVHRR observations with measurements of the HIRS/2 sounder. The advantage of the HIRS/2 is not its spatial resolution, approximately 17 km at nadir, but rather its multi-spectral observations. By collocating the AVHRR pixels within the larger HIRS/2 footprint, we take advantage of the strength of each instrument (AVHRR-spatial resolution; HIRS/2-spectral resolution) and produce an enhanced cloud product. The CO_2 slicing technique (Smith and Platt, 1978; Menzel et al., 1983, Menzel et al, 1994) is applied to the HIRS/2 observations to determine the presence of thin cirrus and define cloud top pressure, and effective emittance. The CO_2 technique for deriving cloud top pressure takes advantage of the differing partial CO_2 absorption in several of the HIRS/2 15 μm infrared channels. This gives the CO_2 technique the ability to identify thin cirrus clouds that might be missed by other techniques

4

that cannot account for the transmission of terrestrial radiation through the cirrus, such as threshold methods applied to the AVHRR observations.

These global, coincident observations from the AVHRR and the HIRS/2 provide a data base to explore potential differences in the radiative characteristics of clouds in different regions of the world at different times of the year. First we consider high clouds, then we look at three stratus regimes.

3. HIGH CLOUD ANALYSIS

In conducting the high cloud analysis the collocated observations have been restricted to the following requirements:

1) The entire HIRS/2 field-of-view (FOV) is determined to be overcast using the AVHRR collocated pixels. See Frey and Ackerman (1994) for a description of the AVHRR cloud threshold.

2) The 11 μm brightness temperature of the HIRS/2 FOV is colder then 240K.

3) The CO_2 slicing method indicated the presence of a high cloud, defined as a cloud top pressure less than 400 mb.

The 8-12μm and 3.7-4μm window regions are important infrared spectral regions for cloud detection algorithms (Hunt, 1973; Schiffer and Rossow, 1983; d'Entremont, 1986; Allen et al 1990; Minnis et al, 1992; Minnis et al 1993.) As we have a more intuitive feeling for temperature, the satellite measured radiance is converted to an equivalent brightness temperature using the Planck function. Brightness temperature differences between these spectral observations have been used extensively for cloud detection and classification (e.g., Inoue 1987a and b; Booth 1978; Stone et al 1990; Parol et al 1991). Cloud retrieval algorithms have been developed using these spectral channels under the FIRE program (e.g., Ackerman et al 1990, Baum et al 1994).

3.1 8, 11 and 12 μm Brightness Temperature Difference Analysis

Using HIS observations from FIRE I, Ackerman et al (1990) suggested a tri-spectral infrared cloud detection technique using wavelengths near 8.5, 11 and 12 microns. The technique is physically based on the absorption differences between ice and water vapor in the 8-12 μm window region (Ackerman et al, 1990; Strabala et al 1994); so that positive 8 minus 11μm brightness temperature differences indicate cloud while negative differences, over oceans, indicate clear regions. The analysis consists of comparing brightness temperature differences between 11 and 12 μm (BT_{11}-BT_{12}) versus those of 8 and 11 μm (BT_8-BT_{11}) as a function of the 11 μm brightness temperature. These differences are related to the cloud microphysical properties as demonstrated by Ackerman et al (1990) and in more detail by Takano et al (1992) and Smith et al (1992). This tri-spectral method was further enhanced by Strabala et al (1994) using MAS (MODIS Airborne Simulator) observations from FIRE II. Figure 1 is a frequency scatter diagram of the tri-spectral analysis of these high-clouds for January 1994. The number of points at a given value of BT_8-BT_{11} and an associated BT_{11}-BT_{12} is represented by its size as denoted in the legend. Maximum frequency occurs at approximately BT_{11}-BT_{12}=0.8K and BT_8-BT_{11}=0.7K. Two groupings of points are evident, one is an envelope of the BT_8-BT_{11} versus BT_{11}-BT_{12} differences with a slope of approximately 1. The second group of points are centered at approximately BT_{11}-BT_{12}= -0.6K and BT_8-BT_{11}=1.5K.

A similar frequency scatter diagram is shown for July 1993 in Figure 2 (note the changing legend). Maximum frequency for July occurs at approximately BT_{11}-BT_{12}=1.1K and BT_8-BT_{11}=0.4K, different than the month of January. Two groupings are evident during this month, though the distinction is less than in the month of January. The January grouping with BT_{11}-BT_{12}<0, has now shifted to approximately BT_{11}-BT_{12}=0.4K and BT_8-BT_{11}=1.5K. Such a shift in the tri-spectral diagram is indicative of changing cloud properties suggesting differences between the January and July cloud types.

To further explore these differences, the tri-spectral diagram was categorized as a function of latitude and the 11 μm brightness temperature as shown in Figure 3. Each of the 9 plots is an individual BT_{11}-BT_{12} versus BT_8-BT_{11} graph. The upper row is for observations in the southern hemisphere between 20S and 50S, the middle rows tropical observations between 20S and 20N and the bottom row are observations between 20N and 50N. The columns categorize the data by brightness temperature at 11 μm; these categories are, going from left to right: $BT_{11} \leq 210$; $210 < BT_{11} \leq 220$; $220 < BT_{11} \leq 230$ and $230 < BT_{11} \leq 240$. Figure 3a depicts January results that separate the tri-spectral diagram into two distinct patterns -- colder than 210K the points tend toward a circular pattern with much scatter. Most of these observations fall in the tropical region and the summer hemisphere and are associated with convection. The sloping envelope of points noted in Figure 1, tends to occur in the latitude belts outside the tropics with temperatures warmer then 210K. Hints of this envelope appear in the tropical division of 11 μm temperatures, particularly $BT_{11} > 230$. While there is much scatter, this slope appears independent of brightness temperature categorization. Notice also the 'check pattern' that appears in the northern hemisphere for clouds between 230K and 240K (a hint of this pattern is also seen in the 220-230K category for the northern hemisphere). Such a difference suggests the clouds have different microphysical properties; however, as we shall see later, one of these grouping is associated with clouds over land and may result from an inaccurate cloud retrieval.

Figure 3b presents similar scatter diagrams for July, with some important differences from January. First is that the check pattern in the winter hemisphere is no longer present. The second is that for clouds colder that 210K, while still displaying the circular pattern, the grouping is shifted toward slightly positive differences between BT_{11}-BT_{12}. Such a shift suggests differences in the cloud properties between January and July for these cold convective clouds.

3.2 11 and 3.7 micron Brightness Temperature Difference Analysis

Observations near 11 and 3.7 μm have also been used to detect clouds and infer their optical and microphysical properties(e.g., Hung and Liou, 1984; Arking and Childs, 1985; Allen et al 1990; Stone et al, 1990; Ou et al, 1993). For ice clouds the effective transmissivity is larger at 11 μm than 3.7 μm. For optically thin cirrus the emittance at 3.7 may be much smaller than at 11 μm due to differences in the imaginary index of refraction. For water cloud the emittance at 3.7 μm is more sensitive to changes in optical depth and effective radius than the emittance at the longer infrared (IR) wavelengths. Here we explore differences between 3.7 and 11 μm not with the intention of retrieving the various properties as undertaken by the previous authors, but rather to compare differences between January and July.

Figure 4 depicts the relationship between BT_{11} and $BT_{3.7}$ for January and July. Due to solar reflection the relationships are depicted for day and night separately. Major differences between the months are in the day versus nighttime occurrence of cold cloud top temperatures. July depicts large number of occurrences during the ascending and descending orbits while January displays a greater frequency of occurrence in the daylight hours. This is likely due to late afternoon and early evening summer-time convection over the northern hemisphere. During both months there are two distinct groups of points similar to that observed in the tri-spectral analysis. The other difference between the months is a slightly larger variability in January, in terms of the scatter about the envelope of points with $BT_{11} > 220K$. July also does not have as cold temperatures as January. Solar reflection is large in both months, adding approximately 40K to the cold cloud tops, due to the optically thick nature of these clouds.

As with the tri-spectral analysis, the two months display differences between the very cold clouds, often associated with convection, and clouds warmer than 220K.

3.3 11 and 6.7 micron Brightness Temperature Difference Analysis

Observations at 11 and 6.7 μm have also been used to study high-clouds (Szejwach, 1982; Pollinger and Wendling, 1984: Liou et al 1990). In clear-sky situations, satellite observations in the 6.7 μm spectral channel are sensitive to the relative humidity averaged over a depth of the atmosphere extending from approximately 200 to 500 mb (Soden and Bretherton 1992). Surface temperature studies use the 11 μm channel as absorption by atmospheric gases is weak near this wavelength. Under clear sky conditions, the 11 μm brightness temperature (BT_{11}) is usually larger than the 6.7 μm equivalent blackbody temperature ($BT_{6.7}$) as the radiant energy measured at 11 μm is associated with the lower atmosphere and surface, where it is often warmer. The global analysis show satellite observations with negative brightness temperature differences between 11 and 6.7 μm (BT_{11}-$BT_{6.7}$). For example, Figure 5 depicts the geographic location, within 50 north and south latitude, of each occurrence of a negative difference during January 1994 and July 1993. Each circle represents the geographical location of a single HIRS/2 field-of-view (FOV) that displayed a negative difference in BT_{11}-$BT_{6.7}$. The differences correlate highly with expected regions of convection. The Intertropical Convergence Zone (ITCZ) is apparent in both months, as is the shift in its position to the summer hemisphere. The summertime peak in convection over South America and convection associated with the southwest summer monsoon are also clearly visible. Geographic regions not favorable for convective activity also manifest themselves in this composite analysis. In addition to regions favorable to tropical convection, negative differences also appear in the mid-latitude storm tracks of the winter hemisphere.

Figure 6 displays the difference between 11 and 6.7 μm (BT_{11}-$BT_{6.7}$) as a function of BT_{11} for January (top) and July (bottom) for observations made over water (left) and land (right). Negative differences occur for $BT_{11} < 215K$, with larger variations in January. Note that at temperatures colder than 210K, differences can be positive or negative. As with the window brightness temperature differences, distinct differences

occur between January and July. For a given BT_{11} larger variations occur in the temperature difference for the month of January, particularly for $BT_{11} < 210K$. For $BT_{11} > 215K$ two distinct relationships are also seen for the January land cases, while this is not the situation in July. As we shall discuss in Section 4, these negative values in the January land cases may result from a mis-identification of a cloud. Over a high-altitude region during the winter (e.g. Himalayas in January - see Figure 5) negative values may exist due to the presence of a strong low-level temperature inversion. These negative differences over land occur in both the early morning and early evening satellite overpasses of the NOAA-12.

To further investigate the utility of using these negative values for studies of tropical convection, observations from the GOES VISSR (Visible Infrared Spin Scan Radiometer) Atmospheric Sounder (VAS) 11 and 6.7 μm channels were collocated with rain-rate estimates derived from the Defense Meteorological Satellite Program's (DMSP) Special Sensor Microwave Imager (SSMI). As the VAS and SSMI were flown on separate satellites, collocation of the observations was accomplished by averaging the values over 125×125 km boxes. The observations from the different satellites were required to be made within 10 minutes of each other and for the same geographic region. The eight cloud systems observed were in the eastern tropical Pacific (10°S-20°N; 120°W-150°W) between 1700-1900 UTC. Figure 7 is a histogram of the SSMI derived rain-rates categorized by negative and positive values of $BT_{11}-BT_{6.7}$ averaged over the 128 km box. The intriguing aspect of this figure is that whenever the brightness temperature difference is less than zero (left panel), the SSMI indicates rain (all values are greater than zero). The magnitude of these differences had little relationship to the magnitude of the derived rainrate. Such an 'on' switch could be an extremely valuable tool for characterizing a precipitation system and studying tropical convection. Note that positive differences are associated with rain or no-rain cases.

The negative values were always associated with cold 11 μm brightness temperatures suggesting cold, convective type storms. The geographic position of the negative observations relative to cloud systems in the tropical Pacific were determined using the Man-computer Interactive Data Acquisition System (McIDAS) (Suomi et al, 1983) by overlaying the position of the negative BT_{11}-$BT_{6.7}$ on the 1 km resolution GOES-7 visible imagery. In such analysis the negative values tended to be associated with the convective core of the cloud system. These cores, or 'hot towers' are regions associated with strong updrafts that give the appearance of 'cauliflower' tops. Simulation studies of these satellite observations using a plane-parallel multiple scattering radiative transfer model, indicate that BT_{11}-$BT_{6.7}$ are positive, or zero in the case of very thick clouds as both spectral radiances have large contributions from particles near the cloud top.

It is possible that calibration errors may cause these negative values. To increase the signal-to-noise in the VAS measurements, multiple samples of the radiance are sensed by leaving the mirror position fixed on a given earth location for multiple spins of the GOES spacecraft. Calibration of the VAS instrument is discussed by Menzel et al (1981) and suggest random noise of individual observations of ±0.75K and ±0.05K in the $BT_{6.7}$ and BT_{11} observations, respectively. Biases at both these channels are estimated to be less than 2K. While these calibration issues can result in negative BT_{11}-$BT_{6.7}$ observations, we would not expect such errors to be strongly correlated to a particular location of the storm, such as the convective core, particularly since the cirrus cloud shield surrounding the core can have similar temperatures.

The footprint of the VAS 6.7 μm observations is approximately 16 km at nadir (the HIRS/2 is approximate 18 km). It is highly likely that the field-of-view (FOV) is not uniform when viewing the convective center of the storms. As the Planck function is non-linear, this non-uniform FOV can generate brightness temperatures that vary between widely spaced spectral channels. Let us consider a two-layer cloud, with one layer at a

11

temperature 190K and the other at a temperature of 215K. Assuming the clouds behave as a blackbody, we estimate the observed radiance by linearly averaging the radiance at each of these temperatures as function of the fraction of cloud cover within the FOV, that is

$$I^\lambda_{measured} = f I^\lambda_{190} + (1-f) I^\lambda_{215}$$

where I^λ_{190} and I^λ_{215} are the radiance at 190K and 215K respectively at wavelength λ, f is the fraction of the field-of-view covered by the cloud with a temperature of 190K, and $I^\lambda_{measured}$ is the measured radiance of the non-homogeneous FOV. The measured radiance is then converted to a brightness temperature and the result shown in Figure 8. The solid and dashed lines represent the $BT_{6.7}$ and BT_{11} observations as a function of f. The difference is the dotted line whose magnitude is noted on the right-hand ordinate. It is possible to generate a spectral temperature difference of -1.5K based on scene uniformity; however, some of the observed differences are smaller than -3K.

Whatever the mechanism for generating these negative values associated with the convective core, they are an extremely useful tool for studying the hydrological cycle. Convective activity is extremely variable in both time and space, as is evident by plotting the geographic location of the negative differences for a single day. On any given day only a very small portion of the globe is convectively active - as indicated by these observations. The 11 and 6.7 μm observations are currently available on the GOES and METEOSAT geostationary satellites and the NOAA polar orbiting satellites providing the spatial completeness and temporal continuity required for studying tropical convection. The capability to locate the convective core has an important impact on the following applications:

- Measurements from passive radiometers at visible and infrared window (e.g., 0.5 and 11 μm) wavelengths are widely used in precipitation retrievals. These techniques can be enhanced by incorporating observations at 6.7 μm to denote, in conjunction with the 11 μm channel, the core of convective systems.

12

- Precipitation estimates using passive radiometers may be improved by classifying tropical convective systems according to the life cycle of the storm. Systems with convective cores denote a convective system in its mature stage, and one likely to contain heavy precipitation.

- As the observations are available on geostationary satellites, they support studies of the periodic nature (e.g., diurnal) of active convective systems over the tropical oceans.

- The moistening of the stratosphere is believed to occur during tropospheric-stratospheric exchanges due to the overshooting tops associated with convective cores. The frequency of occurrence of such exchanges can be estimated if we can detect the frequency of occurrence of these cores.

- The potential of increased convection associated with a warmer climate raises speculation if the troposphere will moisten due to upward transport of moisture, or dry due to corresponding subsidence in surround regions. The 6.7 μm observations can be used to estimate the upper troposphere relative humidity in clear-sky conditions surrounding the convective regions. Thus, time-lag correlations of the convective core and clear-sky humidity may provide some quantitative information regarding this issue.

4. A POTENTIAL SATELLITE CLEAR-SKY DETECTION METHOD DURING POLAR WINTER CONDITIONS

One of the objectives of the FIRE program is to develop new and improve existing passive remote sensing capabilities from the satellite platform. Distinguishing clear and cloud regions from satellite IR radiances is a challenging problem in polar winter conditions due to the cold surface temperatures. Under clear-sky conditions, surface radiative temperature inversions often exist. Thus, in the regions IR channels whose weighting function peaks down low in the atmosphere, will often have a larger BT than a window channel, for example $BT_{8.3} > BT_{11}$. The previous example can also confuse the surface inversion with thick cirrus cloud, and thus need to be accompanied by other tests

(e.g., the magnitude of BT_{11} or the $BT_{11}-BT_{12}$). Channels in the window region must also account for the spectral emissivity of ice and snow that varies with surface condition. The CHAPS global analyses of $BT_{11}-BT_{6.7}$ have shown large negative differences (less than -10K) over the Antarctic Plateau and Greenland during winter, which may be indicative of clear-sky and the existence of a strong low-level temperature inversion. Figure 9 depicts the geographic location of $BT_{11}-BT_{6.7}$ differences of less than -5K for a single HIRS/2 FOV over the south-pole region during July 1993. Strong radiative temperature differences have been observed during the winter on the continent of Antarctica. Temperatures near the surface can reach 200K, while the middle troposphere is 235K. In cloud free conditions strong water vapor absorption channels, such as the 6.7 μm, will have a warmer equivalent brightness temperature than the 11 μm window channel. This brightness temperature difference between 11 and 6.7 μm may therefore be very useful for detecting cloud free conditions in the polar evening. Similar observations were observed over Greenland in July 1993. Such surface inversions may explain the negative differences observed over the January land cases discussed in Section 3. While physically reasonable, this technique has not been verified with ground nor aircraft observations. Future experiments, such as SHEBA (Surface Heat Budget of the Arctic) may provide the verification data for the proposed technique.

5. STRATOCUMULUS CLOUD ANALYSIS

A wide variety of techniques have been developed to detect the presence of stratocumulus clouds from satellite measured radiances. For oceanic stratus, solar channels provide the best method of cloud detection outside the sun-glint region (e.g. Saunders and Kriebel, 1988; Stowe et al 1991; Derrien et al 1993). Spatial variability tests are also very useful tests for these layered cloud systems (Coakley and Bretherton, 1982; Coakley, 1990). It is more difficult to detect these clouds during the night, due to the small temperature difference between the cloud and the underlying surface. When the

14

solar zenith angle is greater than approximately 80° or in regions of sun-glint, detection of these clouds is often based on brightness temperature differences. Using nighttime AVHRR observations at 10.8 and 3.7 μm, Baum et al (1994) demonstrated that for stratus clouds, brightness temperature differences become negative for high optical depths for an effective radius (r_{eff} - the third moment of the size distribution divided by the second moment) of smaller than approximately 8 μm. Baum et al (1994a) also combined the 10.8 and 3.7 μm AVHRR observations with HIRS/2 CO_2 channel observations to analyze scenes of overlapping cloud layers. A multilevel cloud detection technique was applied to FIRE II observations by Baum et al (1994b).

This section uses the global data set from NOAA-12 to investigate differences between satellite brightness temperatures of three oceanic stratus regimes: off the west coast of South America (15-30S latitude; 71-86E longitude); off the west coast of southern Africa (15-30S latitude; 0-15E longitude); and off the west coast of North America (30-45N latitude; 120-135W longitude). Following Baum et al (1994) the analysis is presented in terms of BT_{11} versus $BT_{3.7}-BT_{11}$, with the following additional restriction: CO_2 slicing from the HIRS/2 observations indicates a cloud top pressure greater than 650 mb. The clear-sky regions in the following diagrams are determined as in Frey and Ackerman (1994) who employ a series of checks based on a histogram analysis of AVHRR observations, spatial variability tests, and brightness temperature difference thresholds at 8, 11 and 12 μm. These clear-sky values are circled in the accompanying figures.

Figure 10a depicts the relationship between the $BT_{3.7}-BT_{11}$ and BT_{11} for the region off the coast of California. The circle denotes the region where the majority of the clear-sky scenes resided. The stratus cloud observations tend to fall between $280<BT_{11}<285$ with the majority having $-4<BT_{3.7}-BT_{11}<-1$. From the work of Baum et al (1994) these negative differences indicate optically thick clouds with effective radii between approximately 4 and 8 μm. This is slightly smaller than the effective radius

derived by Minnis et al (1992) for a smaller region centered on the FIRE I stratus experiment central site (see their Figure 30). Minnis et al (1993) infer the effective particle radius using liquid water paths derived from ground based microwave observations and satellite visible reflectance measurements. There is no physical reason to expect the satellite inferred effective radius to be spectrally conservative. Thus, effective radii derived at different wavelengths may differ in their size. Figure 10b depicts the split-window difference $(BT_{11}-BT_{12})$ versus BT_{11} for the same region. The split-window difference is not as sensitive to particle size as $BT_{3.7}-BT_{11}$ as indicated by the work of Baum et al (1994). For these stratus clouds off the coast of California, $BT_{11}-BT_{12}$ ranges (Figure 10b) from approximately 0 - 1K-- consistent with Figure 10a and the model calculations of Baum et al (1994).

Figure 11 presents the 3.7 and 11 μm brightness temperature difference diagrams for stratus off the west coast of South America in January and July. The clear-sky observations (circled region) indicates warmer BT_{11} in January, 290-294K versus the 285-290K temperature of July. The group of cloud observations also tend to shift to warmer BT_{11} values in January. $BT_{3.7}-BT_{11}$ in July are generally greater than -3K while there are many values less than -3K in January. This may result from either optically thicker clouds or an increase in the effective radius. Several points appear to be contaminated by cirrus clouds, as suggested by the analysis of Baum et al (1994). The multilevel cloud detection of Baum et al (1994) is not currently included in the CHAPS algorithm, though for this regional analysis there tend to be only a few contaminated cirrus scenes.

Analysis for the stratus off the west coast of South Africa is depicted in Figure 12. This analysis is similar for the two months, though July appears to have more cirrus contamination and larger negative values of $BT_{3.7}-BT_{11}$. For January, $BT_{3.7}-BT_{11}$ ranges between -2K and 2K. When compared to the geographic region off the west coast of the America's, it suggests the clouds have a larger effective radius or are optically

16

thinner. For this geographic region, the clear-sky values do not separate out as well as in the previous two areas. This may result from optically thinner clouds or not as an accurate clear-sky retrieval. Cirrus contamination may also play a role in merging the clear and stratus regimes.

In additional to seasonal differences, differences also exist between geographic regions. For example, the July 93 stratus off the west coast of North America, have similar clear-sky BT_{11} to the July 1993 clear-sky region off the west coast of South America. The clouds off South America tend to display colder BT_{11}, have more cirrus contamination and have smaller values of $BT_{3.7}$-BT_{11}. The south-eastern Pacific clouds may either have higher tops, be optically thicker or have smaller effective radii than their northern components. Determination of which is the major factor contributing to the $BT_{3.7}$-BT_{11} differences requires more detailed analysis of the satellite data, preferably combined with observations and/or modeling results.

6. SUMMARY

There is an acute awareness of the importance of clouds and hydrological processes, in understanding climate change. Field experiments such as FIRE are crucial to developing new remote sensing techniques and parameterizations suitable for global climate modeling. Satellite observations provide the means to extend these regional observations to the global scale.

Understanding climate change will require models that simulate the atmosphere, the complete hydrological cycle, surface processes and biological cycles. Such complete physical models will not be available for some time, if ever. It is therefore necessary to describe the parameters and relationships using empirical data sets, such as satellite observed relationships between cloud emittance and albedo. This is often a focus of field experiments. Field experiments are also extremely important in confirming satellite

inferred properties, which may then be extended to the global scale and incorporated as parameterizations in General Circulation Models.

This study employs a global satellite data set in a simplified analysis to attempt to distinguish similarities between different cloud types and of similar clouds in different geographic locations. Observing such differences requires either large differences, making it trivial for observational studies to detect (e.g., an El Nino year) or one must employ many observations. The later is the approach undertaken in this study. In addition, improvements in cloud detection and classification using passive infrared observations at 11 and 6.7 µm are presented. The analyses are summarized as follows:

- It appears from the brightness temperature differences, that extremely cold clouds, those likely associated with convective cores, exhibit different radiative properties than clouds warmer than 215K. Variations in spectral brightness temperature differences between combination of 6.7 8, 11, 12 µm, exist for clouds warmer than 215K, though differences tend to align along a single envelope. The exception was differences between some clouds located over land in January, though it is pointed out that these clouds may be misidentified clear-regions.

- Brightness temperature differences between 11 and 6.7 µm observations are suggested as a method of detecting tropical convective cores. These spectral observations also have the potential to distinguish clear-sky conditions over high-altitude polar regions during nighttime.

- An analysis of brightness temperature differences of three different oceanic stratus regimes at night suggests seasonal and regional differences in cloud properties.

- A method to distinguish clear-sky conditions over high-altitude polar regions during nighttime is suggested using brightness temperature differences between 11 µm and 6.7 µm observations.

18

The analyses presented here clearly indicates differences in the radiative properties of high clouds colder and warmer than 210K. There is, however, much variability in each of different analyses. Whether this scatter is associated with natural variability or is a function of cloud type, requires a more detailed analysis. The analyses presented in this paper are primarily at the spatial resolution of the HIRS/2. The individual AVHRR pixels collocated within the HIRS/2 footprint are also available for further classification of cloud type and a more in-depth analysis of the causes of this variability. Differences also appear in stratocumuls clouds as a function of geographic region and time of year and may be associated with the microphysical and/or macrophysical properties of the cloud. AVHRR pixel analysis may also be of use in separating out these effects. These are the foci of on-going work.

7. REFERENCES

Ackerman, S. A., W. L. Smith, J. D. Spinhirne and H. E. Revercomb 1990: The 27-28 October 1986 FIRE IFO cirrus case study: Spectral properties of cirrus clouds in the 8-12 μm window. *Mon. Wea. Rev*, **118**, 2377-2388.

Allen, R. C., Jr., P. A. Durkee, and C. H. Wash, 1990: Snow/cloud discrimination with multispectral satellite measurements. *J. Appl. Met.*, **29**, 994-1004.

Arking, A. and H. D. Childs, 1985: Retrieval of cloud cover parameters from multispectral satellite images, *J. Clim. Appl. Meteorol.* **23**, 322-333.

Baum, B. A., B. A. Wielicki and P. Minnis, 1992: Cloud-property retrieval using merged HIRS and AVHRR data. *J. App. Meteor.*, **31**, 351-368.

Baum, B. A., R. F. Arduini, B. A. Wielicki, P. Minnis, and S. -C. Tsay, 1994a: Multilevel cloud retrieval using multispectral HIRS and AVHRR Data: Nighttime oceanic analysis. *J. Geophys. Res*, **99**, 5499-5514.

Baum, B. A., T. Uttal, M. Poellot, T. P. Ackerman, J. M .Alvarex, J. Intrieri, D. O'C. Starr, J. Titlow, V. Tovinkere, and E. Clothiaux, 1994b: Satellite remote sensing of multiple cloud layers. Submitted to the *Jour. Atmos. Sci.*

Coakley, J. A. Jr., and F. P. Bretherton, 1982: Cloud cover from high resolution scanner data: Detecting and allowing for partially filled fields of view. *J. Geophys. Res.*, **87**, 4917-4931.

Coakley, J. A. Jr., 1990: Reflectivities of uniform and broken layered clouds. *Tellus*, **43B**, 420-433.

d'Entremont, R. P., 1986: Low- and midlevel cloud analysis using nighttime multipsectral imagery. *J. Clim. Appl. Met.*, **25**, 1853-1869.

Derrien, M., B. Farki, L. Harang, H. LeGleau, A. Noyalet, D. Pochic, and A. Sairouni, 1993: Automatic cloud detection applied to NOAA-11/AVHRR imagery. *Remote Sens Environ.*, **46**, 246-267.

Frey, R. A. and S. A. Ackerman, 1994: Climate parameters from satellite spectral measurements. Part I: Collocated AVHRR and HIRS/2 observations of spectral greenhouse parameter. Submitted to the *Jour. Appl. Met.*

Huang, R. and K. N. Liou, 1984; Remote sounding of cirrus optical depth and temperature from 3.7 and 11 μm windows, *Adv. Atmos. Sci.*, **1**, 150-164.

Hunt, G. E., 1973: Radiative properties of terrestrial clouds at visible and infrared thermal window wavelengths. *Quart J. Roy. Meteorol. Soc.*, **99**, 346-369.

Inoue, T., 1987a: An instantaneous delineation of convective rainfall areas using split window data of NOAA-7 AVHRR. *J. Meteor. Soc. Japan.*, **65**, 469-480.

Inoue, T., 1987b: A cloud type classification with NOAA-7 split window measurements *J. Geophys. Res.*, **92**, 3991-4000.

Liou, K. N., S. C. Ou, Y. Takano, F. P. J. Valero, and T. P. Ackerman, 1990: Remote sounding of the tropical cirrus cloud temperature and optical depth using 6.5 and 10.5 μm radiometers during STEP. *J. Appl. Meteorol.*, **29**, 716-726.

Menzel, W. P., W. L. Smith, and T. R. Stewart, 1983: Improved cloud motion wind vector and altitude assignment using VAS. *J. Clim. Appl. Meteor.*, **22**, 377-384.

Menzel, W. P., D. P. Wylie and K. I. Strabala, 1989: Characteristics of global cloud cover derived from multispectral HIRS observations. Technical Proceedings of the Fifth International TOVS Study Conference, 24-28 July 1989, Toulouse France, 276-290.

Menzel, W. P., D. P. Wylie and K. I. Strabala, 1994: Four years of global cirrus cloud statistics using HIRS. Submitted to the *Jour. Climate*.

Minnis, P., P. W. Heck, D. F. Young, C. W. Fairall, and J. B. Snider, 1992: Stratocumulus cloud properties derived from simultaneous satellite and island-based instrumentation during FIRE. *J. Appl. Meteor.*, **31**, 317-339.

Minnis, P., P. W. Heck, and D. F. Young, 1993: Inference of cirrus cloud properties using satellite-observed visible and infrared radiance. Part II: Verification of theoretical cirrus radiative properties. *J. Atmos. Sci.*, **50** 1305-1322.

Minnis, P., K. -N. Liou and Y. Takano, 1993: Inference of cirrus cloud properties using satellite-observed visible and infrared radiance. Part I: Parameterization of radiance fields. *J. Atmos. Sci.*, **50** 1279-1304.

Ou, S. C., K. N. Liou, W. M. Gooch and Y. Takano, 1993; Remote sensing of cirrus cloud parameters using advanced very-high resolution radiometer 3.7- and 10.9-μm channels. *Appl. Opt.*, **12** 2171,2180.

Parol, F., J. C. Buriez, G. Brogniez, and Y. Fouquart, 1991: Information content of AVHRR channels 4 and 5 with respect to the effective radius of cirrus cloud particles. *J. Appl. Met.*, **30**, 973-984.

Pollinger, W. and P. Wendling, 1984: A bispectral method for the height determination of optically thin ice clouds. *Contrib. Atmos. Phys.* **57**, 269-281.

Prabhakara, C., R. S. Fraser, G. Dalu, M. -L. Wu, and R. J. Curran, 1988: Thin cirrus clouds: Seasonal distribution over oceans deduced from Nimbus-4 IRIS. *J. Appl. Met.*, **27**, 379-399.

Rossow, W. B., L. C. Garder, P. Lu and A. Walker, 1988: International Satellite Cloud Climatology Project (ISCCP), Documentation of cloud data. WCRP Rep., 78 pp.

Rossow, W. B. and L. C. Garder, 1993: Cloud detection using satellite measurements of infrared and visible radiances for ISCCP., *J. Climate*, **6**, 2341-2369.

Saunders, R. W. and K. T. Kriebel, 1988: An improved method for detecting clear sky and cloud radiances from AVHRR data. *Int. J. Remote Sens.* **9**, 123-150.

Schiffer, R. A. and W. B. Rossow, 1983: The International Satellite Cloud Climatology Project (ISCCP): The first project of the World Climate Research Programme. *Bull. Amer. Meteor. Soc.*, **64**, 779-784.

Smith, W. L., and C. M. R. Platt, 1978: Intercomparison of radiosonde, ground based laser and satellite deduced cloud heights. *J. Appl. Meteor.*, **17**, 1796-1802.

Stone, R., S., G. L. Stephens, C. M. R. Platt and S. Banks, 1990: The remote sensing of thin cirrus cloud using satellites, lidar and radiative transfer theory, *J. Appl. Meteorol*, **29**, 353-366.

Stowe, L. L., McClain, E. P. Carey, R., et al. 1991: Global distributions of cloud cover derived from NOAA/AVHRR operational satellite data. *Adv. Space Res.*, **11**, 51-54.

Strabala, K. I., S. A. Ackerman and W. P. Menzel, 1994: Cloud properties inferred from 8-12 μm data. *Jour. Appl. Met.*, **2**,

Suomi, V. E., R. J. Fox, S. Limaye, and W. L. Smith, 1983: McIDAS III, a modern interactive data analysis facility. *J. Appl. Meteor.* **22**, 766-788.

Szejwach, G., 1982: Determination of semitransparent cirrus cloud temperature from infrared radiances: Application to METEOSAT. *J. Appl. Meteorol*, **21**, 384-393.

Takano, Y., K. N. Liou and P. Minnis, 1993: The effects of small ice crystals on cirrus infrared radiative properties. *J. Atmos. Sci.*, **49**, 1481-1493.

Wielicki, B. A., J. T. Suttles, A. J. Heymsfield, R. M. Welch, J. D. Spinhirne, M. L. Wu, D. O'C Starr, L. Parker and R. F. Arduini, 1990: The 27-28 October 1986 FIRE IFO cirrus case study: Comparison of radiative transfer theory with observations by satellite and aircraft. *Mon. Wea. Rev.*, **118**, 2356-2376.

8. LIST OF FIGURES

Figure 1. Frequency scatter diagram of the tri-spectral analysis of high clouds for the month of January 1994 The number of points at a given value of BT_8-BT_{11} and an associated BT_{11}-BT_{12} is represented by its color and size as denoted in the legend.

Figure 2. Same as figure 1 except for July 1993.

Figure 3. Tri-spectral diagram categorized as a function of latitude (rows) and the 11 μm brightness temperature (columns). Each of the 9 plots is an individual BT_{11}-BT_{12} versus BT_8-BT_{11} graph. The upper row are observations south of 20S, the middle are tropical observation between 20S and 20N and the bottom row are observations between 20N and 50N. The columns categorize by brightness temperature at 11 μm; these are, going from left to right, $BT_{11} \leq 210$, $210 < BT_{11} \leq 220$; $220 < BT_{11} \leq 230$ and $230 < BT_{11} \leq 240$. a) January 1994 and b) July 1993.

Figure 4. Relationship between BT_{11} and $BT_{3.7}$ for high clouds observed during January 1994 and July 1993. Due to solar reflection the relationships are depicted for day (left) and night (right) separately.

Figure 5. The geographic location (circles) of the negative differences of BT_{11}-$BT_{6.7}$ for HIRS/2 FOVs in the region between 45N and 45S. a) January 1994 and b) July 1993.

Figure 6. The difference between 11 and 6.7 μm brightness temperature (BT_{11}-$BT_{6.7}$) as a function of BT_{11} for January (top set) and July (bottom pair) for HIRS/2 observations made over water (left panel) and land (right panel).

Figure 7. Histogram of the SSMI derived rain-rates categorized by the difference between the VAS cloud top 11 μm and the 6.7 μm equivalent temperatures averaged over a 128 km geographic.

Figure 8. Effect of cloud variability (f) in the FOV on the brightness temperatures of 11 and 6.7 microns. Two clouds in the FOV are assumed, one with a temperature of 190K and the second having a temperature of 215K. f represent the 190K cloud fraction. The solid and dashed lines represent the $BT_{6.7}$ and BT_{11} observations as a function of f. The difference between the two brightness temperatures is the dotted line whose scale is the right-hand ordinate.

Figure 9. The geographic location of BT_{11}-$BT_{6.7}$ differences less than -5K for a single HIRS/2 FOV over the south-pole region during July 1993.

Figure 10. Brightness temperature differences between 3.7 and 11 μm versus the 11 μm brightness temperature (top) and 11 and 12 μm versus the 11 μm (bottom) brightness temperature for stratus off the west coast of North America. The ellipse encompasses most of the clear-sky observations. The diamonds indicate cloud values. The squares represent clear-daytime values and the circles are clear-nighttime derived values.

Figure 11. Brightness temperature differences between 3.7 and 11 μm versus the 11 μm brightness temperature for January (top) and July (bottom) brightness temperature for stratus off the west coast of South America. The ellipse encompasses most of the clear-sky observations. The open circles represent clear-daytime values and the filled triangles are clear-nighttime derived values.

Figure 12. Brightness temperature differences between 3.7 and 11 μm versus the 11 μm brightness temperature for January (top) and July (bottom) brightness temperature for stratus off the west coast of southern Africa. The ellipse encompasses most of the clear-sky observations. The squares represent clear-daytime values and the filled circles are clear-nighttime derived values.

Frequency Scatterplot JANUARY 1994

Legend:
- • 1 case
- ○ 2-16 cases
- ○ 17-31 cases
- ○ 32-46 cases
- ○ 47-61 cases
- ○ 62-76 cases
- ○ >76 cases

Axes: $BT_8 - BT_{11}$ (vertical), $BT_{11} - BT_{12}$ (horizontal)
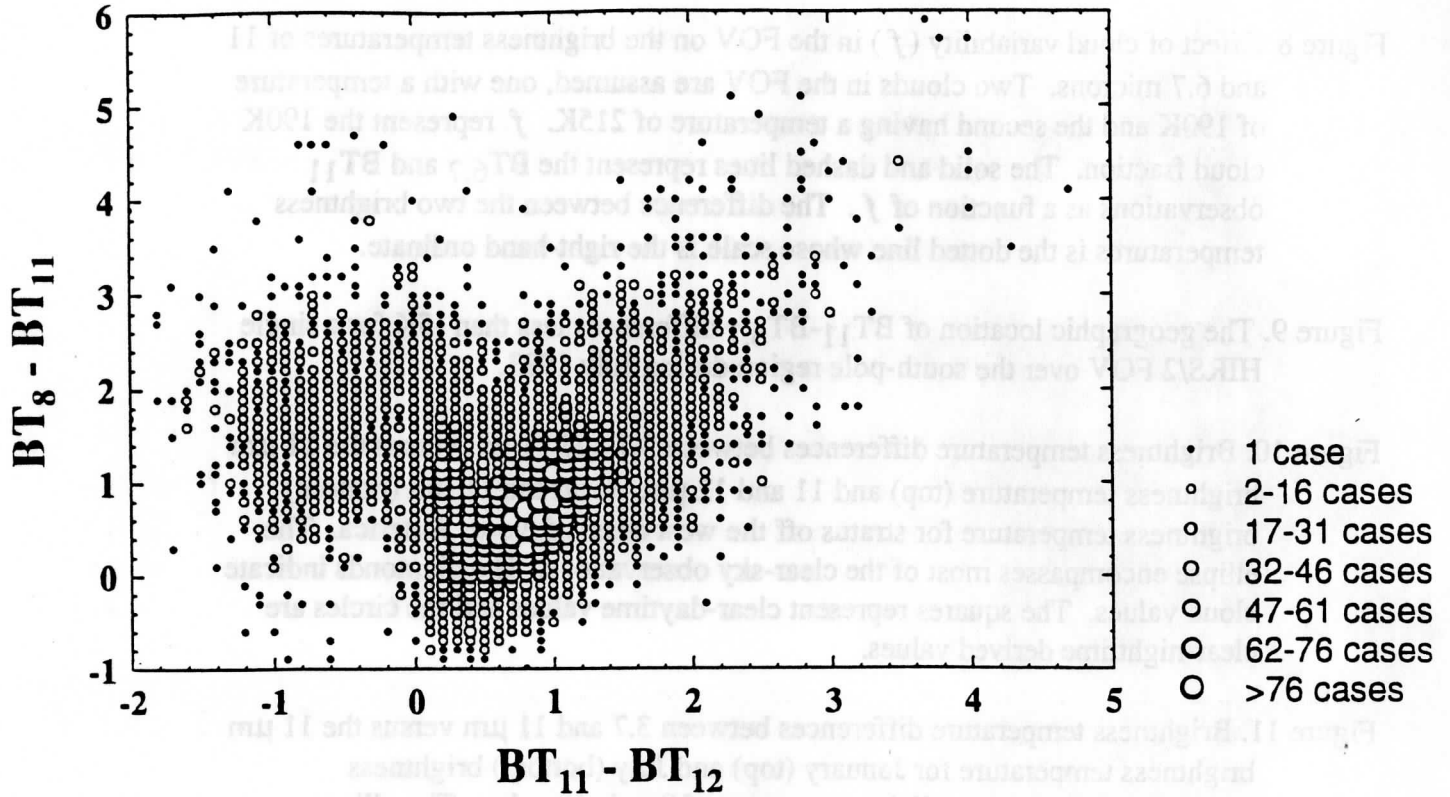
Frequency Scatterplot JULY 1993

JANUARY 1994

$BT_8 - BT_{11}$ (vertical axis)

LAT: $<= -20$

LAT: $(-20,20]$

LAT: > 20

BT_{11}: $<= 210$

BT_{11}: $(210,220]$

BT_{11}: $(220,230]$

BT_{11}: > 230
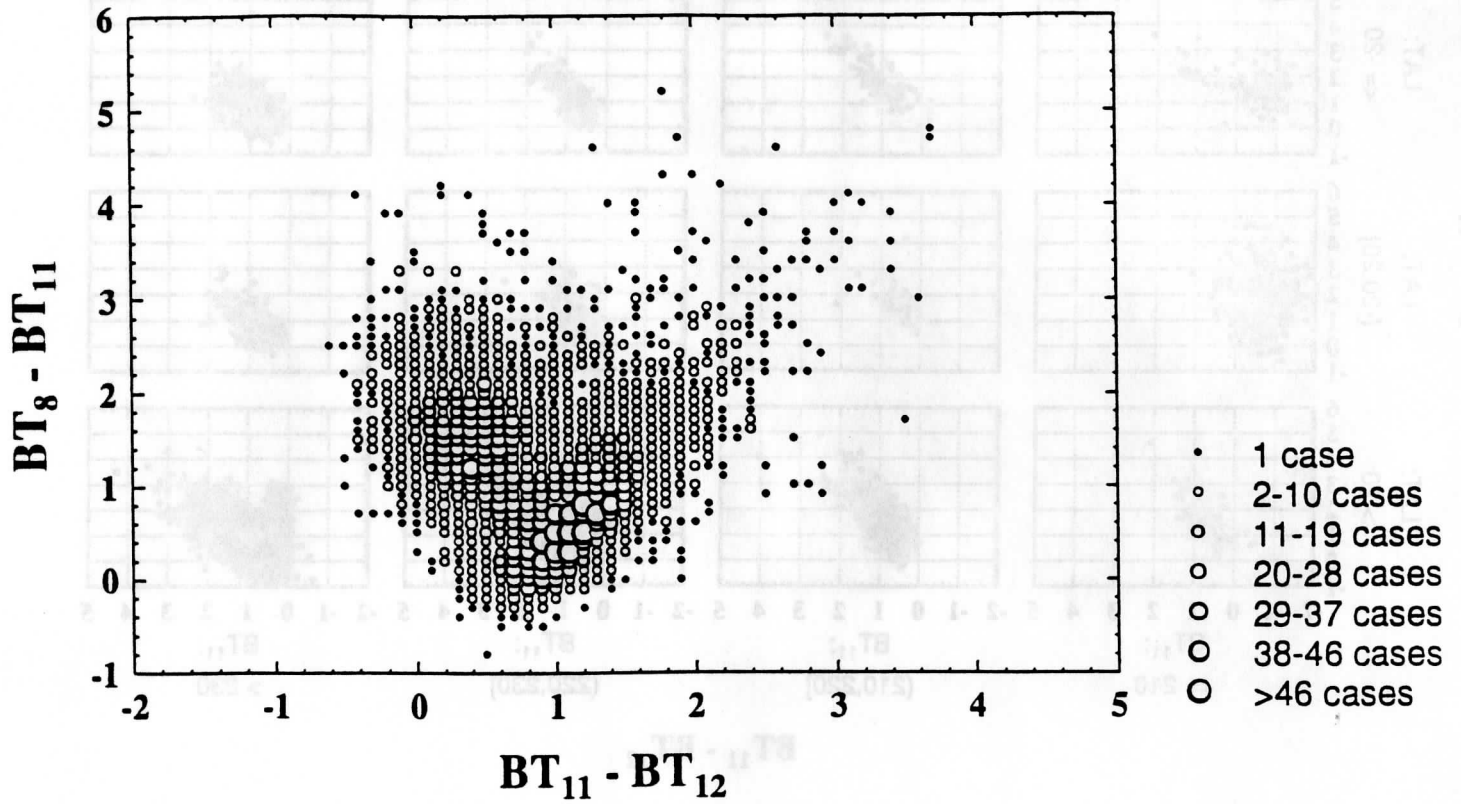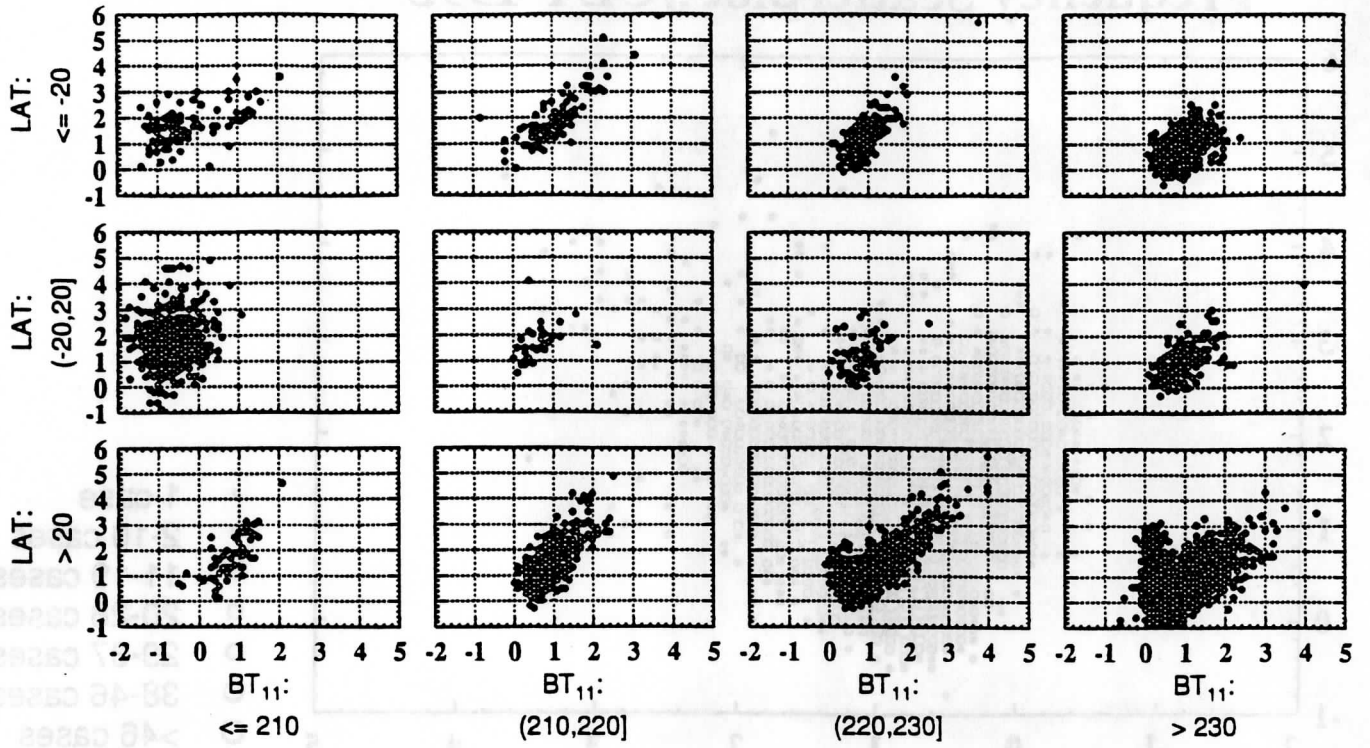
$BT_{11} - BT_{12}$

JULY 1993

BT$_8$ - BT$_{11}$
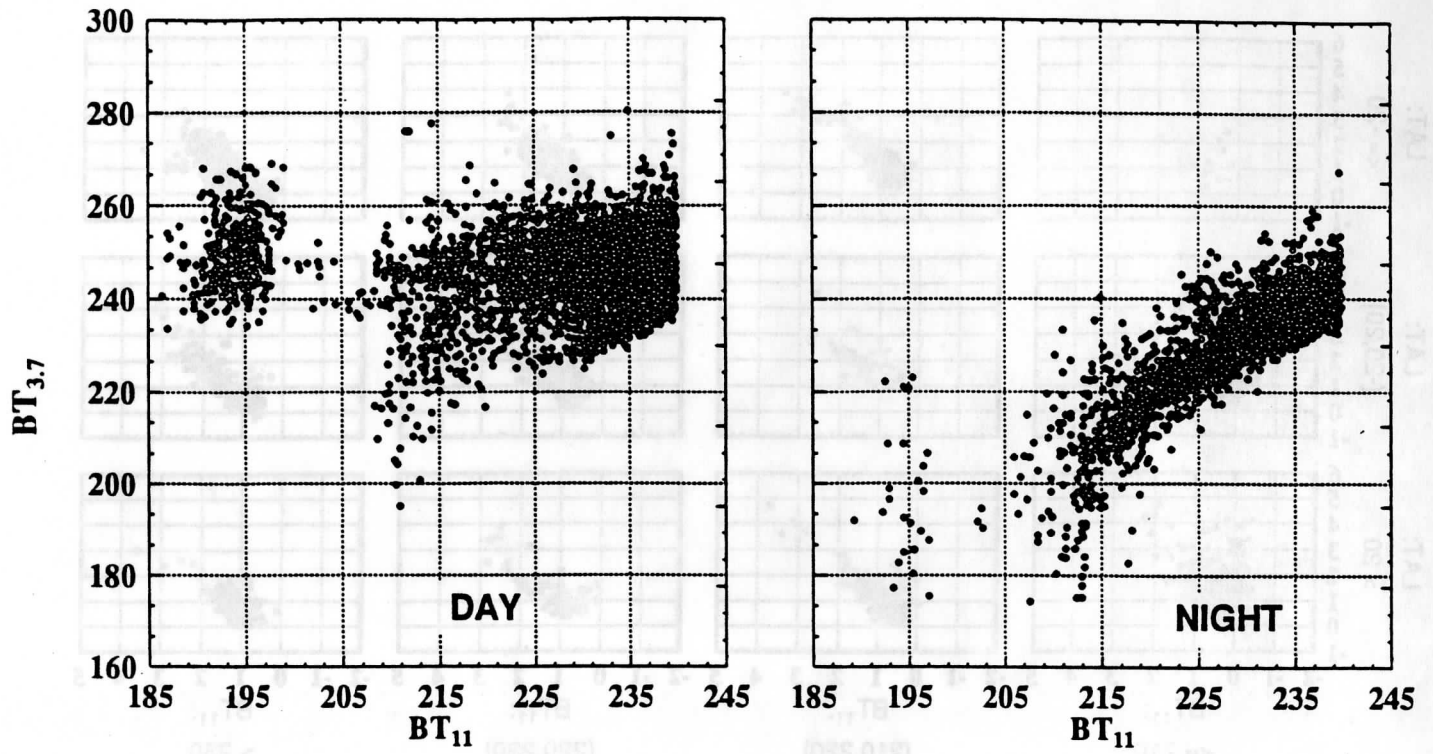
LAT: <= -20

LAT: (-20,20]

LAT: > 20

BT$_{11}$: <= 210

BT$_{11}$: (210,220]

BT$_{11}$: (220,230]

BT$_{11}$: > 230

BT$_{11}$ - BT$_{12}$

JANUARY 1994

JULY 1993
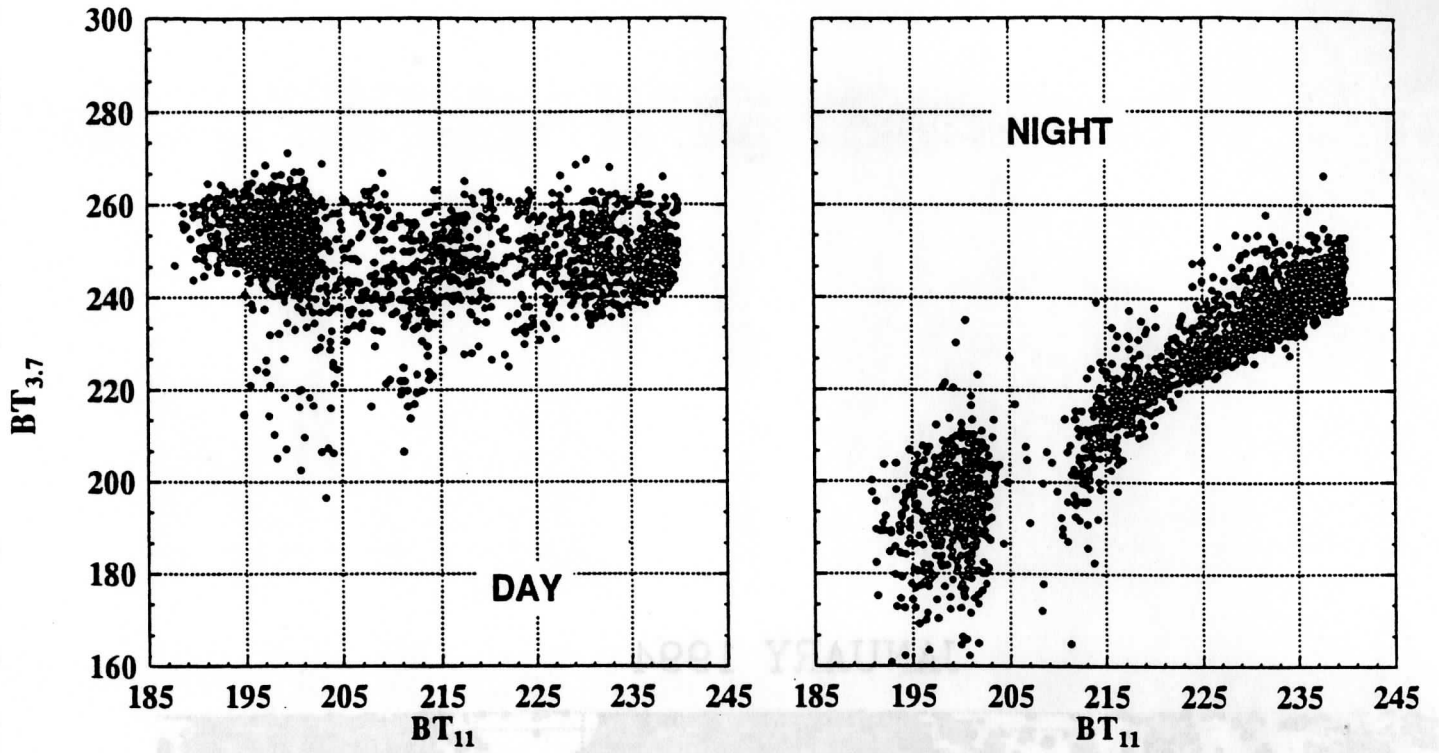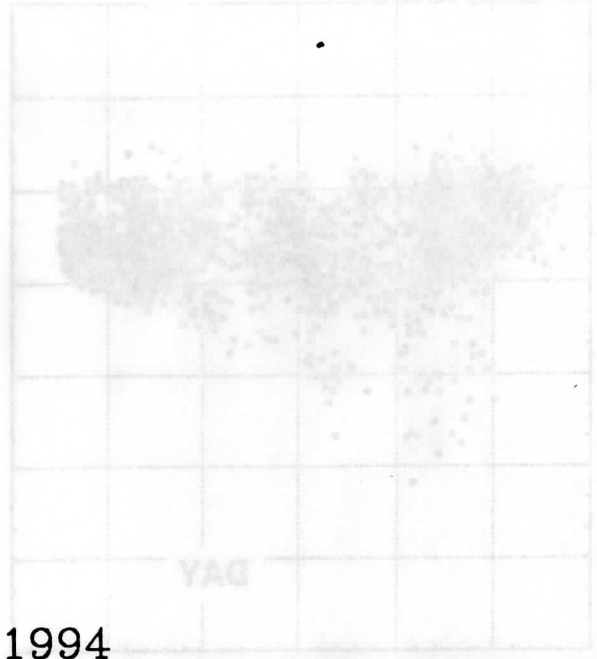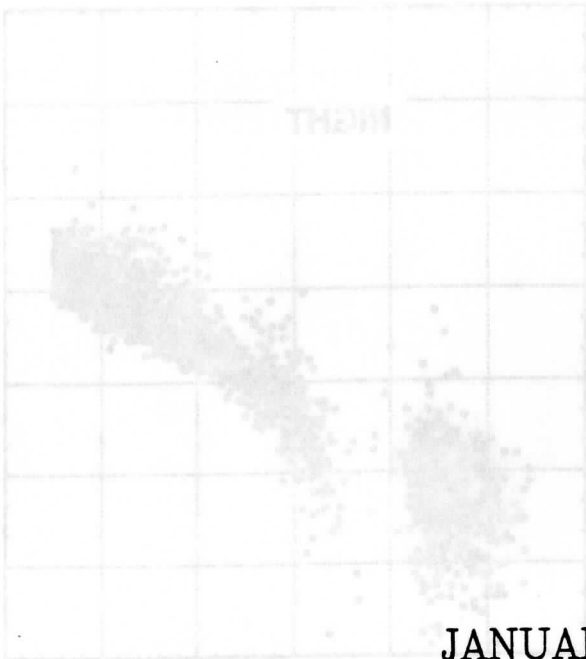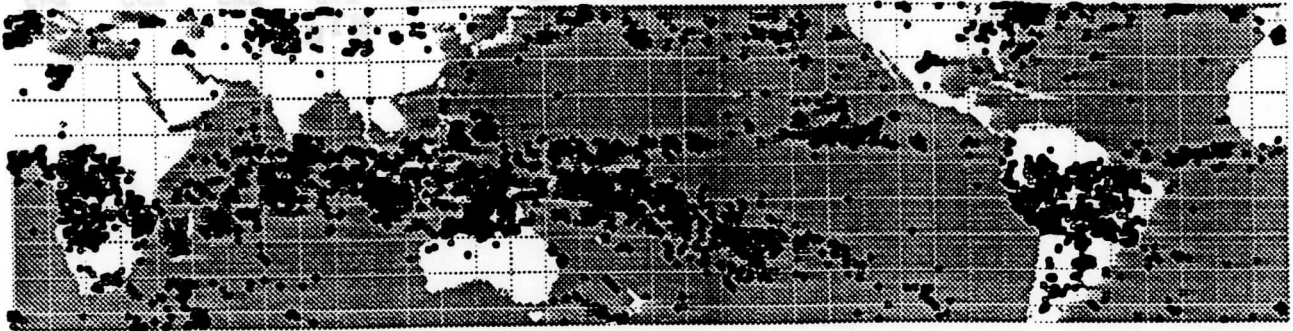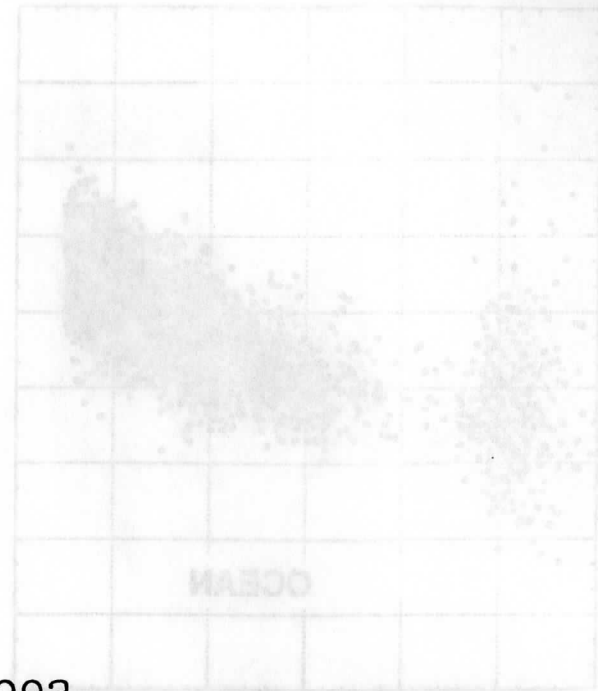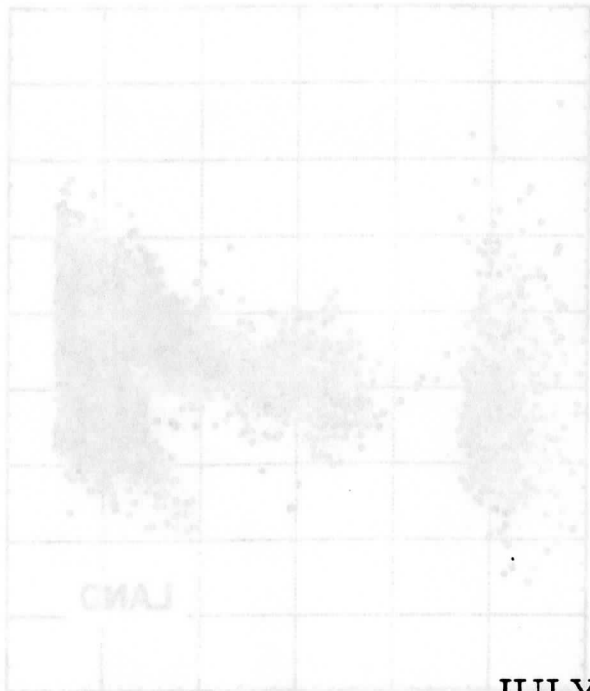
JANUARY 1994
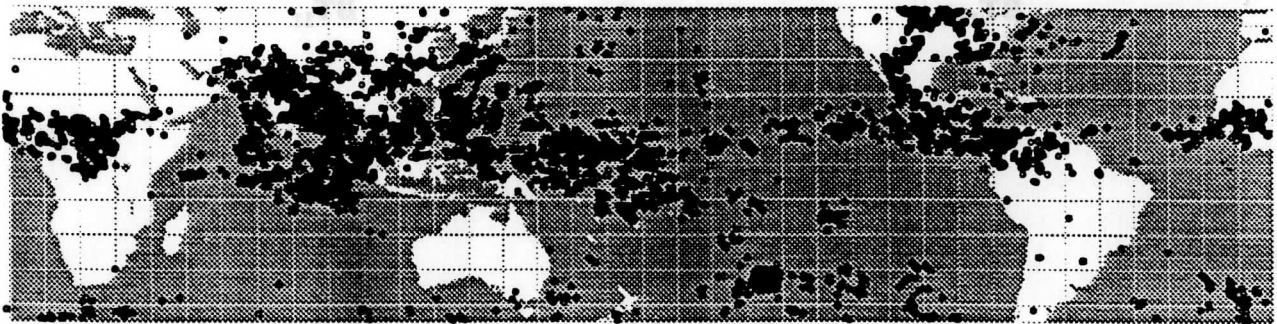
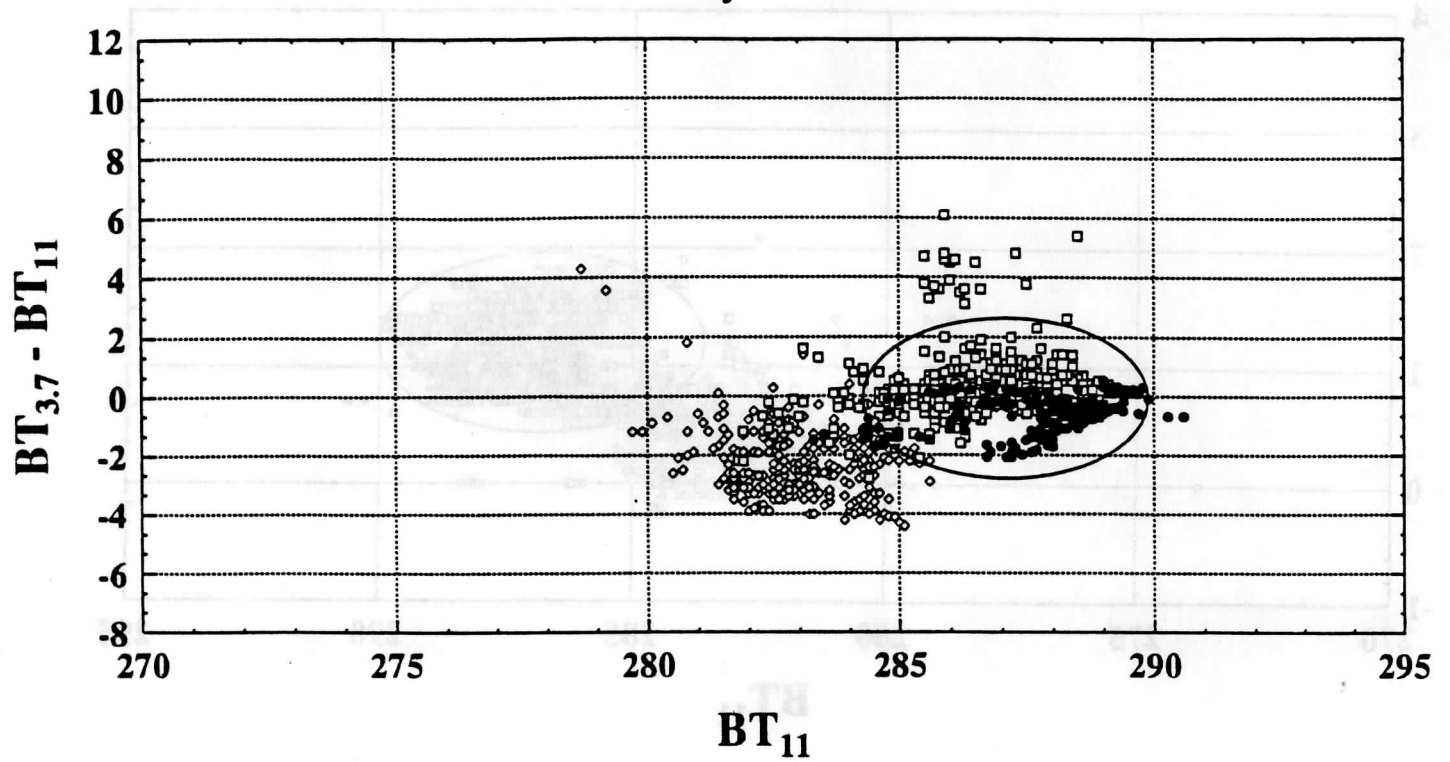JULY 1993
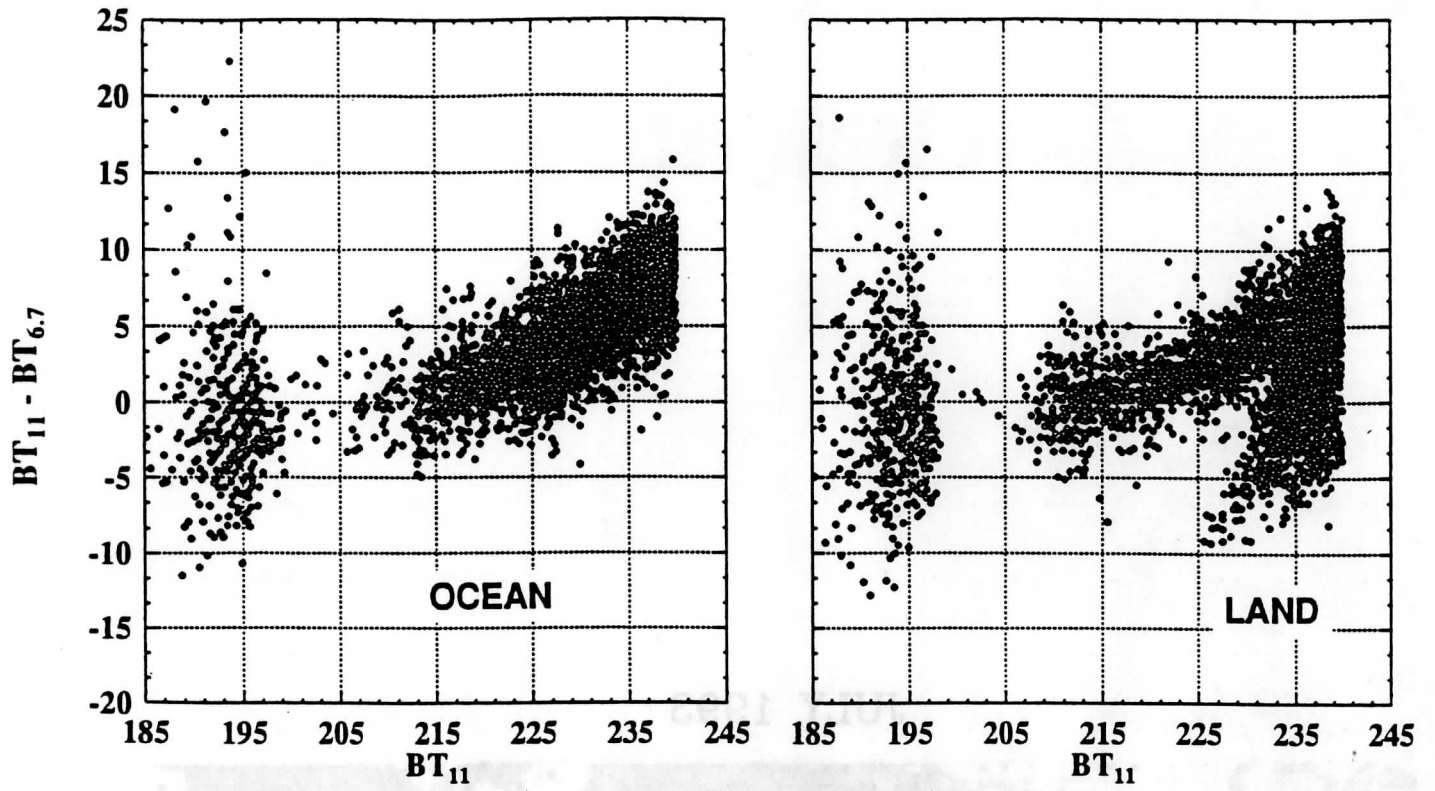
JANUARY 1994
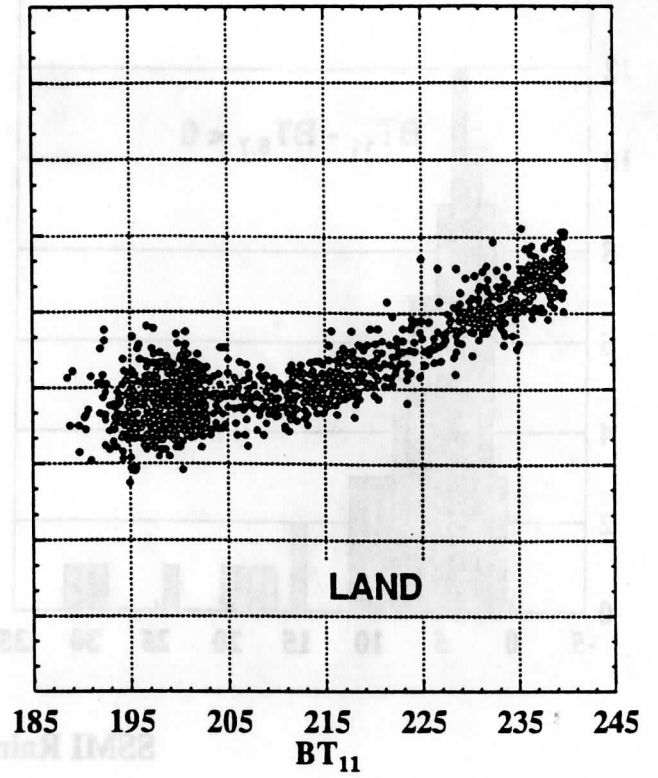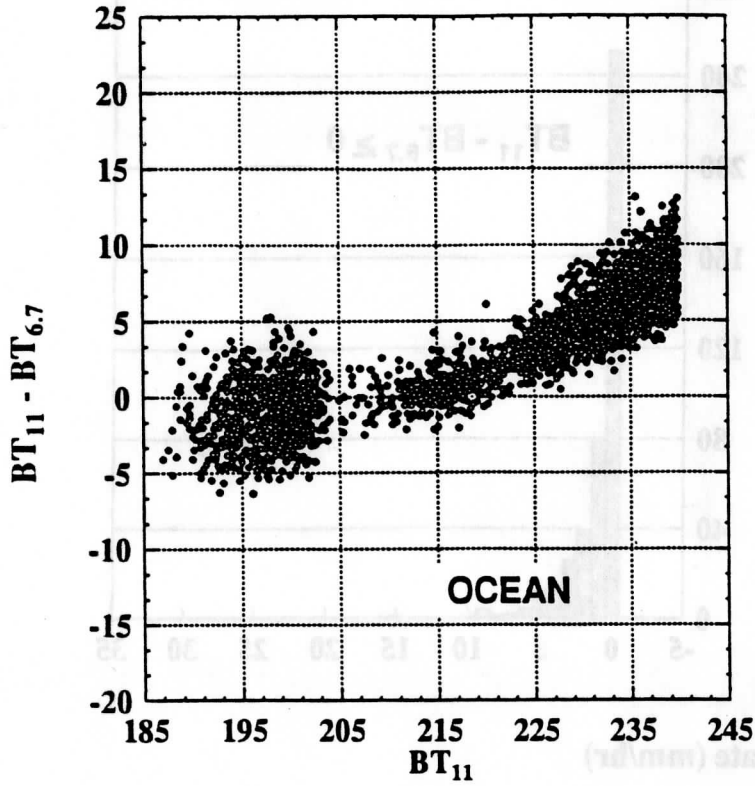
JULY 1993

Collocated GOES-7 and SSMI Observations
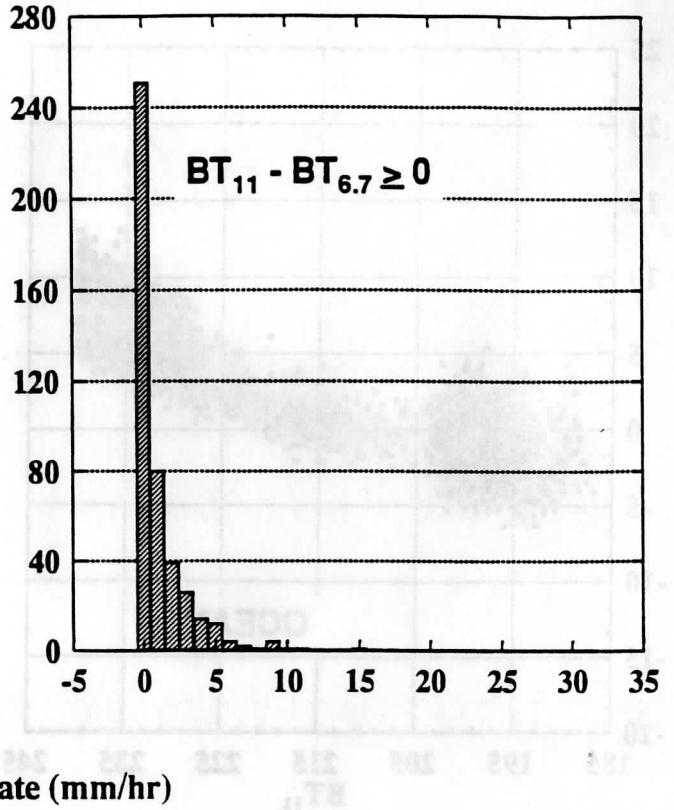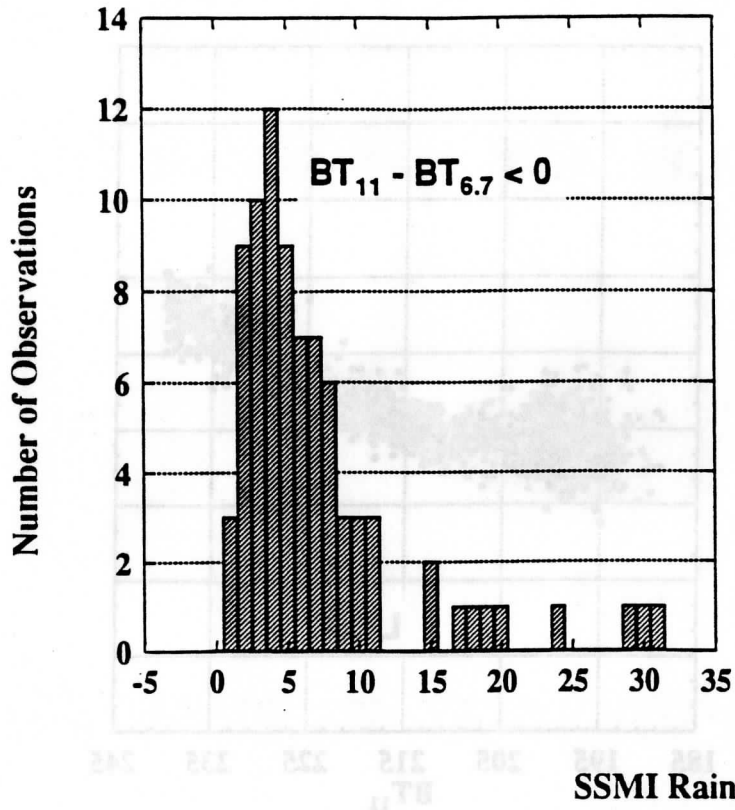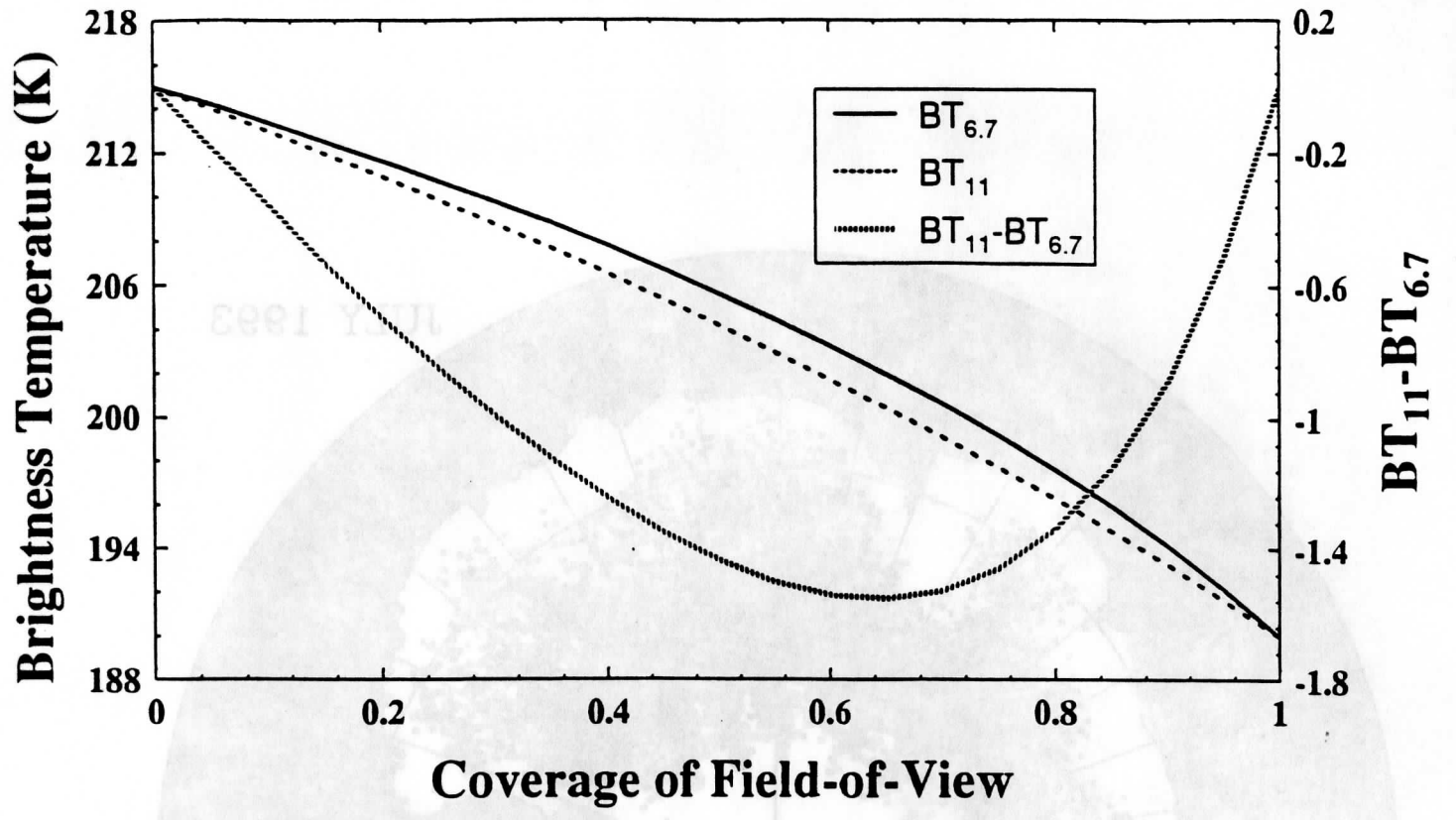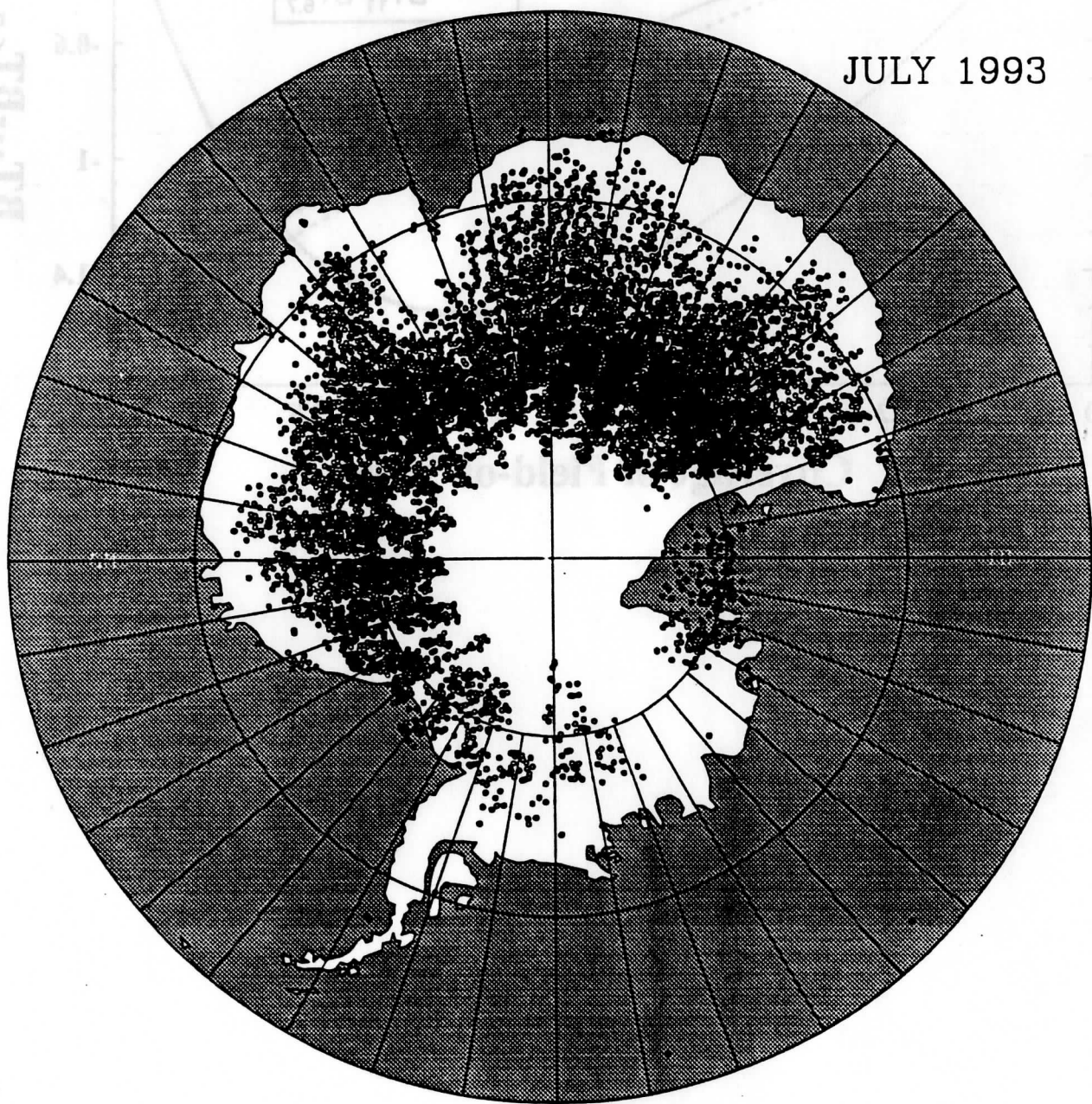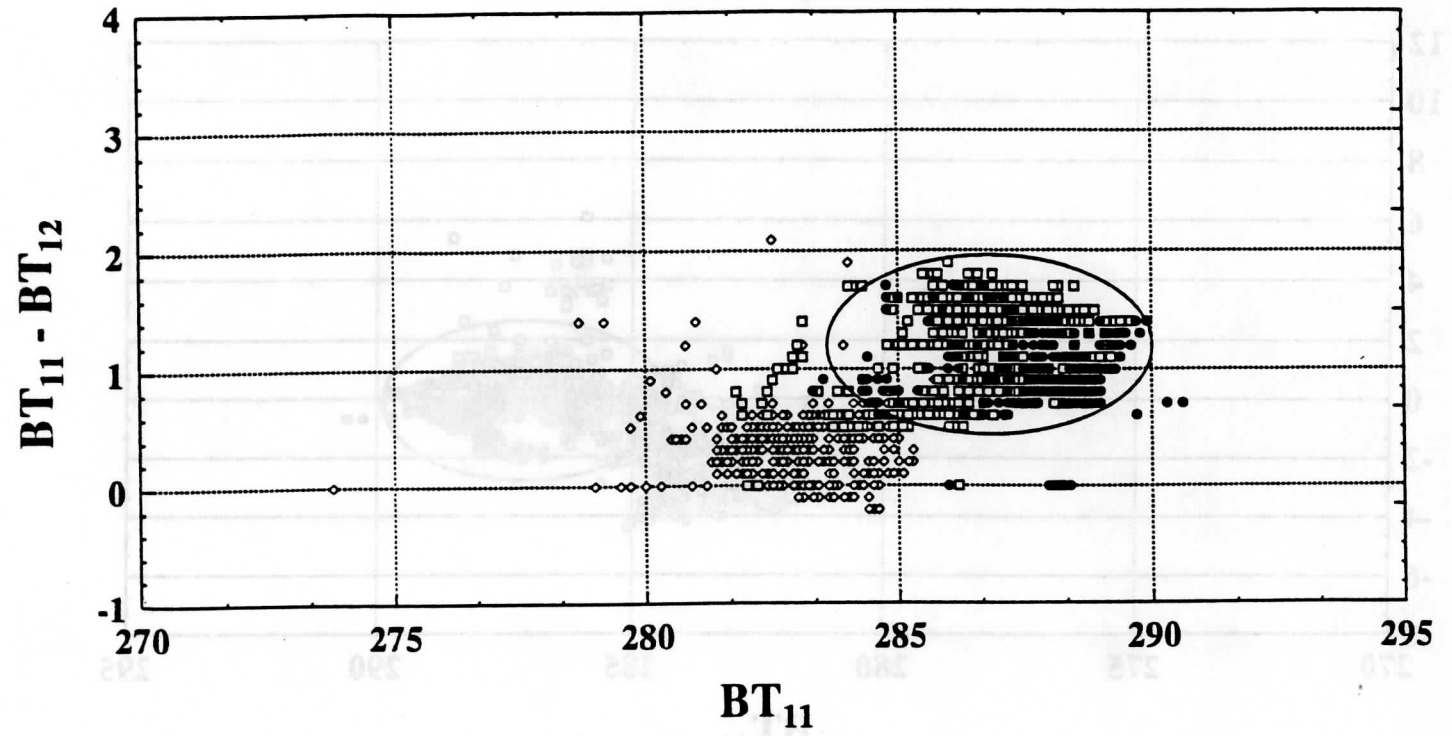

SSMI Rainrate (mm/hr)

7

Stratus off the West Coast of North America
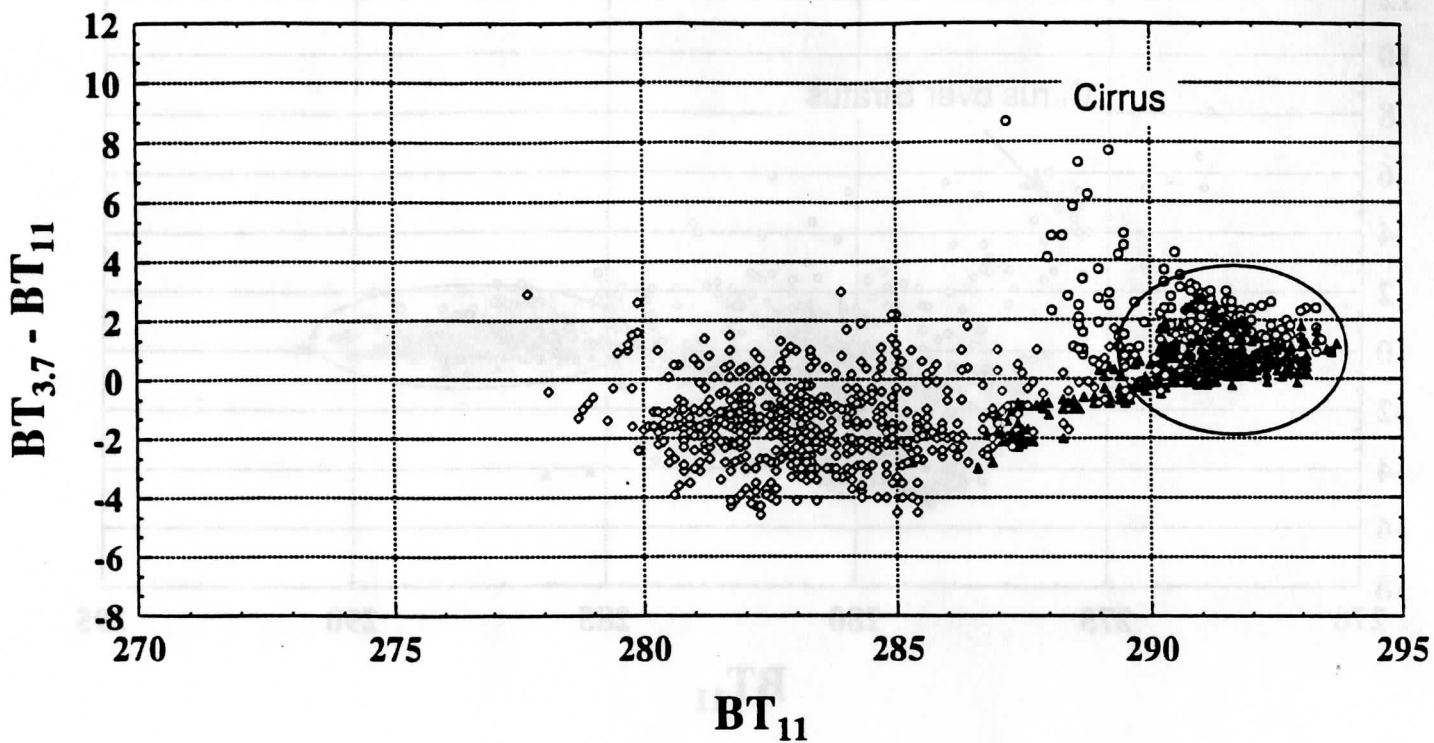## July 1993

10a

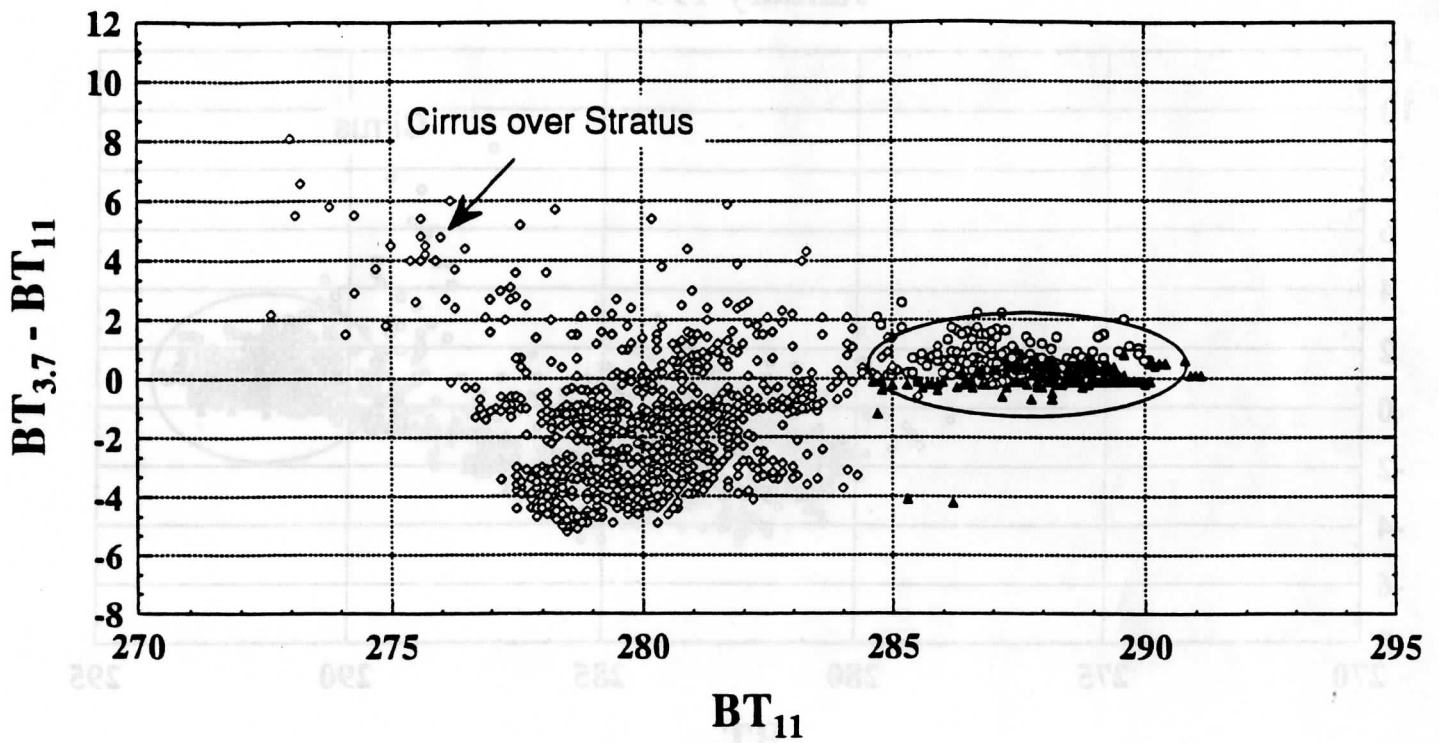# Stratus off the West Coast of North America
July 1993

Stratus off the West Coast of South America
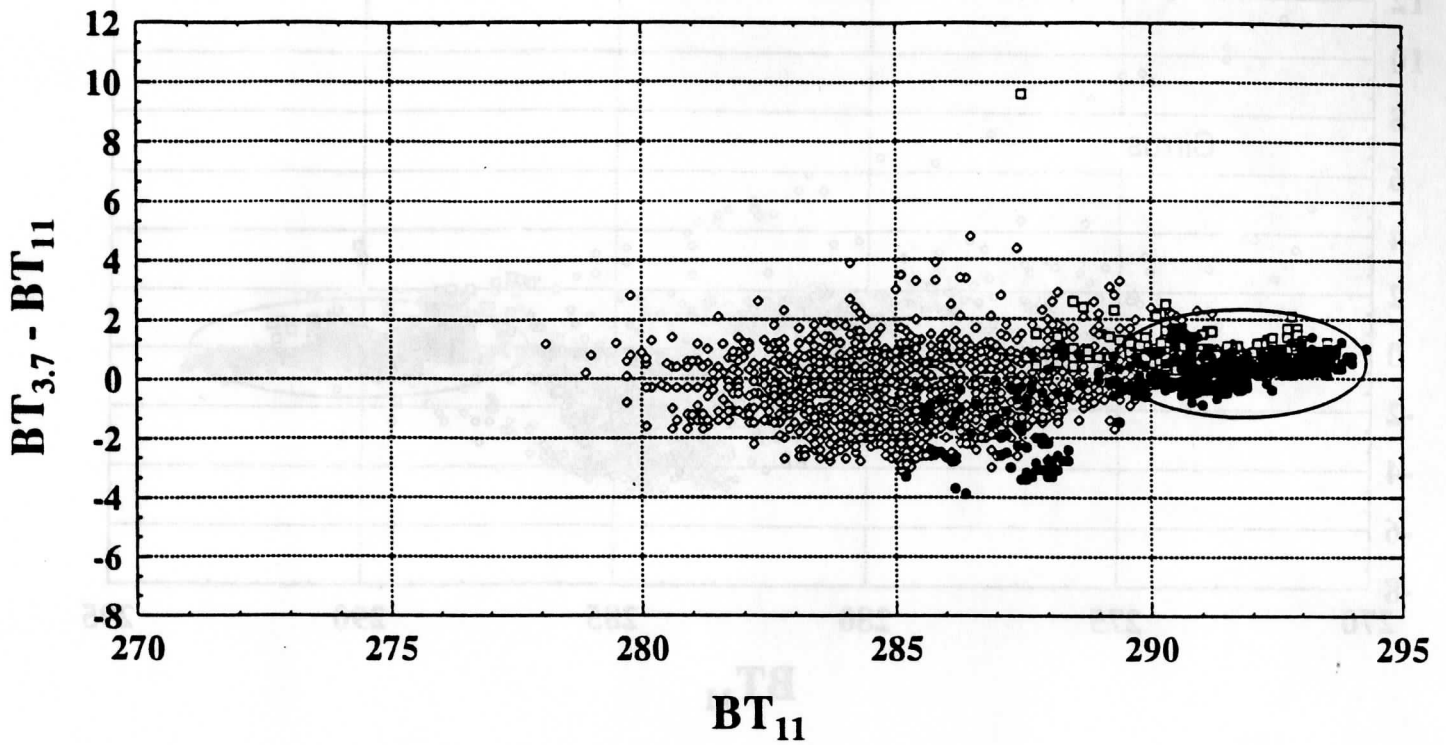## January 1994

Stratus off the West Coast of South America
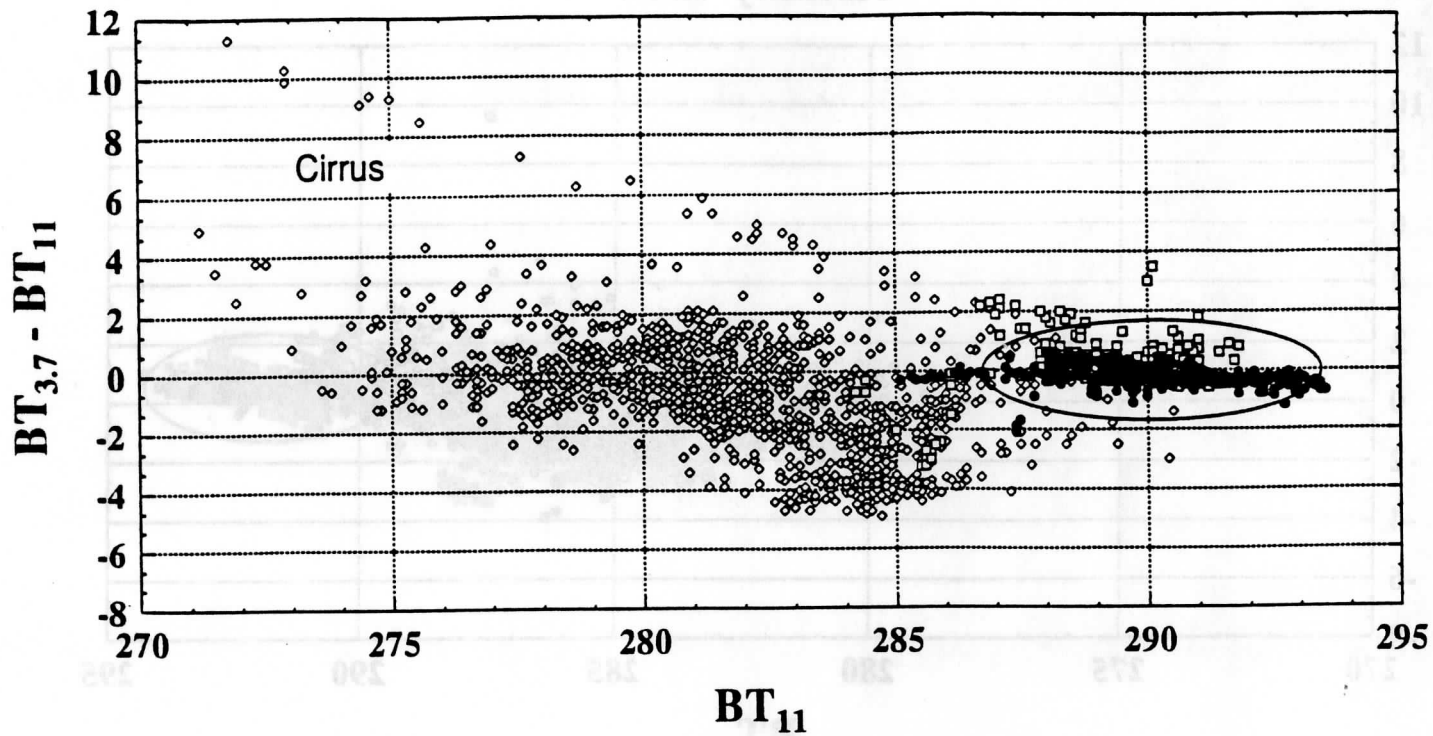## July 1993

Stratus off the West Coast of Africa
January 1994

12a

Stratus off the West Coast of Africa
July 1993

Satellite remote sensing of H_2SO_4 aerosol using the 8- to 12-μm window region: Application to Mount Pinatubo

Steven A. Ackerman and Kathleen I. Strabala

Cooperative Institute of Meteorological Satellite Studies, University of Wisconsin-Madison

Abstract. Monitoring stratospheric aerosols containing H_2SO_4 using the brightness temperature (BT) difference between 11 and 8.3 μm ($BT_8–BT_{11}$) spectral channels is demonstrated using theoretical calculations and satellite observations. Assuming an aqueous solution of 50% and 75% sulfuric acid, radiative transfer calculations indicate that over oceans an increase in the optical depth of the stratospheric aerosol results in an increase in $BT_8–BT_{11}$. Theoretical simulations suggest that the technique is sensitive to visible optical depths greater than approximately 0.15. The simulations also demonstrate a lack of sensitivity to the particle size distribution. Changes in pre- and post-Pinatubo observations by the HIRS2 on board the NOAA 10 are consistent with observed optical depth measurements and confirm the sensitivity of these channels to the presence of the aerosol. The technique is also applied to cold tropical convective clouds and desert regions where the signal, though evident, is less conclusive. Time series analysis is applied to the NOAA 10 and NOAA 12 combined $BT_8–BT_{11}$ observations to detect the periodicity of the spread of the volcanic aerosol. Over a region of the southern Pacific a 18- to 26-day period is present. Model simulations were conducted to demonstrate a trispectral technique with observations near 8, 11, and 12 μm. The trispectral approach has high potential in that the spectral signature of cirrus, water vapor, and H_2SO_4 aerosols are different. Observations from NOAA 10 and NOAA 11 are combined to demonstrate the capabilities of these infrared wavelengths of detecting the aerosol. The signal is clearly evident when a region of the South Atlantic is compared for pre- and post-Pinatubo conditions.

1. Introduction

Aerosols may affect climate directly by modifying the radiative energy distribution of the Earth-atmosphere system or indirectly through modification of cloud microphysical structure. The direct radiative effects will cool or warm the climate depending on the spectral variation of the aerosol absorption-to-backscatter ratio and the characteristics of the underlying surface (e.g., albedo and emissivity). Climate variations have been attributed to widespread distribution of volcanic aerosols [*Toon*, 1982; *Lamb*, 1970; *Kondratyev*, 1988].

The eruption of Mount Pinatubo on June 15–16, 1991, provides a unique observational opportunity to study the impact of the stratospheric aerosol on various climate parameters. *Bluth et al.* [1992] estimated that the Mount Pinatubo eruption injected 20 million metric tons of sulfur dioxide into the stratosphere. The SO_2 is converted to sulfuric acid-water (H_2SO_4-H_2O) aerosols. The growth of stratospheric dilute sulfuric acid particles and their dependence on temperature and humidity is discussed by *Steele et al.* [1983]. This volcanic stratospheric cloud quickly spread between 20°S and 50°N by the beginning of August [*Stowe et al.*, 1992]. The aerosol was observed over Laramie, Wyoming in July 1991 where balloon-borne observations indicated the Pinatubo cloud was composed largely of H_2SO_4-H_2O aerosols.

Several observational studies have addressed the potential climatic impact of this stratospheric aerosol. *Minnis et al.* [1993] used broadband radiative budget observations to demonstrate that the presence of the Mount Pinatubo aerosol layer increased the global albedo while decreasing the outgoing longwave radiation. The shortwave radiative forcing dominated, resulting in a net radiative cooling of the planet. *Chandra* [1993] concluded that a decrease in column ozone amount and a heating of the lower stratosphere resulted from the presence of the Mount Pinatubo aerosol. *Dutton and Christy* [1992] showed that the Pinatubo eruption resulted in a decrease in the monthly mean clear-sky total solar irradiance at the surface and a decrease in the ratio of direct to diffuse radiation.

Understanding the climatic implications of the aerosol requires global monitoring of its position and optical properties. Several methods exist for determining the presence of volcanic aerosol and its optical thickness from satellite radiance measurements. The most direct satellite observations of the aerosol are those provided by the Stratospheric Aerosol and Gas Experiment (SAGE). The disadvantage of the SAGE lies in its time sampling and that it saturates for vertical optical depths (at 0.55 μm) of approximately 0.2. The reflectance channels of the advanced very high resolution radiometer (AVHRR) are used by the National Oceanic and Atmospheric Administration (NOAA) to routinely monitor aerosols over oceans [*Rao et al.*, 1989]. This approach was extremely successful in monitoring the Mount Pinatubo aerosol [*Stowe et al.*, 1992]. The disadvantage of this approach is that it works only during the day, not an extreme

Table 1. Optical Parameters Used in the Theoretical Modeling Sensitivity Analysis

Solution, %	Size Distribution	λ, μm	Index of Refraction	Single-Scattering Albedo	Asymmetry Parameter	σ_{ir}/σ_{vis}
75	*Pueschel et al.* [1993]	8.3	1.241–i0.68	0.038918	0.063813	0.221
		11.1	1.738–i0.463	0.039496	0.047155	0.0818
		12.5	1.757–i0.158	0.062164	0.038610	0.0251
50	*Pueschel et al.* [1993]	8.3	1.28–i0.48	0.032180	0.067765	0.1535
		11.1	1.484–i0.311	0.024629	0.042260	0.0653
		12.5	1.549–i0.210	0.027142	0.034665	0.0373
75	*Deshler et al.* [1992]	8.3	1.241–i0.68	0.027060	0.051691	0.199
		11.1	1.738–i0.463	0.026949	0.038565	0.0719
		12.5	1.757–i0.158	0.042486	0.031630	0.0219

disadvantage in monitoring stratospheric aerosols, and is most effective over low-albedo surfaces such as the ocean. Brightness temperature (BT) differences between 11-μm and 12-μm channels have also been used in limited studies of monitoring volcanic aerosols [e.g., *Prata*, 1989; *Barton et al.*, 1992]. More recently, *Baran et al.* [1993] presented a satellite detection method using observations at 8.3 and 12.5 μm. This paper suggests a similar approach using observations near 8, 11, and 12 μm. The technique is demonstrated with observations made by the High-Resolution Infrared Sounder 2 (HIRS2) on the NOAA satellites to monitor the Mount Pinatubo aerosol. Because no present-day satellite-borne instrument has all three channels, we first investigate the effects of the aerosol on the 8- and 11-μm channels before assessing the three-channel combination using collocated observations made on different satellite platforms.

2. Model Simulations

The proposed technique is physically based on the spectral variation of the aerosol inherent optical properties in the 8- to 12-μm region. The index of refraction of an aqueous solution of sulfuric acid differs considerably across this atmospheric window region. The imaginary part, an indication of the absorption properties, is approximately 50% larger at 8.3 than at 11 μm. Spectral variations exist in the real part as well.

The parameters needed to determine the radiative properties of an aerosol layer are (1) extinction coefficient (σ_{ext}), which integrated over the pathlength gives the optical thickness (τ); (2) the single-scattering albedo (ω_0); (3) and the phase function, or if one is interested in fluxes, the asymmetry parameter (g). Given these single-scattering properties of the aerosol, in addition to the radiative characteristic of the molecular atmosphere, the layer reflectance, transmittance, and absorption may be determined.

Determination of the radiative properties of aerosols for satellite monitoring or climate studies provides a particularly challenging problem: as the aerosol outbreak undergoes its life cycle, its chemical and physical properties change, thereby changing its radiative characteristics. As a sensitivity analysis of the aerosol effects on simulated satellite observations, we assume three representative distributions. To assess the effect of aerosol composition, we assume two solutions of sulfuric acid in water (75 and 50%) and use the index of refraction reported by *Palmer and Williams* [1975].

Particle size distributions of stratospheric aerosols are often expressed as lognormal distributions of the form

$$\frac{dN(r)}{dr} = \frac{N_0}{r \ln \sigma_g \sqrt{2\pi}} \exp\left[-\frac{1}{2}\left(\frac{\ln r - \ln r_g}{\ln \sigma_g}\right)^2\right]$$

To assess the impact of varying size distribution, we assume a 75% solution using the measured distributions of *Deshler et al.* [1992] and *Pueschel et al.* [1993]. Pueschel et al. collected information on the particle size distribution of the stratospheric aerosols from the NASA ER-2 between August 1991 and March 1992. Observations at altitudes between 16.5 and 20 km indicated a bimodal distribution which they fitted with two lognormal curves with the following parameters: for the small particle mode, $N_{0_1} = 2.3$ cm^{-3}, $r_{g1} = 0.1$ μm, and $\sigma_{g1} = 1.4$; for the large particle mode, $N_{0_2} = 1.3$ cm^{-3}, $r_{g2} = 0.3$ μm, $\sigma_{g2} = 1.6$. The second distribution is based on the balloon-borne measurements of *Deshler et al.* [1992] over Laramie, Wyoming. Table 1 summarizes the single-scattering properties at the three wavelengths of interest, calculated using Mie theory. At all wavelengths the ω_0 is nearly zero. σ_{ir}/σ_{vis} is the ratio of the volume cross section at the given infrared wavelength normalized to the volume cross section at a wavelength of 0.5 μm. For a given optical depth at 0.5 μm, extinction will be much larger at 8.3 μm than at 11.1 μm or 12.5 μm. Changing the size distribution slightly modifies the optical parameters, indicating the potential difficulty of the method for inferring particle size distribution of the aerosol.

Assuming azimuthal symmetry, the infrared radiative transfer equation for a horizontally homogeneous layer is

$$\mu \frac{dI(\tau, \mu)}{d\tau} = I(\tau, \mu) - (1 - \omega_0)B(T) - \frac{\omega_0}{2}\int_{-1}^{1} P(\mu; \mu')I(\tau, \mu')\,d\mu'$$

where τ is the optical depth, $I(\tau, \mu)$ is the radiance from direction μ, and $B(T)$ is the Planck function. We assume boundary conditions of no downward radiance incident on the top of the aerosol layer, and the upward radiance at the base of the aerosol layer is what is typically observed by the HIRS2 over clear-sky tropical ocean conditions. Satellite spectral observations are simulated by solving the radiative

Theoretical Simulations
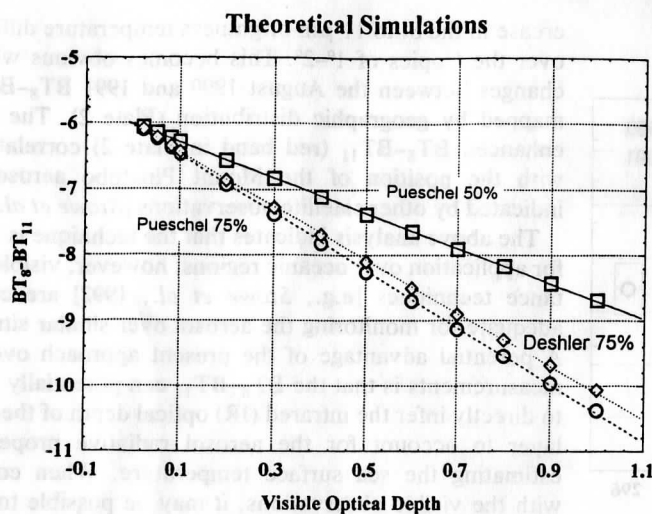
Figure 1. Theoretical simulation of brightness temperature (BT) difference between 8.3 and 11.1 μm (BT_8–BT_{11}) and optical depth at a wavelength of 0.55 μm. The three different curves represent the three distributions listed in Table 1.

transfer equation using a doubling/adding model. A version of this model was used by *Ackerman* [1989] to assess the capabilities of a two-channel dust detection algorithm and by *Ackerman and Chung* [1992] to investigate the broadband properties of dust. Results are presented for the nadir view angle only. For the purposes of demonstrating the technique, we assume the aerosol layer is uniformly distributed between 20 and 25 km and an atmospheric temperature profile of the standard tropical atmosphere [*McClatchy et al.*, 1972]. SAGE and lidar observations generally observe the aerosol to be near these altitudes, though the aerosol is generally not well mixed. Figure 1 depicts the model brightness temperature difference between 8.3 and 11 μm (BT_8–BT_{11}) as a function of optical depth at 0.5 μm. The three lines represent the radiative transfer calculations using the three aerosol distributions of Table 1. As the optical depth is small, there is a linear relationship between the aerosol radiative properties and visible optical depth. The slope of the brightness temperature difference for the different distributions results from the differences in extinction at the two infrared wavelengths. It is difficult to distinguish the calculations for the different size distributions with the same solution. The 50 and 75% solutions can be distinguished for larger optical depths. For visible optical depths between 0.2 and 0.3, a typical range observed by *Stowe et al.* [1992], the BT_8–BT_{11} ranges from 1° to 1.5°C smaller than the clear-sky case for the 75% solution and from 0.5° to 1.0°C for the 50% solution. For thick aerosol layers, if the visible optical depth is known, the simulations indicate a possibility of estimating the dilution of the sulfuric acid particles.

3. HIRS2 Observations

Further sensitivity studies of the aerosol impact on satellite observations can be undertaken using this modeling approach. At this point we choose to explore the technique discussed above using global satellite observations. While several aerosol detection techniques have been developed using observations from the AVHRR, few aerosol retrieval techniques have been proposed using HIRS2 data (*Baran et*

NOAA 10; No Aerosol
45-35S; 0-30W
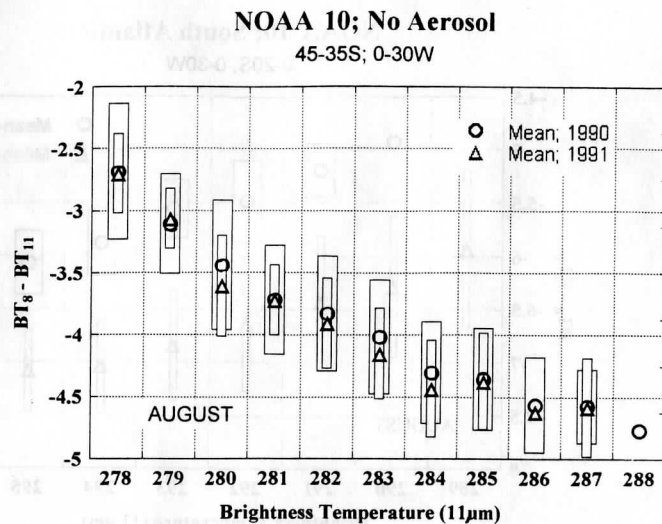
Figure 2. Box diagram of the BT_8–BT_{11} versus the 11-μm brightness temperature for the geographic regions 45°–35°S and 0°–30°W for the month of August. The symbols represent the mean for that year (circles, 1990; triangles, 1991) and the rectangles the standard deviation (wide box for 1990, narrow box for 1991).

al. [1993] recently proposed one such technique). A disadvantage of the HIRS2 is its spatial resolution, approximately 17 km at nadir; however, the HIRS2 possesses many more spectral channels than the AVHRR, both in atmospheric windows and in atmospheric absorption bands. The 20 spectral channels of the HIRS2 were selected to provide information on the atmospheric temperature and moisture structure and ozone content of the atmosphere and is the only present-day satellite-borne instrument with an spectral channel near 8.3 μm. This instrument was flown on the NOAA 10, NOAA 11, and NOAA 12 satellites, though the NOAA 11 HIRS2 had the 8.3-μm channel replaced with a 12-μm channel.

3.1. Bispectral Observations

Clear-sky ocean scenes. Observations from the NOAA 10 are used in this section as it was operational prior to and after the explosion of Mount Pinatubo. We begin by analyzing the brightness temperature differences at 8.3 and 11.1 μm (BT_8–BT_{11}) as a function of the 11-μm brightness temperature (BT_{11}) for ocean regions only. Surface spectral emissivities for the ocean are nearly one at both wavelengths. We consider individual HIRS2 observations within 10° of nadir that have been cloud cleared based on the cloud climatology algorithm described by *Wylie and Menzel* [1989]. The 11.1-μm channel is largely a window channel and the observed radiance has a strong contribution from surface-emitted radiation; while the 8.3-μm channel is sensitive to low tropospheric water vapor concentrations. Figure 2 depicts the relationship between BT_8–BT_{11} and BT_{11} for August 1990 and 1991 for the region 35°–45°S and 0°–30°W. Based on SAGE observations, this region had very little Mount Pinatubo aerosol present at this time. The values of BT_8–BT_{11} were averaged over 1°K intervals of BT_{11}, and Figure 2 depicts the mean (circle, 1990; triangle, 1991) and standard deviation (wide box for 1990, narrow box for 1991). The slope of the mean BT_8–BT_{11} as a function of BT_{11}

NOAA 10; South Atlantic
0-20S; 0-30W
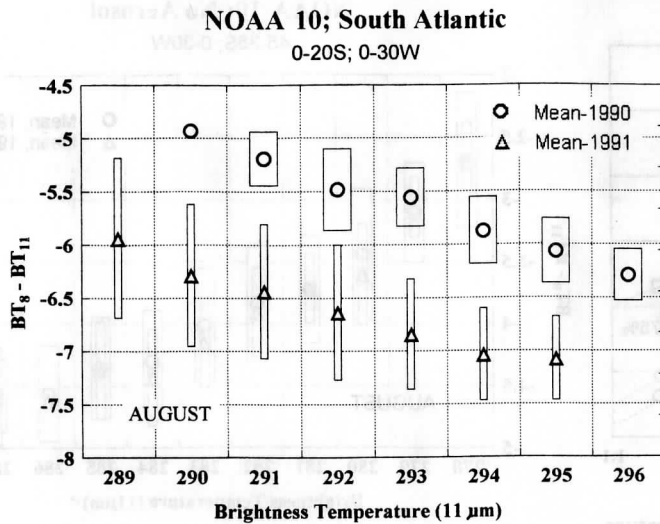
Figure 3. Same as Figure 2 except for the regions 0°–20°S and 0°–30°W.

results from the strong coupling between total atmospheric precipitable water and sea surface temperature [*Stephens*, 1990]. Increases in sea surface temperature (SST) result in an increase in BT_{11}. The larger atmospheric water vapor associated with the increased SST results in a smaller BT_8–BT_{11}. The relationship between BT_8–BT_{11} and BT_{11} does not change between the two years, lending confidence to the stability of the instrument. The standard deviation is similar between the two years. The only difference between the two years is the warm 288°K BT_{11} values observed in 1990 that were not observed in 1991.

An analysis of BT_8–BT_{11} versus BT_{11} for a region SAGE observed to be contaminated by the Mount Pinatubo aerosol (0°–20°S and 0°–30°W) is shown in Figure 3 as a box diagram similar to Figure 2. The slope observed in August 1990 results from the effects of water vapor and its relationship to SST. For August 1991 there is a significant decrease in BT_8–BT_{11} for every catagory of BT_{11}. Generally, the mean value decreases by approximately 1°–1.5°K. Referring back to Figure 1, this increase corresponds to a visible optical depth of 0.2–0.5, depending on the solution assumed. The corresponding infrared optical depths for 8.3 and 11.1 µm is 0.03–0.06 and 0.014–0.02, respectively. Not only do the BT_8–BT_{11} means for each year lie outside the standard deviation of the other year but there is also little overlap in the standard deviation observed between the two years. The standard deviation for the 1990, pre-Pinatubo, is approximately ±0.25°K and approximately doubles in post-Pinatubo year. This is expected as the aerosol layer was not uniformly distributed in space or time, resulting in a larger standard deviation. While we expect the presence of the stratospheric aerosol to decrease the mean BT_8–BT_{11} and increase the standard deviation, it does not affect the slope of BT_8–BT_{11} versus BT_{11}, which is driven by the underlying water vapor distribution and its relation to SST.

To further demonstrate the difference between the BT_8 minus the BT_{11} values due to stratospheric aerosol, we composited the brightness temperature differences for 2° × 3° latitude/longitude boxes for August 1990 and 1991 (Plate 1). Regions of yellow have BT_8–BT_{11} averages of −8° or smaller. After the Mount Pinatubo eruption there is a de-

crease in the 8- to 11-µm brightness temperature differences over the tropics of 1°–2°. This becomes obvious when the changes between the August 1990 and 1991 BT_8–BT_{11} are mapped by geographic distribution (Plate 2). The zonally enhanced BT_8–BT_{11} (red band in Plate 2) correlates well with the position of the Mount Pinatubo aerosol layer indicated by other satellite observations [*Stowe et al.*, 1992].

The above analysis indicates that the technique is suitable for application over oceanic regions; however, visible reflectance techniques [e.g., *Stowe et al.*, 1992] are certainly adequate for monitoring the aerosol over similar situations. A potential advantage of the present approach over solar measurements is that the BT_8–BT_{11} can potentially be used to directly infer the infrared (IR) optical depth of the aerosol layer to account for the aerosol radiative properties in estimating the sea surface temperature. When combined with the visible observations, it may be possible to infer a gross estimate of the composition. For example, *Stowe et al.* [1992] derived an August mean aerosol optical thickness of approximately 0.3–0.4 for the zonal band 0°–20°N. To have a mean brightness temperature difference of 1°–1.5° requires a 50–75% solution of H_2SO_4/H_2O. The present approach also has the capability to study aerosols over surfaces with high albedos, such as deserts and tropical convective systems. This is explored in the sections below.

Tropical convective scenes. *Minnis et al.* [1993] presented a unique study of the impact of Mount Pinatubo aerosol on the energy budget at the top of the atmosphere using wide field of view radiative flux measurements. The largest regional differences in the net radiation between pre- and post-Pinatubo analysis were for the Amazon and Congo basins, regions with frequent deep convective storms, and clear-sky ocean scenes. Differences over the deep convective scenes can be caused by the direct radiative effect of the aerosol, as in the clear-sky ocean case, or by an indirect effect through modification of the cloud microphysical properties. *Minnis et al.* [1993] suggest that this later effect would be more prominent in the shortwave than in the longwave and may be responsible for the large difference observed in the net radiation. *Ackerman et al.* [1990] and *Strabala et al.* [1994] demonstrated that the BT_8–BT_{11} is also sensitive to the particle size distribution of an ice cloud, though not so sensitive as the shortwave reflectance. While inclusion of an H_2SO_4 aerosol layer in the stratosphere drives BT_8–BT_{11} to smaller differences, a reduction in the effective radius of the particle size distribution makes the BT_8–BT_{11} less negative. Figure 4 is an analysis of BT_{11} versus BT_8–BT_{11} for August 1990 and 1991 for the Amazon region for conditions in which the CO_2 slicing method inferred overcast cloud conditions [*Wylie and Menzel*, 1989]. In this analysis the 11-µm observations were grouped in intervals of 5°K. For low clouds (BT_{11} greater than 270°K) there tends to be agreement with the clear-sky ocean case; the post-Pinatubo year has smaller BT_8–BT_{11} by 1°–2°C. As the cloud gets higher, this difference between the years tends to zero. This tendency is also observed in a scatter diagram of the two parameters, as depicted in Figure 5 where 1990 observations are denoted with circles, and squares represent 1991 observations. The dotted line is a least squares fit to the 1990 data and the solid line represents a fit to 1991 observations. At warmer temperatures the two fits differ by approximately by 1°–2°C, and they converge at the colder cloud top temperatures. While this is in agreement with the hypothesis of *Minnis et al.*
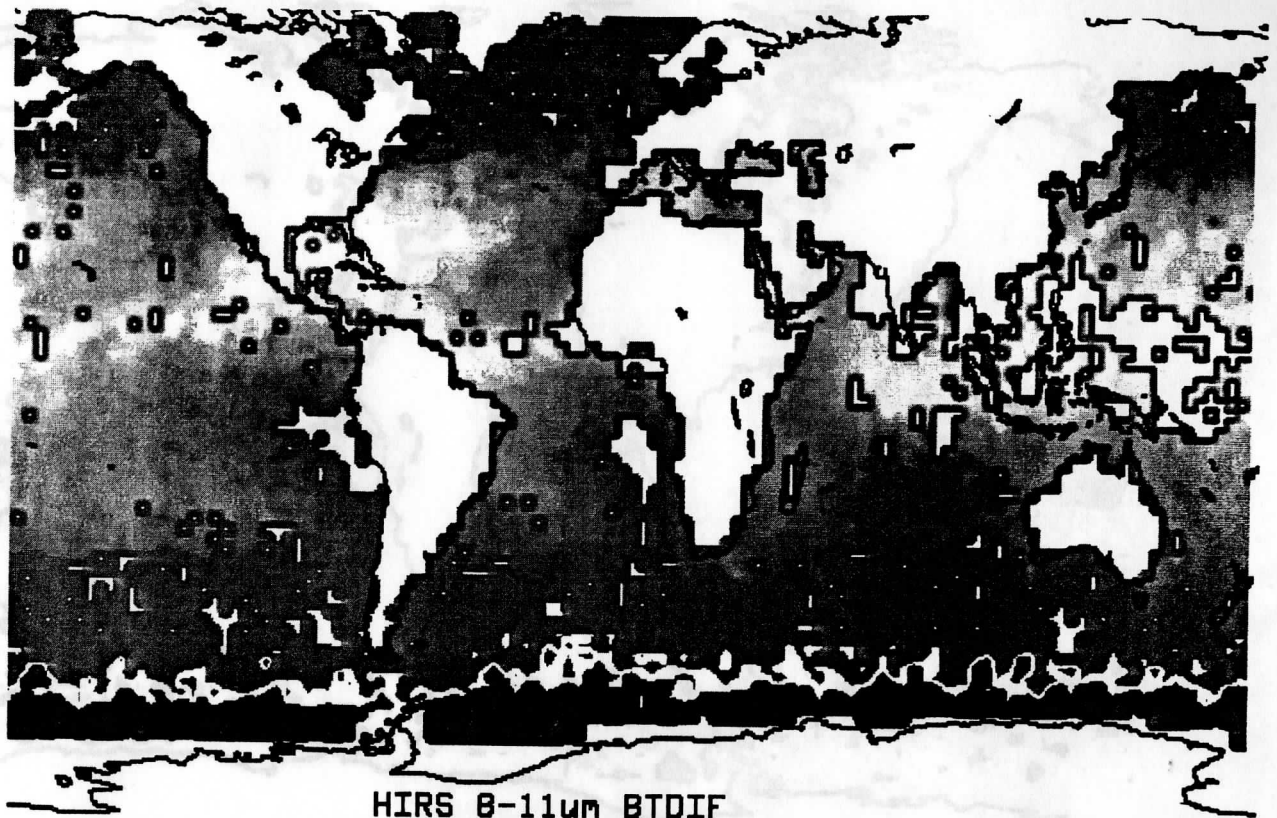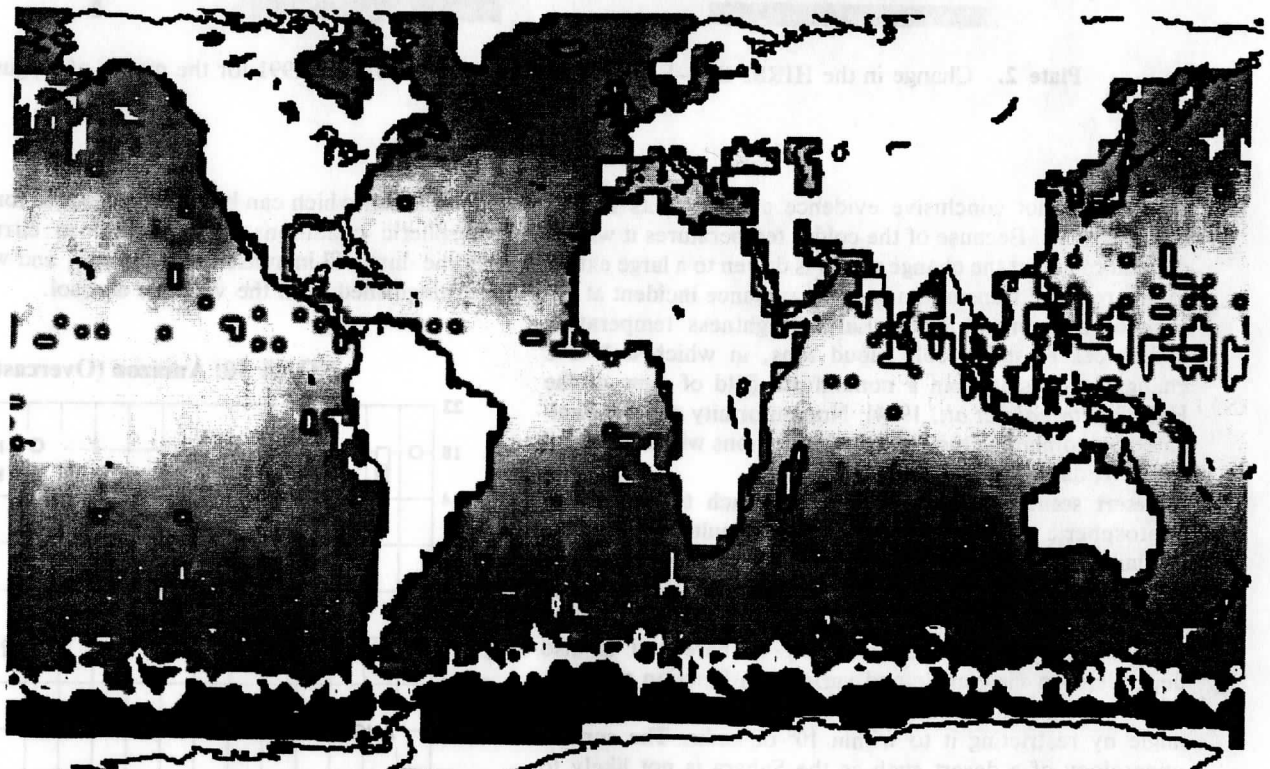
Plate 1. A composite analysis of the HIRS2 BT_8-BT_{11} for August 1990 and 1991. The legend is given at the bottom of each figure.

HIRS 8-11um CHANGE
AUG. 1990 TO AUG. 1991

+5   +2.5   +1   -1   -2.5   -5 deg C
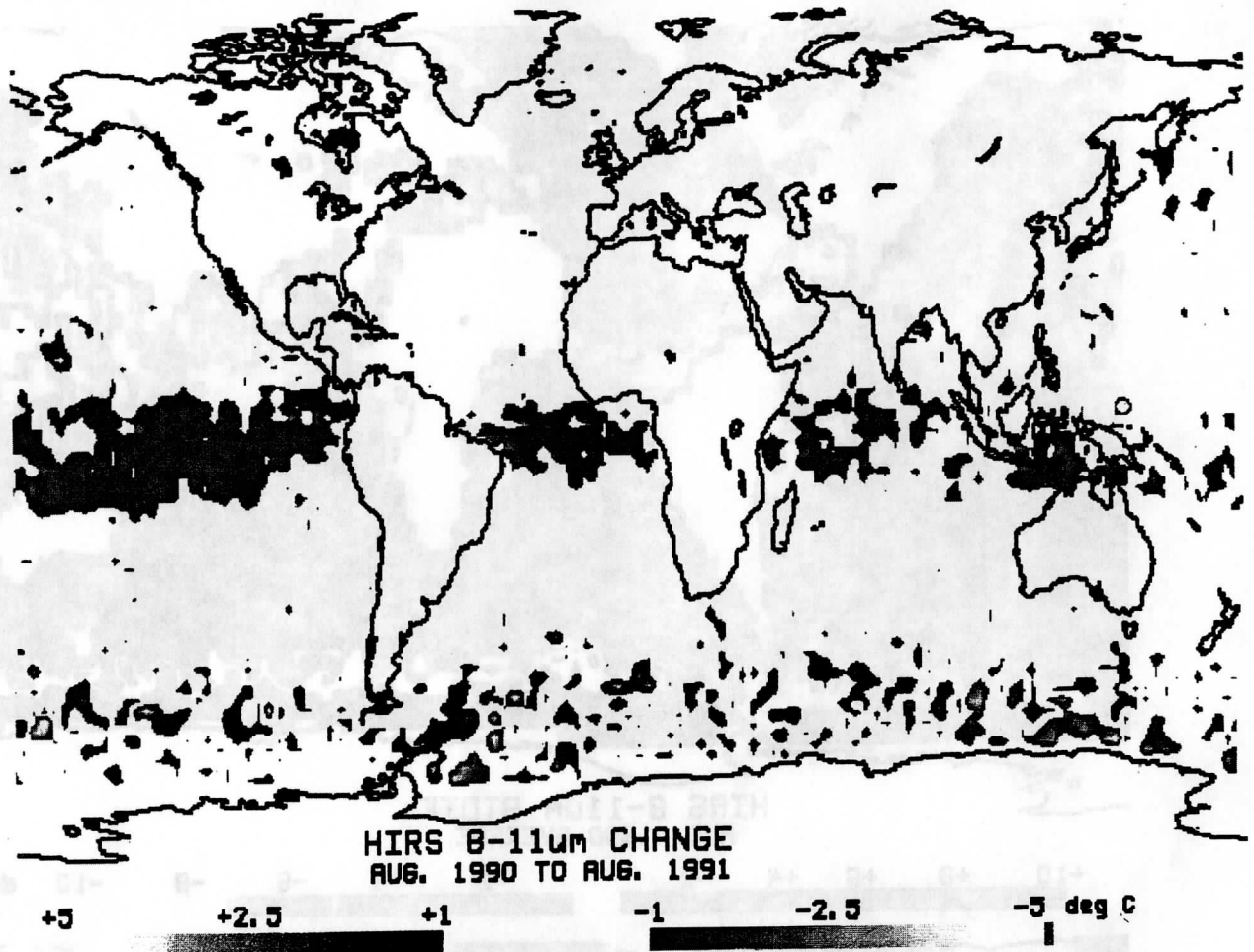
Plate 2. Change in the HIRS2 BT_8–BT_{11} between the years 1990 and 1991 for the month of August.

[1992], it is not conclusive evidence and warrants further investigations. Because of the colder temperatures it will be difficult to detect the change which is driven to a large extent by the reduced transmittance of the radiance incident at the base of the aerosol layer. Large brightness temperature differences exist for cold cloud tops, in which a 1°–2°C change can result from a nonuniform field of view of the HIRS2 [*Strabala et al.*, 1994]. Nonuniformity can be eliminated by combining the HIRS2 observations with collocated AVHRR data.

Desert scenes. The BT_8–BT_{11} approach to monitoring stratospheric volcanic aerosol is more difficult over land due to daily temperature changes and spectral variations in surface emissivity. The emissivity of bare soil varies considerably between 8 and 12 μm depending on the surface mineralogy. The surface emissivity of bare soil is also dependent on view angle and varies as a function of wavelength. We can minimize the spectral dependence on view angle by restricting it to within 10° of nadir. The surface mineralogy of a desert such as the Sahara is not likely to change radically on the timescale of one year. An increase in total precipitable water from 1990 to 1991 will result in a decrease of BT_8–BT_{11} as will the Mount Pinatubo aerosol layer. Unlike the oceanic case, over the desert there is no direct coupling between surface temperature and water

vapor amount which can be used to account for the varying atmospheric conditions. An increase in cirrus cloud or airborne dust will increase the BT_8–BT_{11} and will therefore be distinguished from the volcanic aerosol.
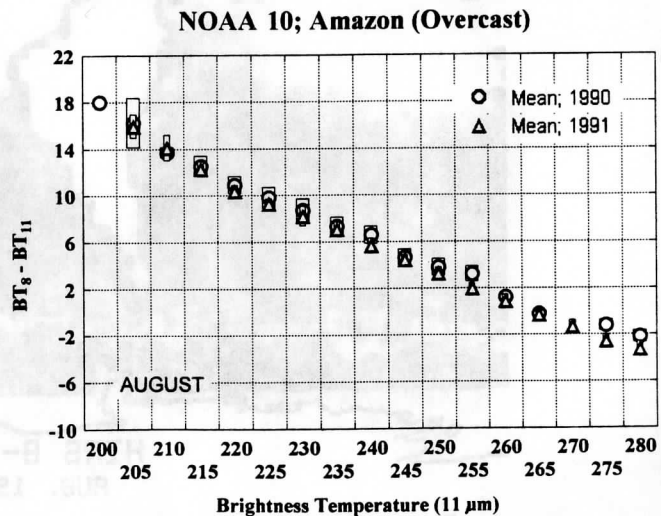

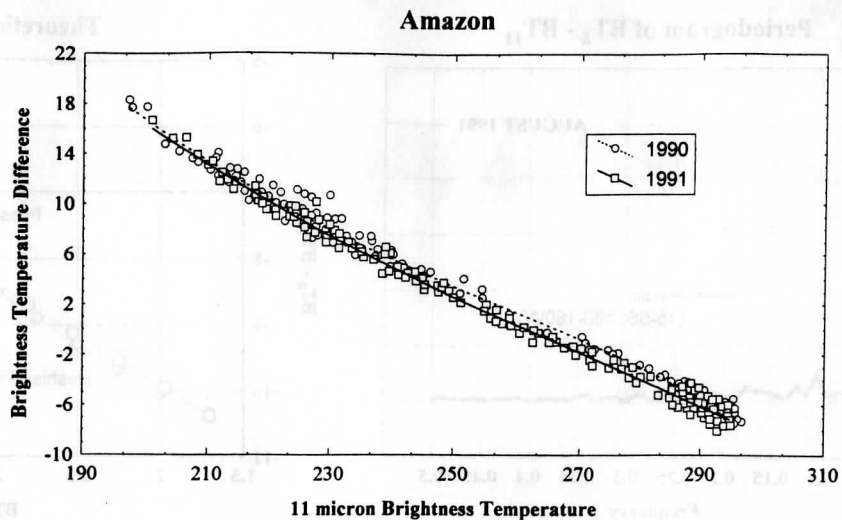**Figure 4.** Same as Figure 2 except for a region over the Amazon.

Amazon

Figure 5. Scatter diagram of the 11-μm brightness temperature versus BT_8–BT_{11} for August 1990 (circles) and 1991 (squares). The solid line represents the best fit polynomial curve to the 1991 data and the dotted line represents the fit to the 1990 data.

Figure 6 is a box analysis of the BT_8–BT_{11} versus BT_{11} for the Sahara Desert region for view angles of 0°–10°. The 1991 means (triangles) are consistently lower by approximately 1°C, than the 1990 values (circles). This is in agreement with expectations for the Mount Pinatubo aerosol as observed over the ocean region. While not so conclusive as the oceanic case, the desert 1991 means lie just within the standard deviation of the 1990 observations, they suggest a potential for detecting the aerosol over the desert and warrant further study.

3.2. Time Series Analysis

The spatial distribution of the aerosol depends on the transport mechanisms and the microphysical processes such as coagulation, sedimentation, and chemical reactions. Time series analysis of the satellite observations can provide insight to the transport processes. For example, *Stowe et al.* [1992] analyzed the east-west progression of the Mount Pinatubo aerosol by plotting the daily values of aerosol optical thickness (AOT) averaged over the 0°–10°S zonal band as a function of longitude from 100°E to 80°W. They estimated that for the first two months the aerosol layer circled the Earth with a period of approximately 16–18 days. Analysis of more zonal bands over the tropical regions for June to November indicated the aerosol was circulating the globe with a period of approximately 18–22 days.

The brightness temperature differences of 1°–1.5°C suggests the capability of tracking the aerosol using the infrared signal. In this section we use the HIRS2 observations to further explore the periodicity of the stratospheric aerosol. We analyze clear-sky daily observations of BT_8–BT_{11} averaged over Southeast Pacific (15°–5°S and 160°–180°W). We consider only observations ±10° view angles and average all observations within the geographic region made in a day. Days with missing values are linearly interpolated from nearby values. To search for periodicity, we perform a harmonic analysis of the BT_8–BT_{11} data and smooth the periodogram using 3-point Daniel weights. Figure 7 displays the smoothed periodogram. The broad peak at a frequency of approximately 0.05 corresponds to periods of 18 to 26

days. This Fourier analysis of the brightness temperature difference time series results in periodicities that are similar to that inferred by *Stowe et al.* [1992], demonstrating the potential utility of the thermal observations for monitoring the position of the aerosol layer.

3.3. Trispectral Analysis

The bulk transmittance of many aerosols display a strong spectral variation in the 8- to 13-μm region. For this reason, techniques have successfully employed temperature differences between the 11- and the 12-μm channels of the AVHRR to detect aerosols [e.g., *Prata*, 1989; *Barton et al.*, 1992]. More recently, *Baran et al.* [1993] proposed using observations at 8.3 and 12.5 μm to detect stratospheric aerosols. The brightness temperature differences among 8-, 11-, and 12-μm channels has been shown to be useful in detecting cirrus clouds [*Ackerman et al.*, 1990; *Strabala et*

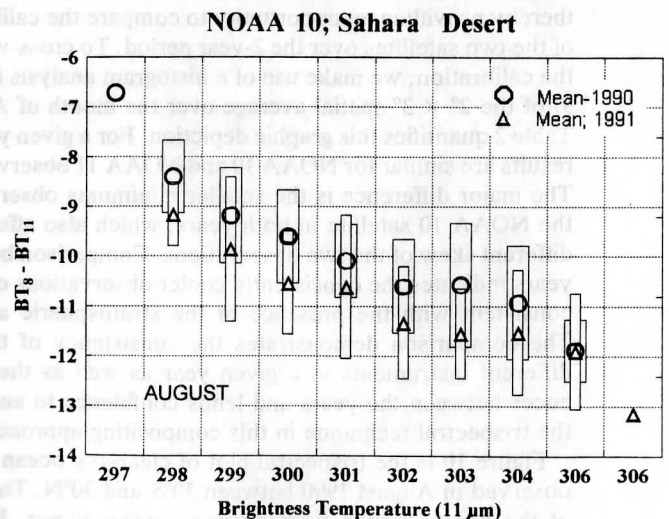**NOAA 10; Sahara Desert**

Figure 6. Same as Figure 2 except for a region over the Sahara Desert.

Periodogram of $BT_8 - BT_{11}$
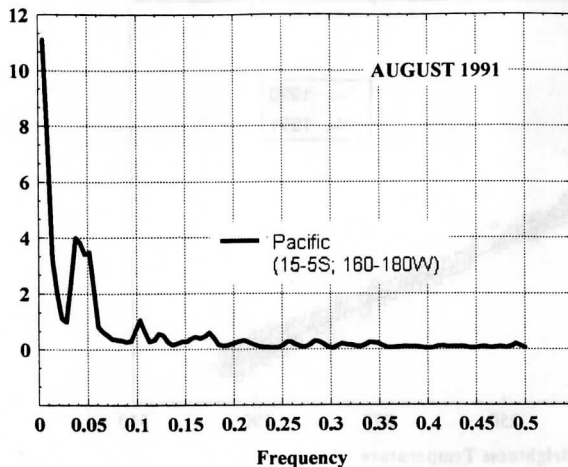
Figure 7. Periodogram of BT_8-BT_{11} for the period June to December 1991.
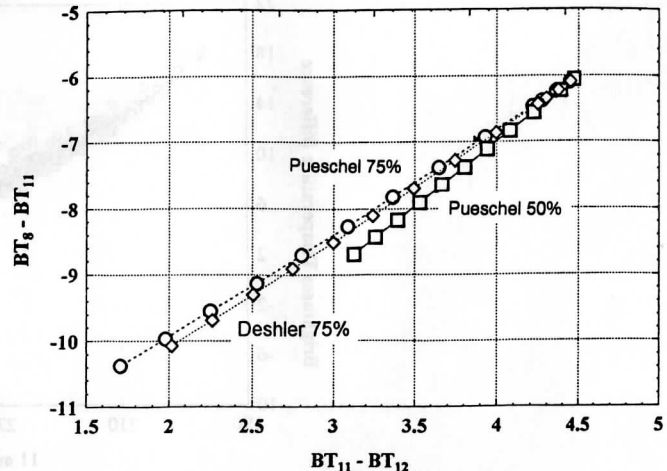
Theoretical Simulation

Figure 8. Theoretical simulation of brightness temperature difference between 11.1 and 12.5 μm ($BT_{11}-BT_{12}$) versus the difference between 8.3 and 11.1 μm (BT_8-BT_{11}). The three different curves represent the three distributions listed in Table 1.

al., 1994]. In this section we apply our trispectral technique for remote sensing of volcanic aerosols.

Figure 8 is a theoretical simulation of the effect of the Mount Pinatubo aerosol on the brightness temperature difference among the three IR channels, assuming the physical characteristics present in Table 1. As the optical thickness of the aerosol increases, BT_8-BT_{11} and $BT_{11}-BT_{12}$ decrease. While the change is in the same direction as an increase in water vapor for BT_8-BT_{11}, the change is opposite to that of increased water vapor for the $BT_{11}-BT_{12}$ parameter. Thus the three-channel technique may aid in separating the effects of water vapor from those of the aerosol as well as clouds [*Strabala et al.*, 1994].

As no present single satellite instrument makes observations at all three wavelengths, we composited observations from the HIRS2 instruments flown on NOAA 10 and NOAA 11 satellites. The NOAA 11 platform provides observations at 11 and 12 μm, while the HIRS2 on the NOAA 10 provides observations at 8 and 11 μm. Clear-sky observations with view angles less than 10° are averaged over 2° latitude by 3° longitude regions. Both instruments have an 11-μm channel, thereby providing an opportunity to compare the calibration of the two satellites over the 2-year period. To cross-validate the calibration, we make use of a histogram analysis (Figure 9) of the 2° × 3° spatial average over the month of August. Table 2 quantifies this graphic depiction. For a given year the results are similar for NOAA 10 and NOAA 11 observations. The major difference is the smaller minimums observed by the NOAA 10 satellite in both years, which also affects the different skew of the two observations. Comparison between years indicates the consistently cooler observations of 1991, consistent with the presence of the stratospheric aerosol. The comparison demonstrates the consistency of the two different instruments in a given year as well as the differences between the years and lends confidence to analyzing the trispectral technique in this compositing approach.

Figure 10 is the trispectral plot of clear-sky ocean scenes observed in August 1990 between 30°S and 30°N. The slope of the points results from changing water vapor. Positive values of $BT_{11}-BT_{12}$ result from stronger absorption at 12.5 μm, and the BT_8-BT_{11} negative values result from stronger

absorption at 8.3 μm. The ellipse oriented along a linear regression between the variables denotes the 95% probability that a point will fall within the enclosed region. This circle is replicated in Figure 11 which depicts the post-Pinatubo trispectral observations for the month August 1991. Many points lie outside the 95% confidence ellipse generated with the 1990 observations. The departure is consistent with the effects of the aerosols. Partial field of view cloud contamination would drive the differences in the opposite direction [*Strabala et al.*, 1994].

The effect of the Mount Pinatubo aerosol on the $BT_{11}-BT_{12}$ are also demonstrated in a box diagram (Figure 12). The difference between the 1990 and 1991 means ranges from 0.5° to 0.8°C. Referring to the theoretical simulations (Figure 8), this implies a BT_8-BT_{11} of 1°-1.5°C, which is in agreement with the present infrared observations and the optical depth estimates of *Stowe et al.* [1992] (see Figure 1). Thus the model calculations and satellite visible and infrared observations are consistent in suggesting, for this region and time, infrared optical depths at 8.3, 11.1, and 12.5 μm of 0.03-0.06, 0.014-0.02, and 1.2×10^{-3}-4×10^{-3}, respectively.

4. Summary

Methods of monitoring stratospheric aerosol using brightness temperature differences between 8- and 11-μm channels, and 8-, 11-, and 12-μm channels are presented. The methods are illustrated with theoretical calculations. More theoretical work is required to refine the techniques and understand their capabilities and limitations. Observations made by the HIRS2 on board the NOAA 10, NOAA 11, and NOAA 12 satellites are used to demonstrate the technique and to monitor the presence of the Mount Pinatubo aerosol layer. Differences between 1990 and 1991 observations of BT_{8-11} over clear-sky oceanic regions clearly indicate the presence of the stratospheric aerosol layer. The suitability of the method to regions of high reflectance is also demonstrated.

August (30N-30S)

2 X 3 Latitude/Longitude Grid Averages
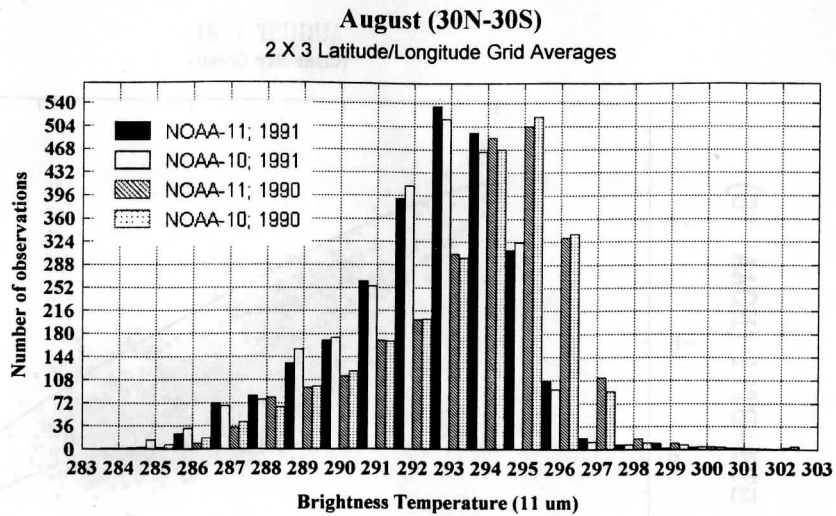
Figure 9. Histogram of the 11-μm brightness temperature for the NOAA 10 and NOAA 11 satellites for August 1990 and 1991.

**Table 2.** Statistical Analysis of 11-μm Brightness Temperatures Observed by NOAA 10 and 11 Satellites in August 1990 and 1991

Satellite, Year	Mean	Median	Min	Max	Lower Quartile	Upper Quartile	Standard Deviation	Skew
NOAA 11, 1991	292.98	293.35	284.26	302.03	291.68	294.56	2.34	−.47
NOAA 10, 1991	292.85	293.23	280.28	301.57	291.51	294.56	2.38	−.64
NOAA 11, 1990	293.99	294.48	284.82	303.31	292.62	295.75	2.49	−.66
NOAA 10, 1990	293.87	294.42	281.31	302.80	292.47	295.66	2.57	−.85

AUGUST 1990
(Clear-Sky Ocean)
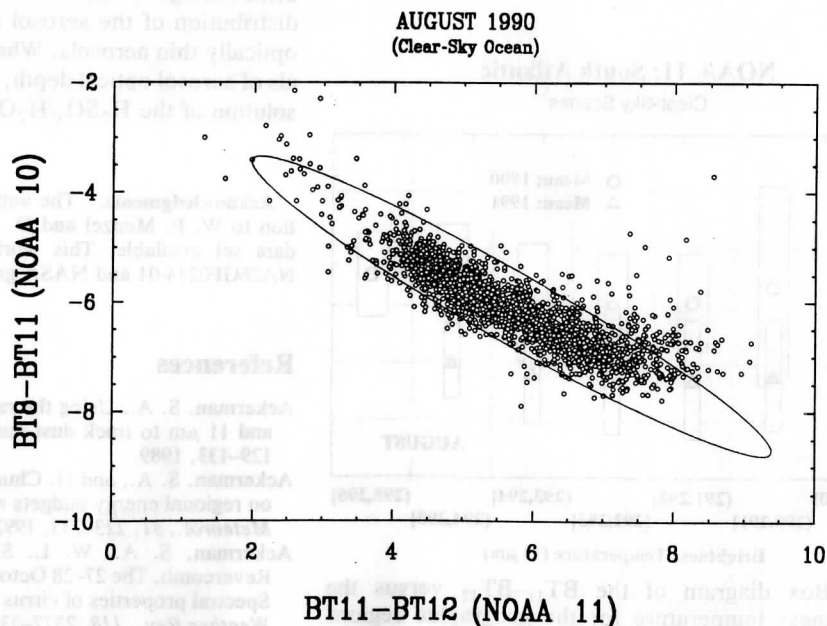
Figure 10. Scatter diagram for the clear-sky August 1990 observations of NOAA 11 brightness temperature difference between 11 and 12 μm versus the NOAA 10 brightness temperature difference between 8 and 11 μm. The ellipse represents the 95% confidence limit that points lie within the region.

AUGUST 1991
(Clear-Sky Ocean)
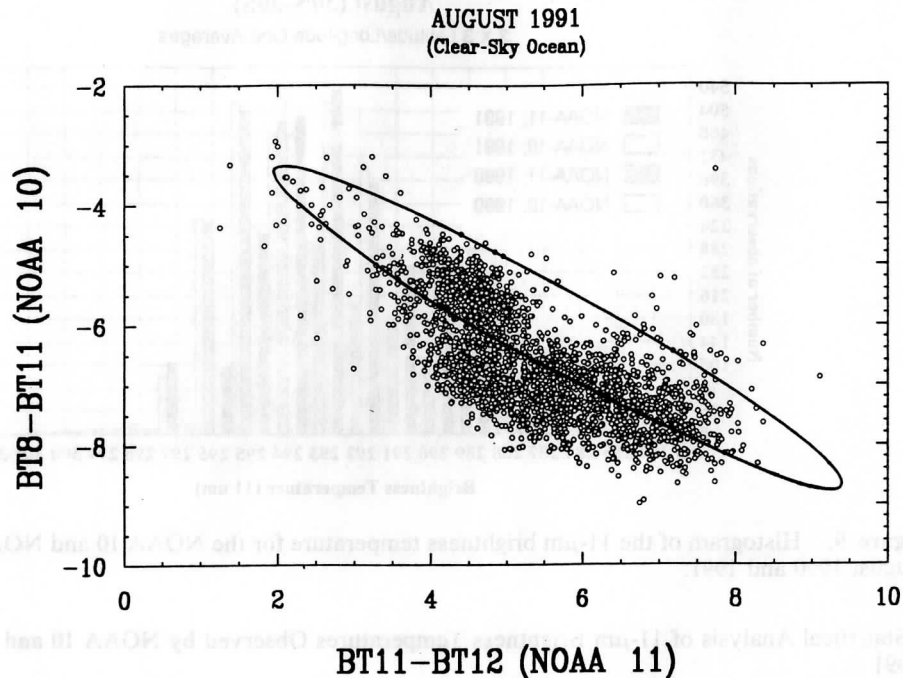
Figure 11. Scatter diagram for the clear-sky August 1991 observations of NOAA 11 brightness temperature difference between 11 and 12 μm versus the NOAA 10 brightness temperature difference between 8 and 11 μm. The ellipse represents the 1990 95% confidence limit of Figure 10.

A time series analysis of the BT_8-BT_{11} for a 7-month period for an oceanic region indicates a periodicity of 18–26 days, consistent with other global observations of the spreading of the Mount Pinatubo aerosol. When compared to a similar analysis for August 1990, a spatial analysis over the month of August 1991 clearly indicates the zonal presence of the aerosol.

Observations of HIRS2 on the NOAA 11 and NOAA 10 satellites were composited to demonstrate the potential of the trispectral technique. Over ocean regions the analysis suggests the potential for future satellite instruments to separate cirrus clouds from stratospheric H_2SO_4 aerosols. Application over land requires more work.

Advantages of the method are that it can be applied during both night and day and has a better time sampling than solar occultation methods. It also has potential to be applied over high-albedo surfaces such as deserts and deep convective clouds, a limitation of visible reflectance techniques. A disadvantage is that it has no information on the vertical distribution of the aerosol and may be difficult to apply in optically thin aerosols. When combined with visible retrievals of aerosol optical depth, it may be feasible to estimate the solution of the H_2SO_4/H_2O droplets.

NOAA 11; South Atlantic
Clear-Sky Scenes
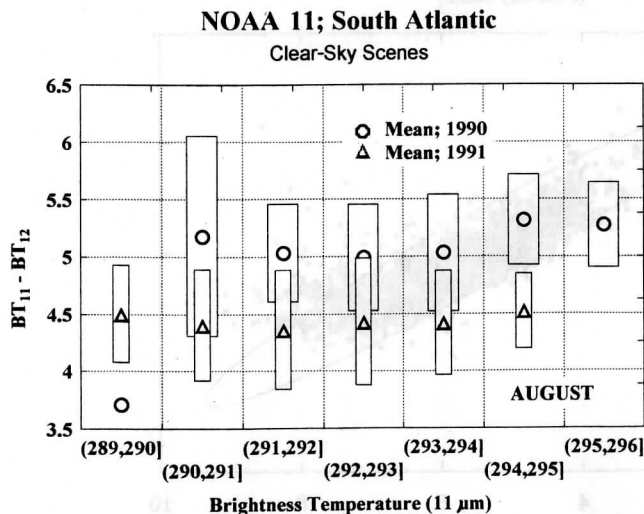
Figure 12. Box diagram of the $BT_{11}-BT_{12}$ versus the 11-μm brightness temperature for the geographic regions 0°–20°S and 0°–30°W for the month of August. The symbols represent the mean for that year (circles, 1990; triangles, 1991) and the rectangles the standard deviation (wide box for 1990, narrow box for 1991).

References

Ackerman, S. A., Using the radiative temperature difference at 3.7 and 11 μm to track dust outbreaks, *Remote Sens. Environ.*, *27*, 129–133, 1989.

Ackerman, S. A., and H. Chung, Radiative effects of airborne dust on regional energy budgets at the top of the atmosphere, *J. Appl. Meteorol.*, *31*, 223–233, 1992.

Ackerman, S. A., W. L. Smith, J. D. Spinhirne, and H. E. Revercomb, The 27–28 October 1986 FIRE IFO cirrus case study: Spectral properties of cirrus clouds in the 8–12 μm window, *Mon. Weather Rev.*, *118*, 2377–2388, 1990.

Baran, A. J., J. S. Foot, and P. C. Dibben, Satellite detection of volcanic sulphuric acid aerosol, *Geophys. Res. Lett.*, *20*, 1799–1801, 1993.

Barton, I. J., A. J. Prata, I. G. Watterson, and S. A. Young,

Identification of the Mount Hudson volcanic cloud over SE Australia, *Geophys. Res. Lett.*, *19*, 1211–1214, 1992.

Bluth, G. J. S., S. D. Doiron, C. C. Schnetzler, A. J. Krueger, and L. S. Walter, Global tracking of the SO_2 clouds from the June 1991 Mount Pinatubo eruptions, *Geophys. Res. Lett.*, *19*, 151–154, 1992.

Chandra, S., Changes in stratospheric ozone and temperature due to the eruptions of Mt. Pinatubo, *Geophys. Res. Lett.*, *20*, 33–36, 1993.

Deshler, T., D. J. Hoffman, B. J. Johnson, and W. R. Rozier, Balloon-borne measurements of the Pinatubo aerosol size-distribution and volatility at Laramie, Wyoming, during the summer of 1991, *Geophys. Res. Lett.*, *19*, 199–201, 1992.

Dutton, E. G., and J. R. Christy, Solar radiative forcing at selected locations and evidence for global lower tropospheric cooling following the eruptions of El Chichon and Pinatubo, *Geophys. Res. Lett.*, *19*, 2313–2316, 1992.

Kondratyev, K. Ya., Volcanoes and climate, *WCP-54, WMO/TD 166*, 103 pp., World Meteorol. Organ., Geneva, 1988.

Lamb, H. H., Volcanic dust in the atmosphere, with a chronology and assessment of its meteorological significance, *Philos. Trans. R. Soc. London A*, *266*, 424–533, 1970.

McClatchey, R. A., R. W. Fenn, J. E. Selby, F. E. Volz, and J. S. Garing, *Optical Properties of the Atmosphere*, 3rd ed., Air Force Cambridge Res. Labs., Hanscom Air Force Base, Mass., 1972.

Minnis, P., E. F. Harrison, L. L. Stowe, G. G. Gibson, F. M. Denn, D. R. Doelling, and W. L. Smith Jr., Radiative climate forcing by the Mount Pinatubo eruption, *Science*, *259*, 1411–1415, 1993.

Palmer, K. F., and D. Williams, Optical constants of sulfuric acid, Application to the clouds of Venus? *Appl. Opt.*, *14*, 208–219, 1975.

Prata, A. J., Observations of volcanic ash clouds in the 10–12 μm window using AVHRR/2 data, *Int. J. Remote Sens.*, *10*, 751–761, 1989.

Pueschel, R. F., S. A. Kinne, P. B. Russell, K. G. Snetsinger, and J. M. Livingston, Effects of the 1991 Pinatubo volcanic eruption on the physical, optical and radiative properties of stratospheric aerosols, in *Proceedings of the IRS '92*, edited by S. Keevallik, A. Deepak, Hampton, Va., 1993.

Rao, C. R. N., L. L. Stowe, and E. P. McClain, Remote sensing of aerosols over the oceans using AVHRR data: Theory, practice and application, *Int. J. Remote Sens.*, *10*, 743–749, 1989.

Steele, H. M., and P. Hamill, Effect of temperature and humidity on the growth and optical properties of sulphuric acid-water droplets in the stratosphere, *J. Aerosol Sci.*, *12*, 517–528, 1983.

Stephens, G. L., On the relations between water vapor over the oceans and sea surface temperature, *J. Clim.*, *3*, 634–645, 1990.

Stowe, L. L., R. M. Carey, and P. P. Pellegrino, Monitoring the Mt. Pinatubo aerosol layer with NOAA/11 AVHRR data, *Geophys. Res. Lett.*, *19*, 159–162, 1992.

Strabala, K. I., S. A. Ackerman, and W. P. Menzel, Cloud properties inferred from 8–12 μm data, *J. Appl. Meteorol.*, 212–229, 1994.

Toon, O. B., Volcanoes and climate, in Atmospheric Effects and Potential Climatic Impact of the 1980 Eruptions of Mount St. Helens, edited by A. Deepak, NASA *Conf. Publ. 2240*, pp. 15–36, 1982.

Wylie, D. P., and W. P. Menzel, Two years of cloud cover statistics using VAS, *J. Clim.*, *2*, 380–392, 1989.

S. A. Ackerman and K. I. Strabala, CIMSS Space Science Center, University of Wisconsin, 1225 W. Dayton, Madison, WI 53706.

Climate Parameters from Satellite Spectral Measurements Part I: Collocated AVHRR and HIRS/2 Observations of Spectral Greenhouse Parameter

Richard A. Frey, S. A. Ackerman
Cooperative Institute for Meteorological Satellite Studies
University of Wisconsin-Madison
and
Brian J. Soden
Atmospheric and Oceanic Sciences Program
Princeton University

1

ABSTRACT

An automated method of monitoring various climate parameters using collocated AVHRR (Advanced Very High Resolution Radiometer) and HIRS/2 (High-resolution InfraRed Sounder - 2) observations has been developed. The method, referred to as CHAPS (Collocated HIRS/2 and AVHRR ProductS) was implemented during the months of July 1993 and January and July 1994. This paper presents the oceanic cloud screening method and analysis of the spectral greenhouse parameter (g_λ) for July 1993 and January 1994. In addition, the CHAPS derived clear-sky parameters are compared to the NESDIS historical data set. There is agreement between NESDIS and CHAPS for the $g_{6.7}$ and $g_{7.3}$. The NESDIS 8.2 μm data appears to be cloud contaminated. Through comparison with CHAPS, it is suggested that the mode, rather than the mean, provides the better estimate of the central tendency of the NESDIS clear-sky 8.2 μm radiance distribution, particularly for regions with extensive low level cloud cover.

It is shown that the spectral greenhouse parameter at wavelengths sensitive to middle and upper atmospheric water vapor content is dependent on SST via its connection to large scale atmospheric circulation patterns. It is also shown that the variability of the spectral greenhouse parameter is strongly a function of latitude at these wavelengths, as well as in spectral regions sensitive to lower level water vapor. Standard deviations are largest in the tropics and generally decrease poleward. In contrast, variability in

2

the spectral regions sensitive to upper tropospheric temperature, peaks in the middle latitudes and has its minimum in tropical latitudes.

Variability in the relationship between g_λ and SST shows only a weak dependence on season for channels sensitive to water vapor content. A strong seasonal dependence is found in the $g_{14.2}$ for the middle latitude regions associated with changes in the temperature structure of the upper troposphere.

The relationship between the spectral greenhouse parameter and the broadband greenhouse parameter is presented and discussed. It is found that the range in broadband g for warm tropical SSTs is driven by spectral changes at wavelengths sensitive to upper tropospheric water vapor. For cooler SSTs associated with the middle latitudes, the range in g is a function of the spectral greenhouse parameter sensitive to the temperature structure of the upper troposphere.

1 Introduction

The satellite platform provides a means for global monitoring of various earth-system parameters. Long-term satellite data sets spanning time periods of up to 20 years are now becoming available for use in the investigation of climate trends and variability. Although such time intervals are usually considered too short for climate studies, any effort to systematically analyze a time series of global satellite data of even that length would be extraordinarily costly. In order to avoid the expense of retrieving data from archives, the authors have developed a method whereby observations from two instruments on the same space platform are combined in a near real-time environment. Various climate parameters are computed and analyzed in the same time frame. Similar algorithms could conceivably be expanded to include more instruments and be operated over long time periods in order to automatically monitor important atmospheric variables such as cloud type and amount, cloud radiative forcing and the "greenhouse effect" of the atmosphere.

This paper is the first in a series of investigations of various climate parameters using global satellite spectral observations. These global measurements are used to study inter-annual and inter-seasonal variations. The global data also provide validation for climate models and will lead to interesting insights on atmospheric processes relevant to climate change studies.

4

Part one focuses on the methods of data collection and clear-sky determination, along with analysis of the spectral greenhouse parameter. Variations in clear-sky observations from various spectral bands across the infrared spectrum are investigated, as well as their relation to the broadband observations.

The algorithm designed to operate in near-real time for the purpose of monitoring climate parameters and which makes use of collocated radiance measurements from the Advanced Very High Resolution Radiometer (AVHRR) and the High Resolution Infrared Sounder/2 (HIRS/2) is referred to as CHAPS - Collocated HIRS/2 and AVHRR ProductS. Observations from instruments aboard the NOAA-12 space platform were used in conjunction with forecast model output from the National Meteorological Center (NMC) to produce global distributions of cloud altitude and amount, the spectral greenhouse effect of the atmosphere, and spectral cloud radiative forcing. This study utilizes CHAPS data collected during the months of July 1993 and January 1994 for the purpose of studying the spectral properties of the clear-sky atmposphere.

The feasibility of collocating measurements from two instruments and analyzing the combined data in near real-time is also demonstrated. The technique discussed below can therefore be adapted into an operational algorithm but could be applied to historical data sets as well. In this paper, the emphasis on collocating AVHRR pixels within the HIRS/2 footprints is

5

to ensure cloud-free HIRS/2 scenes. A complete discussion of the spectral measurements and the CHAPS cloud screening process for ocean surfaces is found in Section 2. Comparison of the CHAPS derived clear-sky parameters with those derived from the historical National Environmental Satellite, Data, and Information Service (NESDIS) operational radiances is given in Section 3. Analysis of the spectral greenhouse parameter is undertaken in Section 4 and the results of the study are summarized in section 5.

2   Satellite Observations

Adequate discrimination between clear and cloudy scenes from space is crucial for an understanding of global radiation balance, cloud cover, surface property studies, and retrieval of atmospheric temperature and moisture profiles. The description and understanding of the Earth's clear regions is important for its own sake, but also as a reference for changes in radiative forcings caused by differing cloud types and amounts. By combining the spectral resolution of an atmospheric sounder (HIRS/2) with the spatial resolution of an imager (AVHRR) we hope to more accurately describe the radiative properties of clear-sky regions. Hayden and Taylor (1985) and Levanant (1989) used collocated AVHRR and HIRS/2 observations to improve clear-sky HIRS/2 scenes and thus improve the atmospheric profiling of the TOVS package. Ackerman et al (1992) used collocated AVHRR, HIRS/2 and ERBE observations to study clear and cloudy sky radiative

6

properties. Collocated AVHRR and HIRS/2 data have also been used to study cloud properties (e.g., Baum et al, 1992; Baum et al, 1994). Derrien et al (1993) make use of the AVHRR to assess the cloud conditions within the HIRS/2 footprint and have developed an automatic regional cloud detection technique for the NOAA-11 using AVHRR 1 km data. In this paper we present an automated global cloud detection technique using the AVHRR and HIRS/2 data in tandem.

Tables 1 and 2 list channel information for the HIRS/2 and AVHRR instruments aboard NOAA-12. The spatial resolution of the HIRS/2 is nominally 17 km at nadir, while that of the AVHRR is 1 km. The present study utilized AVHRR Global Area Coverage (GAC) data, where every third scanline was recorded and four of each five-pixel group along these scanlines were averaged, resulting in a nominal resolution of 4 km. The NOAA-12 space platform is in near-terminator sun-synchronous orbit with an inclination of approximately 110 degrees and height of 850 km. Such an orbit provides near-global coverage in 24 hours, with observations near 07:30 and 19:30 local time for most latitudes. This allows monitoring of day to day changes in clear-sky radiative properties due to variations in atmospheric moisture and temperature. This is particularly important in areas of the world which are otherwise very data-sparse. Using the methodology described below, it is possible to build an archive of high quality clear-sky parameters over the world's oceans. Such a data set now exists for the months of July 1993 and January and July 1994.

2.1 Data Acquisition and Processing

The radiance data were acquired in near-real time from the Man-computer Interactive Data Access System (McIDAS) at the University of Wisconsin-Madison (Suomi et al 1983). Calibrated and navigated AVHRR and HIRS/2 measurements (Kidwell, 1991) are stored on an IBM 4381 mainframe several hours after the completion of each orbit by the spacecraft. These data sets remain on the computer for approximately 24 hours, until being overwritten by more recent observations. Global fields of vertical temperature and moisture profiles were obtained from the NMC in Camp Springs, MD. These "final analysis" fields are output for 0 and 12 hours UTC and are available approximately 10 hours later. Weekly, global Reynolds' blended sea surface temperatures (SSTs) were also received from the NMC.

Because of the tremendous volume of data, particularly from the AVHRR, processing had to be completed in a timely fashion to reduce the amount and cost of storage space. This was accomplished with the use of an IBM RISC 6000 computer. When new orbital data appeared on the mainframe, it was transferred to the RISC 6000 by use of the standard File Transfer Protocol (ftp) software. A pre-processing program was run periodically to ascertain which ancillary datasets would be needed (e.g. NMC profiles which would not be available for several hours), to match up the HIRS/2 and AVHRR orbital data sets, and to generate any other parameters necessary for processing. The input NMC temperature and moisture fields were

8

linearly time-interpolated, when necessary, to the nearest hour of the orbital start times. Such a scheme is adequate for processing over the ocean surface where diurnal temperature variations are very small. This software acted as a funnel, gathering data from several machines, usually at several different times, providing the main processing stream with all of the information needed to process one complete orbit.

The central and most CPU-intensive task of the data processor is the collocation of the AVHRR GAC pixels within the larger HIRS/2 footprints. The method described by Aoki (1980) was chosen, but where GAC data is used in place of the 1 km Local Area Coverage (LAC) type. This method has been used with good success by the present authors (Ackerman et. al., 1992). Although the attempt was made to process as much data as possible, in order to minimize problems associated with limb measurements, sun glint, and angular effects on visible measurements, fields of view (FOVs) beyond 30 degrees of nadir were eliminated from the collocation. Also, poleward of 70 degrees latitude only one of four HIRS/2 FOVs was collocated with AVHRR pixels, due to the oversampling by polar orbiters in these regions. By restricting scan width, the amount of time needed to achieve truly global coverage is lengthened to two days, but any given geographical area is observed at least once for four consecutive days near the equator and more often nearer the poles. Even with the above restrictions, approximately 20,000 collocated HIRS/AVHRR FOVs were produced per

orbit with about 30 AVHRR GAC observations for each HIRS/2. The collocated measurements (as well as all derived products) were mapped onto a 2.5° latitude equal-surface-area grid according to the International Satellite Cloud Climatology Project (ISCCP) binning scheme (Rossow and Schiffer, 1991).

A check on the quality of the collocations is readily accomplished by comparison of the 11 μm "window" channel measurements of each instrument. Given that the atmosphere is nearly transparent at this wavelength, both instruments sense a wide variety of scene temperatures as the spacecraft progresses in its orbit. AVHRR pixel radiances were averaged over the corresponding HIRS/2 FOVs and converted to equivalent temperatures, then compared to those of the single HIRS/2 measurements. AVHRR data were also corrected for the known non-linearity of calibration in the three infrared channels (Brown, 1991). Correlations over an orbit were generally greater than 0.99. Because it is convenient in terms of computer processing efficiency, three other algorithms are executed during the collocation step. First is the CO_2-slicing method of cloud altitude determination (Smith et al, 1974; Smith and Platt, 1978; Menzel et al, 1983) using five of the HIRS/2 infrared channels. This information is used as part of a quality control system for clear-sky determination later in the processing stream. Secondly, histograms of AVHRR pixel values for each of its five channels are produced for each ISCCP region viewed. The class widths are 0.5K

10

for infrared channels and 1% for the visible. Only those pixels found to be located within HIRS/2 FOVs are incorporated into the histograms, which saves considerable amounts of computer time. Figure 1a shows a typical subtropical regional histogram of AVHRR 11 μm brightness temperatures. Figure 1b is similiar but incorporates only the collocated pixels which fell inside HIRS/2 footprints. It is clear that the second histogram captures the important thermal characteristics of the region. Third, an estimate of total precipitable water at the location of each HIRS/2 FOV is computed based on spatially and temporally interpolated NMC temperature and moisture profiles.

2.2 Clear-Sky Determination

Using HIRS/2 spectral measurements and AVHRR GAC collocated pixel data, an attempt is made to determine which HIRS/2 FOV locations (if any) are clear within each ISCCP region viewed. Information from any such FOVs are used to infer the regional mean clear-sky radiative characteristics.

An important part of this process is the generation of regional 11 μm clear-sky brightness temperature threshholds. The first step is to compute a first guess clear-sky brightness temperature threshhold at each HIRS/2 FOV location in the region.

Based on total precipitable water (TPW) estimates noted above, HIRS/2 scan angles (SCNA), and collocated AVHRR radiance data from a wide variety of ocean scenes, the following regression equation was developed:

11

$$SFCDIF = A0 + (A1 * TPW/\cos(SCNA)) + (A2 * (TPW/\cos(SCNA))^2) \quad (1)$$

where SFCDIF is the difference between the Reynolds' blended SST and the mean collocated AVHRR brightness temperature at a given FOV location. The values of the coefficients are: $A0 = -0.8163$, $A1 = 0.5488$, and $A2 = 0.1132$.

The first guess threshhold (FGT) may then be written,

$$FGT = SST - SFCDIF - 4.0 \quad (2)$$

The extra four degrees subtracted from the SST is to account for the standard lapse rate from the surface to the minimum expected cloud base.

Making use of the computed variabilities of collocated AVHRR pixels and the FGT associated with each HIRS/2 FOV location in a region, individual GAC 11 μm measurements within each HIRS/2 FOV are sorted into *possibly clear* and *possibly cloudy* categories. During nighttime situations (solar zenith angles greater than or equal to 80 degrees), if the standard deviation of 11 μm collocated observations is less than or equal to 0.5K, then each 11 μm pixel value is compared with the FGT for that HIRS/2 FOV location. Measurements with brightness temperatures greater than or equal to the FGT are incorporated into a second, (possibly) clear-sky histogram (CSH). During daytime situations (solar zenith angle less than

12

80 degrees), the further requirement is made that the AVHRR channel 2 reflectance be less than or equal to a threshold (e.g., 6.5 %.) This process is repeated for all HIRS/2 FOV locations in the ISCCP region. The final clear-sky 11 μm brightness temperature threshhold is defined as the temperature corresponding to the class of maximum frequency in the CSH minus the standard deviation computed from all of the *possibly clear* pixel values. It should be noted here that single-pixel measurements at 3.7 μm (channel 3) which could be useful in cloud screening, are not used in the algorithm due to the known low signal-to- noise characteristics of this channel.

The FGT and AVHRR FOV variability are used together to minimize cloud contamination. The variability check screens out collocated FOVs which may contain warm AVHRR measurements, but have a high probability of being cloud contaminated. It also flags FOVs containing thin cirrus clouds which are often characterized by warm brightness temperatures and low visible reflectance measurements. By use of Eq. 2, we attempt to define a brightness temperature which includes pixels from reasonably warm scenes, but excludes those colder, cloudy areas which may be very uniform. The daytime channel 2 reflectance test is an additional check for warm clouds such as stratus or fog which are bright in the visible wavelengths. When all of the AVHRR 11 μm measurements from pixels which passed the *possibly clear* tests are sorted into the CSH, observations from clear scenes will cluster into a sharp, narrow peak characteristic of the desired clear-sky

13

brightness temperature. Those from partly cloudy areas form a broader, ill-defined peak with fewer observations because of the higher temperature and moisture variability in those scenes. The standard deviation of the CSH AVHRR 11 μm values is subtracted from the peak temperature to allow for instrument noise in the measurements.

Figure 2 shows a histogram describing an ISCCP region centered on 18.75 S latitude and 109.85 W longitude on January 28, 1994. Figure 3 shows the associated CSH as well as the final clear-sky threshhold. A time series of clear-sky threshhold values, Reynolds' blended SSTs, and maximum collocated AVHRR 11 μm observed brightness temperatures is shown in Figure 4 for the ISCCP gridbox centered on 18.75S, 107.13W. Time runs through the month of January. Note that very little or no data was archived for a few days due to poor data quality or data ingest problems. Data may also be missing for a given day due to large scan angles. The two low points found on days 11 and 25 occur because no FOVs satisfying the *possibly clear-sky* criteria were found. The threshhold represented in the figure is the first guess. On these two days there are no high-confidence clear footprints and thus no clear-sky spectral greenhouse parameter is derived. Note that the maximum AVHRR values are also low on these days, while the SST remains nearly constant.

Final clear-sky determination for each HIRS/2 FOV location is accomplished by use of the regional clear-sky threshhold along with several other

14

criteria. If each of the criteria are met, the FOV in question is said to be clear. They are:

- If daytime, mean collocated AVHRR channel 2 refectance less than or equal to 6.5

- Mean collocated AVHRR 11 μm brightness temperature greater than or equal to the regional clear-sky threshhold

- Collocated AVHRR 3.7 μm standard deviation less than or equal to 0.5 degree K

- Collocated AVHRR 11 μm standard deviation less than or equal to 0.5 degree K

- HIRS/2 8 - 11 μm brightness temperature difference less than -3.5 degrees K

- Mean collocated AVHRR 11 - 12 μm brightness temperature difference greater than 0.5 degree K

- Computed cloud height from CO2-slicing algorithm greater than 500 mb

Tests 1, 2 and 4 have already been discussed, except that here we apply tests 1 and 2 to entire HIRS/AVHRR FOVs instead of one GAC pixel. Test 3 is included as an additional test for the presence of low, warm clouds, being particularly effective in daylight hours.

The last three tests take advantage of the multiple spectral channels of both instruments. Due to spectral differences in atmospheric absorption

15

of upwelling radiation due to cloud liquid water between 8 and 11 μm, versus that of ice, fully overcast FOVs containing ice cloud exhibit positive 8-11 μm differences, while those filled with water cloud show negative differences. The magnitude of the differences also depends on the total column water vapor amount. Therefore, given the same temperature and moisture conditions, clear-sky FOVs will yield greater negative differences than those contaminated with water cloud. At the same time, the presence of ice clouds (e.g. thin cirrus) also drives differences more positive. Strabala et al., (1994) use a threshhold value of 0.5° in defining clear-sky scenes observed with the MAS (MODIS (Moderate- Resolution Imaging Spectrometer) Airborne Simulator) instrument. The difference between the two threshholds is due to the wider bandwidths of the HIRS/2 8 and 11 μm channels.

On the other hand, 11 - 12 μm brightness temperature differences approach 0 with total water cloud coverage, but show small positive differences in clear-sky conditions, owing to differential water vapor absorption properties between the two wavelengths (Inoue, 1987). This test is useful as another check for low clouds having very uniform temperatures.

The cloud height test is a final check for the presence of middle and high level clouds. The CO_2-slicing method is very reliable in detecting clouds of these types (Menzel et al., 1983; Smith and Platt 1978).

The clear-sky detection is summarized in two flow charts in Figures 5

16

and 6. The first shows the steps in computing a regional clear-sky threshhold, the second details the final determination process for each FOV. These tests were incorporated into the CHAPS algorithm to optimize detection of clear-sky HIRS/2 observations. The algorithm and data structures were designed so that reprocessing of the data is a straightforward process.

3   Comparison with NESDIS Operational Radiances

This section compares climatologies of clear-sky radiances derived from the CHAPS procedure outlined above with HIRS/2 clear-sky radiances obtained from the TOVS operational sounding products data set. The TOVS sounding product data set contains clear-sky radiances from HIRS/2 as well as other TOVS instruments (MSU and SSU) used by NESDIS to produce operational retrievals of temperature and moisture which are subsequently distributed for assimilation into numerical weather prediction models. The objectives of this comparison are (1) to demonstrate the consistency between the two clear-sky radiance climatologies and (2) highlight regions of discrepancy between the two radiance data sets which are attributable to differences in the processing of the input radiance data stream. In particular, it will be shown that in certain climatological regions, the present cloud clearance algorithm provides significantly improved clear-sky radiance determination for atmospheric channels whose weighting fuctions peak in the lower atmosphere.

17

There are two important differences between the operational data processing performed by NESDIS and the CHAPS processing (described in section 2) which are relevant to the comparison: (1) Cloud clearance - The NESDIS operational cloud clearance algorithm, commonly referred to as the "N*" technique (Smith et al., 1979; McMillin and Dean, 1982), applies thresholds to the HIRS/2 radiance field to discriminate between clear and cloudy pixels. The most significant difference between this approach and the CHAPS procedure is the latter's use of high spatial resolution AVHRR measurements to determine the horizontal homogeneity of the radiance field within the HIRS/2 FOV. This feature enables more reliable discrimination between clear and partially cloud-filled HIRS/2 observations and is particularly useful for identifying low level clouds which may not produce a strong enough IR signature to be detected by NESDIS thresholds. (2) Angular correction - In addition to cloud clearance, NESDIS performs a limb correction which converts the original HIRS/ 2 radiances viewed at varying zenith angles to equivalent "nadir-view" radiances. No limb correction is performed in the CHAPS processing, instead radiances are restricted to within 30 degrees of nadir.

Following Ackerman et al (1992) we define a normalized spectral greenhouse parameter as

$$g_\lambda = \frac{B(T_s) - I_{\lambda cs}}{B(T_s)} \tag{3}$$

18

where $B(T_s)$ is the Planck function at wavelength λ and surface temperature T_s and $I_{\lambda cs}$ is the satellite observed clear-sky radiance. SSTs are derived from the collocated mean AVHRR clear-sky observations using the NOAA operational algorithm (McClain, 1989; Wade, 1993). Figure 7 shows the zonally averaged spectral greenhouse parameter from CHAPS (solid-line) and NESDIS (dashed line) for January from 3 different spectral channels; 6.7 μm, 7.3 μm, and 8.2 μm. The CHAPS data are from January 1994 whereas the NESDIS data represent a climatological average of Januarys from the period 1981-1990. The data represent zonal averages over ocean surfaces only. For channels whose weighting functions peak in the upper troposphere (6.7 μm, 7.3 μm), zonal variations in the greenhouse parameter are in good agreement with each other. Differences are typically less than 2%, or roughly 0.5 K in terms of equivalent brightness temperatures. The study of Bates and Wu (1995) suggests that intercalibration differences in 6.7 μm brightness temperatures between successive NOAA satellites is between 0.1 and 0.5K.

Larger discrepancies between CHAPS and the NESDIS observations exist for the lower tropospheric water vapor sensitive channel (8.2 μm). In particular, for latitudes poleward of 40° the NESDIS data exhibit a significantly larger greenhouse parameter especially in the northern (winter) hemisphere where differences range from 50-100%. These differences reveal that the NESDIS radiances at 8.2 μm are systematically colder than

19

the CHAPS radiances. A similar pattern of discrepancy is noted over the southern hemisphere mid-latitudes during July (not shown).

A comparison of the two datasets as a function of SST is presented in Figure 8. Individual points correspond to CHAPS radiances. The solid and dashed lines correspond to the mean and ± 1 standard deviation of the NESDIS radiances binned as a function of SST. Good agreement is apparent for the upper tropospheric channels (6.7 μm and 7.3 μm) illustrating that both climatologies show a nearly identical dependence upon SST. Both climatologies exhibit an increase in g_λ with increased SST and a non-linear rise at the warmest SSTs; however, in the 8.2 μm channel, the NESDIS greenhouse parameter is systematically larger than the CHAPS greenhouse parameter. The discrepancy is greatest for cold SSTs, consistent with the zonal average plots shown above. Indeed for cold SSTs, the NESDIS data depict a slight decrease in g_λ with increasing SST. This is contrary to what is expected based upon observations that atmospheric water vapor generally increases with increasing SST (Stephens 1990). This comparison suggests that the NESDIS 8.2 μm radiances contain a systematic cold bias, particularly over cold, mid-latitude ocean surfaces.

The presence of a cold bias in the NESDIS radiances for only the 8.2 μm channel suggests a contamination of the NESDIS clear-sky radiances by low cloud cover. This is consistent with the observation of largest bias over cold, mid-latitude oceans where low cloud cover is most frequent. To examine

20

this issue in more detail, Figure 9 compares a histogram of the instantaneous (daily) NESDIS oceanic, clear-sky 8.2 μm brightness temperatures (BT) with results from CHAPS for two geographic regions: (top) northern hemisphere mid-latitudes (45N-55N) and (bottom) the sub-tropics (20N-30N). A distinct skew in the histogram towards lower BT is apparent in the NESDIS values. This supports the hypothesis that the NESDIS radiances are cloud contaminated by low cloud cover. Since clouds are generally colder than the underlying atmosphere/surface, classification of partially-cloudy FOVs as clear results in a tail of cloud contaminated BT extending towards lower values. The CHAPS BT (dark wide bars) on the other hand, exhibit a much more gaussian distribution consistent with that expected for completely cloud-free FOVs. The maximum values in the two histograms are more similar in the sub-tropical region, resulting in a similar mean between the two algorithms.

Since the NESDIS-processed radiance data set provides a 15+ year climatology of archived spectral parameters, it is worthwhile investigating the extent to which channels sensitive to the lower troposphere may be corrected to remove the impact of the low cloud cover. As noted above, cloud contamination generally results in a "tail" of cold radiances which introduces a systematic bias in the monthly mean. In these situations, a more robust statistic of the typical clear-sky radiance for a given month may be provided by the mode of the daily measurements for a particular

21

grid box, rather than the mean. By choosing the peak of the frequency distribution, the impact of the outlying (e.g. cloud contaminated) data points upon the estimate of the central tendency is removed. Figure 10 shows a comparison between several zonally averaged 8.2 μm clear-sky quantities: CHAPS monthly mean BT (thick line), NESDIS monthly mean BT (thin line), and NESDIS mode (dotted line). The use of the mode clearly results in improved agreement over the mid- latitudes, although the agreement is still not perfect. This suggests that the mode, rather than the mean, provides the better estimate of the central tendency of the NESDIS clear-sky 8.2 μm radiance distribution, particularly for regions with extensive low level cloud cover.

4 Analysis of CHAPS

Satellite-based measurements have improved our understanding of the processes involving global climate change. One example is the use of broadband data from the Earth Radiation Budget Experiment (ERBE) to study the atmospheric greenhouse effect and its relationship to sea surface temperature. Water vapor is the most important gas in the atmospheric feedback mechanism known as the greenhouse effect. Water vapor feedbacks are also a major source of uncertainty in the prediction of climate change. The presence of water vapor affects the radiative properties of the atmosphere and impacts the development of clouds. Observational studies of the radiative

22

effects of water vapor have recently made use of the broadband greenhouse parameters;

$$g = \frac{\sigma T_s^4 - \text{OLR}_{cs}}{\sigma T_s^4} \qquad (4)$$

$$\mathcal{G} = \frac{\sigma T_s^4}{\text{OLR}_{cs}} \qquad (5)$$

where T_s is the sea surface temperature (SST), σ is the Stefan-Boltzman constant and OLR_{cs} is the measured clear-sky broadband outgoing long-wave flux at the top of atmosphere. The normalized greenhouse parameter (equation 4) was defined by Raval and Ramanathan (1989). Plotted versus SST, the greenhouse parameter is a demonstration of the atmospheric water vapor feedback to SST variation. In addition to providing physical insight into the coupling between the atmosphere and oceans, this parameter is also used to validate climate models. Raval and Ramanathan (1989) illustrated the broadband relationship between the greenhouse parameter and SST and demonstrated that the relationship was mainly due to changes in total column precipitable water content. In addition to understanding the general trend of increasing g with increasing SST, it is important to understand the range in g for a given SST. Stephens and Greenwald (1991) found a similar relationship between g and SST and used simple model calculations to demonstrate that the variability of $\mathcal{G}$ (equation 5) as a function of SST was associated with changes in the vertical distribution of water

23

vapor and the temperature lapse rate. Ackerman et al (1992) used observations to demonstrate the dependency of the greenhouse parameter on upper tropospheric water vapor using collocated broadband and 6.7 μm spectral observations. They also defined a greenhouse parameter in terms of spectral observations. Webb et al (1993) used broadband observations and model simulations to explain some of the variability of the relationship between the greenhouse parameter and SST. Understanding the causes of variability in the relationship between the greenhouse parameter and SST is necessary for providing insights into climate variations. The following paragraphs address this issue using clear-sky spectral observations.

The relationship between the spectral greenhouse parameter for wavelengths of 11, 8.2, 7.3 and 6.7 μm and SST are depicted in Figures 11 and 12 for July 1993 and January 1994 respectively. The quantities shown were generated by averaging over 2.5 degree ERBE grid boxes (ERBE Data Management Team, 1991). The higher in the atmosphere that a spectral channel's weighting function peaks (see Table 1), the colder the temperature and therefore the larger the spectral greenhouse parameter. The increase in $g_{8.2}$ and g_{11} with SST is related to the increase in precipitable water with SST. This is similar to the relationship presented by Ackerman et al (1992) in their regional study using collocated AVHRR, HIRS/2 and ERBE measurements. The coupling of $g_{7.3}$ and $g_{6.7}$ with SST results from large scale circulation patterns, which are also linked to the SST. The dependence of

24

$g_{8.2}$ and $g_{6.7}$ on SST is demonstrated in Figure 13 which depicts the brightness temperature of 8.2 and 6.7 μm ($BT_{8.2}$ and $BT_{6.7}$) as a function of SST for the month of January. The dependence of BT_{11} is similar to $BT_{8.2}$ while $BT_{7.3}$ is similar to the dependency of $BT_{6.7}$. The strong dependence on SST in these lower tropospheric-sensitive channels is due, in part, to surface emitted radiance being transmitted through the atmosphere. Note the change in slope between $BT_{8.2}$ and SST that occurs at a SST of approximately 297K as noted by Ackerman et al (1992). The connection between the $BT_{6.7}$ and SST is influenced by atmospheric circulation patterns, which are themselves a function of SST. For example, tropical convection transports moisture into the upper troposphere and is associated with warm SSTs, while subsidence dries the upper troposphere and is observed over the cool waters associated with persistent stratus regimes. As the SST increases, $BT_{6.7}$ increases slightly until approximately 290K after which it remains the same with increasing SST.

As with SST and the broadband greenhouse parameter, g_{λ} has a geographic dependence. Figures 14a and 14b show the CHAPS monthly mean $g_{6.7}$ and $g_{8.2}$ respectively, for January 1994 (top) and July 1993 (bottom). Dark blue regions are areas where CHAPS did not retrieve high-confidence clear-sky radiances and therefore no greenhouse parameter. From the definition of g_{λ}, values close to 1 result when the radiant exitance out the top of the atmosphere has a much smaller magnitude than the radiance entering

25

the bottom of the atmosphere. Spectral regions where the atmosphere is weakly absorbing generally have small values of g_λ. Geographic regions of persistent convection generally have moist atmospheres and therefore this is where the spectral greenhouse parameter reaches its maximum value. Regions of persistent subsidence generally have dry middle and upper tropospheres and thus lower values of g_λ. Oceanic tropical convective regions generally coincide with warm SSTs, while subsident regions west of the continents have oceanic upwelling and cooler SSTs which act to enhance the geographic patterns of g_λ. However, not all regions with warm SSTs have high g_λ values. For example, consider the Arabian Sea during July. This entire body of water is warm, yet there is a strong gradient in $g_{8.2}$. The high values in the eastern Arabian Sea (≈ 0.25) are a consequence of the deep moist layer associated with the southwest summer monsoon. But a low-level temperature inversion exists in the western half, confining much of the moisture to the warm boundary layer which results in a smaller value of $g_{8.2}$ (≈ 0.17).

Webb et al (1993) noted that the variability in the broadband greenhouse parameter as a function of SST differed between the winter and summer hemispheres. By combining the broadband observations with model calculations, they found that water vapor was primarily responsible for variations in the $\mathcal{G}$ in the tropics while temperature variations explained much of the variability in the mid-latitudes. The spectral observations of g_λ allow for direct observations of these variations.

26

Figure 15a-d shows diagrams of g_λ as a function of latitude (negative values are southern hemisphere) for HIRS/2 channels 8, 10, 11 and 12 (11, 8.2, 7.3 and 6.7 μm respectively). Values of the spectral greenhouse parameter were averaged over 10° latitude bands. The center points represent the means and the boxes plus and minus a standard deviation. The solid circles represent January values and the open diamonds July measurements. Maximum values occur in the tropics where SSTs are warmest and water vapor concentrations greatest. Commonalities are strong between the summer and winter hemispheres. For example, peak values occur within 10 degrees of the equator in the summer hemisphere. For the region between approximately 40°N and 40°S the latitudinal values of g_λ are seasonally dependent. Except for g_{11}, there is a seasonal symmetry in g_λ – the latitudinal mean value for the southern hemisphere summer matches well with the corresponding latitudinal mean value of the northern hemisphere summer. The dependence on season is small poleward of 40°. The standard deviations in these plots reveal large variations of g_λ within latitude zones, but which generally decrease towards the poles. This occurs for all four of the HIRS/2 spectral channels sensitive to water vapor. It is also apparent that the standard deviations of g_λ in these water vapor-sensitive bands are somewhat seasonally dependent, especially between 40°N and 40°S. The largest variability across a latitude band occurs in the tropics and subtropics. This zonal variability decreases with increasing height in

27

the troposphere (as the height of the channels' peak in weighting functions increases). However, there is only small temporal variability during the two months of the study in tropical convective regions (figure not shown).

In addition to the water vapor vertical distribution, the greenhouse effect of the atmosphere is also a function of its temperature structure. Spectral radiance measurements can be used to asses the relative importance of the atmospheric water vapor and temperature distribution in defining the greenhouse parameter. For example, the 14.2 μm radiance (HIRS/2 channel 4) is in a CO_2-absorption band and is primarily sensitive to atmospheric temperature with a peak in the weighting function at approximately 250 mb. Latitudinal variations in the July and January spectral greenhouse parameter at 14.2 μm are depicted in Figure 16. The $g_{14.2}$ is a strong function of season poleward of approximately 40°. Unlike the water vapor channels, the temperature-sensitive channel shows greatest variation in the mid-latitudes and only small variability in the tropics.

The seasonal dependence of $g_{14.2}$ and $g_{13.6}$ (HIRS/2 channels 4 and 6) on SST is demonstrated in Figure 17. The circles and crosses represent $g_{14.2}$ in the summer and winter hemispheres respectively, while the triangles and stars represent the corresponding values for $g_{13.6}$. In tropical regions which are associated with warm oceans, for a given SST, there is a small range of the spectral greenhouse parameter and there is no seasonal dependence. In the mid-latitude summer hemisphere, as the SST increases, the $g_{14.2}$

28

and $g_{13.6}$ also increase, which is indicative of a warmer upper troposphere with little variability. During winter, for a given SST colder than approximately 285K, there is an increased variability in $g_{13.6}$ and $g_{14.2}$. This winter variation is associated with the presence of mid-latitude cyclones and accompanying changes in the height of the tropopause as well as changes in the atmospheric lapse rate. The winter troposphere is colder than the summer, which enhances the difference between the effective temperatures of the atmosphere and oceans and leads to a larger $g_{14.2}$ and $g_{13.6}$. The difference in mean lapse rate between winter and summer, 6.03 K/km versus 5.91 K/km (Houghton, 1986), also contributes to larger values of $g_{14.2}$ and $g_{13.6}$ during winter. In the tropics, there is little seasonal variation in the tropospheric temperature, and thus smaller variations in $g_{13.6}$ and $g_{14.2}$.

5   Relation Between Spectral and Broadband Greenhouse Parameters

In this section, we investigate the relationship between the broadband greenhouse parameter g, as measured by ERBE, and the spectral greenhouse parameter g_λ, determined from the NESDIS archived data set. We have chosen the NESDIS data set because the CHAPS data do not overlap in time with the ERBE scanner observations. The relationship between the broadband greenhouse parameter and SST has been discussed in several papers (e.g. Raval and Ramanathan, 1989; Stephens and Greenwald,

1991; Webb et al 1993). In Figures 18a and 18b, the abscissa is sea surface temperature and the ordinate is the broadband greenhouse parameter. The shaded regions are an indication of the range of g for a given SST. Corresponding averaged spectral greenhouse parameter values were determined over 1 degree intervals of SST and over 0.01 in the broadband greenhouse parameter. The shaded areas and contours in Figure 18a (18b) represent the averaged values of $g_{6.7}$ ($g_{14.0}$) for the given interval of SST and g. This binning is similar to that of Raval et al. (1994) who investigated the dependence of outgoing longwave radiation on sea surface temperature and moisture. Figure 18a demonstrates that for warm SSTs, the range in g is associated with differences in $g_{6.7}$, while for cooler SSTs, variations in $g_{6.7}$ are small and do not explain the large range of g for a given SST. As an example, for an SST of 300K the broadband greenhouse parameter, g, ranges between approximately 0.33 and 0.4. The smaller values of g are associated with small values of $g_{6.7}$ (0.68) and as g increases to 0.4, $g_{6.7}$ increases to 0.82. For a SST of 280K, $g_{6.7}$ ranges from 0.7 to 0.72, while its broadband counter-part varies from .25 to .35. The ranges of g as a function of a given SST can also be interpreted as occurring due to changes in upper tropospheric humidity (UTH). Figure 19 is similar to Figure 18a, except the contours represent the UTH computed from the HIRS/2 observed 6.7 μm radiances, following the method of Soden et al (1993). For warm SSTs, the range in g is associated with the magnitude of the UTH. For a given

30

SST, a moist upper troposphere will have a larger g than an atmosphere with a lower UTH. For SSTs less than approximately 288K, the UTH is relatively uniform, and therefore cannot explain the observed range in g for a given SST.

For cool SSTs, the range in the broadband g is associated with variations in the channels sensitive to upper tropospheric temperature. Figure 18b shows that for a SST of 280K, $g_{14.0}$ ranges from approximately 0.4 to 0.5. For warm SSTs associated with the tropics, $g_{14.0}$ shows little variation.

The magnitude of the greenhouse parameter is a function of the total water vapor loading and the temperature structure of the atmosphere. Figures 18 and 19 demonstrate that the range in g for warm, tropical SSTs is driven by spectral changes at wavelengths sensitive to upper tropopsheric water vapor. For the cooler SSTs, generally associated with the middle latitudes, the range in g is a function of spectral greenhouse parameter sensitive to the temperature structure of the upper troposphere.

The spectral and broadband observations discussed above provide a useful diagnostic tool with which to study relationships between various atmospheric processes which may be associated with climate change. In addition, they provide a reference data set to use when evaluating the performance of models which predict atmospheric circulations. Understanding model deficiencies through comparisons of model output with observations is not straightforward. For example, it is simple to compare the observed outgoing longwave radiation with model simulations; however, if discrepencies

exist it is sometimes difficult to assess the cause. When agreement occurs, it may not be for the correct reasons, as individual model errors may compensate one another. Including the spectral observations with the broadband measurements provides additional consistency checks. For example, in Figure 20 the observed broadband and spectral radiative budget parameters are compared with those predicted by the Geophsycial Fluid Dynamics Laboratory (GFDL) general circulation model (GCM). The GFDL GCM, described by Wetherald et al. (1991), is a spectral-transform model with 14 vertical levels and is rhomboidally truncated at wavenumber 30, which is approximately equivalent to a horizontal resolution of 2.25° latitude × 3.75° longitude. The model integration was performed for 10 years (1979-1988) using external conditions prescribed by the Atmospheric Model Intercomparison Project (AMIP). The predicted spectral radiance fields are computed by inserting the model profiles of temperature and moisture into the CIMSS transmittance model to simulate the radiance which would be observed by the satellite under those conditions. Both the observed and model results presented here correspond to four year averages from the period 1985-1988. The solid lines represent the mean relationship between the GCM greenhouse parameter and precipitable water (PW), while the dashed lines represent the variability as measured by the standard deviation. The points represent observations; the precipitable water was determined from the SSM/I (Special Sensor Microwave Imager) instrument (Liu et al, 1992),

32

the NESDIS spectral (diamonds and circles) and ERBE (triangles) broad-band greenhouse parameters were determined as discussed above. For small PW values (less than approximate 20 Kg/m^2), the model is in agreement with the observations of g, both in magnitude and range. For values of PW greater than approximately 20 Kg/m^2, the model is over-estimating the broadband g and $\frac{\Delta g}{\Delta PW}$. When comparing to the spectral measurements, we see that the model is overestimating both $g_{14.2}$ and $g_{6.7}$ for large PW. The model is also overestimating $\frac{\Delta g_{6.7}}{\Delta PW}$. The observations also exhibit a larger range in $g_{6.7}$ for a given PW than displayed by the model.

6 Summary

Only a few procedures currently exist which derive atmospheric properties using global satellite radiance measurements. ISCCP (e.g., Rossow and Schiffer, 1991; Schiffer and Rossow, 1983) uses visible and infrared imager data from geostationary and polar orbiting satellites to derive various cloud products. Wylie et al (1994) use sounder data to produce global analyses of effective cloud amount and cloud top pressure. Stowe et al (1991) use the AVHRR data to develop global cloud products while Rao et al (1989) present the method used by NOAA to produce global aerosol amount. The National Environmental Satellite Data and Information Service (NESDIS) has for many years produced atmospheric temperature and moisture profiles operationally using the TIROS-N Operational Vertical Sounder (e.g. Smith

33

et al, 1979). Many other satellite techniqes have been developed for regional applications as well as for deriving global surface properties.

The approach presented in this paper is to collocate observations from the Advanced Very High Resolution Radiometer (AVHRR) and High-resolution Infrared Sounder (HIRS/2) in order to determine global climate parameters. The Collocated HIRS/2 and AVHRR ProductS (CHAPS) include cloud type and amount, spectral cloud forcing and the spectral greenhouse parameter, as well as the collocated radiance data. All are available from the authors. The algorithm was run in an operational mode during the months of July 1993, January 1994, and July 1994, though the current study does not present results for July 1994. The authors discuss the CHAPS oceanic clear-sky determination procedure and some analyses of the spectral greenhouse parameter as a function of sea surface temperature, geographic region and season. The results of the current study can be summarized as follows:

- The capability to collocate imager and sounder data and derive a variety of global climate products in near-real time has been demonstrated. Such an approach can easily be adapted to an operational proceedure or applied to historical data sets.

- A comparison of CHAPS results with the historical NESDIS clear-sky radiances suggests that the NESDIS 8.2 μm radiances contain a systematic cold bias, particularly over cold, mid-latitude oceans. For these

34

regions, the mode rather than the mean, provides a better estimate of the central tendency of the NESDIS clear-sky 8.2 μm radiance distribution.

- The spectral greenhouse parameter measured in water vapor-sensitive channels with weighting functions peaking in the lower atmosphere have values which are directly coupled to the SST. In channels sensitive to middle and upper tropospheric water vapor, g_λ is also dependent on SST via its connection to large scale atmospheric circulation patterns. The spectral greenhouse parameter measured in all the water vapor sensitive channels are dependent on the atmospheric total precipitable water, increasing with increasing water vapor loading.

- Water vapor sensitive channels display latitudinal variations of the spectral greenhouse parameter which generally decrease poleward, in agreement with the simulations of Webb et al (1993). These channels show large standard deviations of g_λ with latitude.

- The water vapor sensitive channels display the largest variability of g_λ in the tropics while $g_{14.2}$ has minimum variability in the tropics and largest variation in the mid-latitudes. These spectral observations support the broadband study of Webb et al (1993).

- Variability in the relationship between g_λ sensitive to water vapor and SST shows only a weak dependence on season. A strong seasonal dependence is observed, however, for the 14.2 μm upper tropospheric

35

temperature-sensitive channel. Large variations are observed in the winter hemisphere and are likely associated with changes in the height of the tropopause and in the vertical temperature structure of the atmosphere during the progression of mid- latitude cyclones.

- For warm SSTs, the range in the broadband greenhouse parameter, g, is associated with changes in the spectral greenhouse parameter sensitive to upper tropospheric water vapor. For cooler SSTs, the range in the broadband g is associated with changes in the spectral greenhouse parameter sensitive to upper tropospheric temperature.

7 References

Ackerman, S. A., R. A. Frey, and W. L. Smith, 1992: Radiation budget studies using collocated observations from AVHRR, HIRS/2 and ERBE instruments. *J. Geophys. Res.*, **97**, 11513-11525.

Aoki, T., 1980: A method for matching the HIRS-2 and AVHRR pictures of TIROS-N satelllites. *Meteorological Satellite Center Tech. Note 2*, Tokyo, Japan, 15-26.

Bates, J. J., and X. Wu, 1995: Interannual variability of upper troposphere water vapor band brightness temperature, submitted *J. Climate*

Baum, B. A., R. F. Arduini, B. A. Wielicki, P. Minnis and S. -C. Tsay, 1994: Multilevel cloud retrieval using multispectral HIRS and AVHRR Data: Nighttime oceanic analyis. *J. Geophys. Res*, **99**, 5499-5514.

Baum, R. A., B. A. Wielicki and P. Minnis, 1992: Cloud-property retrieval using merged HIRS and AVHRR data. *J. Appl. Met.*, **31**, 351-369.

Brown, S. R., 1991: Amendments to *NOAA Tech. Memo.*, NESS **107** Appendix B. Memorandum.

Derrien, M., B. Farki, L. Harang, H. LeGleau, A. Noyalet, D. Pochic, and A. Sairouni, 1993: Automatic cloud detection applied to NOAA-11/AVHRR imagery. *Remote Sens. Environ*, **46**, 246-267.

ERBE Data Management Team, 1991: Earth radiation budget experiment (ERBE) data management system: the regional, zonal, and global gridded averages: S-4G user's guide. *Report ERBE 3-3-12-11-91-01-0*, NASA Langley Research Center, Hampton, VA.

Hayden, C. M. and B. F. Taylor, 1985: The application of AVHRR data to fine scale temperature and moisture retrievals obtained from NOAA satellites. *Preprint Volume 14th Conference on Severe Local Storms*, 29 October - 1 November, Indianapolis, IN, Amer. Meteor. Soc., J22-J28.

Houghton, J. T., 1986: *The Physics of Atmospheres.* Cambridge Univ. Press, 271 pp.

Inoue, T., 1987: A cloud type classification with NOAA 7 split window measurements. *J. Geophys. Res.*, **92**, 3991-4000.

Kidwell, K. B., 1991: NOAA Polar Orbiter Users Guide. U.S. Dept. Commerce.

Levanant, L., 1989: AVHRR/HIRS coupling, in *Proceedings of the 5th International TOVS Conference*, Toulouse, France (A. Chedin, Ed.), LMD, France, pp. 247-259.

Liu, T. T., W. Tang, and F. Wentz, 1992: Precipitable water and surface humidity over oceans for the SSM/I and ECMWF. *J. Geo. Res.*, **97**, 2251-2264.

38

Menzel, W. P., W. L. Smith, and T. R. Stewart, 1983: Improved cloud motion wind vector and altitude assignment using VAS. *J. Appl. Metero.*, **22**, 377-384.

McClain, E. P., 1989: Global sea surface temperatures and cloud clearing for aerosol optical depth estimates. *Int. J. Remote Sensing*, **10**, 763-769.

McMillin, L. M. and C. Dean, 1982: Evaluation of a new operational technique producing clear radiances, *J. Appl. Meteor.*, **21**, 1005- 1014.

Rao, C. R. N., L. L. Stowe and E. P. McClain, 1989: Remote sensing of aerosols over the oceans using AVHRR data: Theory, practice and application. *Int. J. Remote Sens.*, **10**, 743-749.

Raval, R. and V. Ramanathan, 1989: Observation determination of the greenhouse effect. *Nature*, **342**, 758-761.

Raval, A., A. H. Oort, and V. Ramaswamy, 1994: Observed dependence of outgoing longwave radiation on sea surface temperature and moisture, *J. Climate*, **7**, 807-821.

Rossow, W. B., and R. A. Schiffer, 1991: ISCCP cloud data products. *Bull. Amer. Meteor. Soc.*, **72**, 2-20.

Schiffer, R. A. and W. B. Rossow, 1983: The International Satellite Cloud Climatology Project (ISCCP): The first project of the World Climate Research Programme. *Bull. Amer. Meteor. Soc.*, **64**, 779-784.

Smith, W. L., and C. M. R. Platt, 1978: Comparison of satellite-deduced cloud heights with indications from radiosonde and ground-based laser measurements. *J. Appl. Meteor.*, **17**, 1796-1802.

Smith, W. L., H. M. Woolf, P. G. Abel, C. M. Hayden, M. Chalfant, and N. Grody, 1974: Nimbus 5 sounder data processing system, part 1: measurement characteristics and data reduction procedures. *NOAA Tech. Memo.*, NESS **57**, Washington, DC.

Smith, W. L., H. M. Woolf, C. M. Hayden, D. Q. Wark and L. M. McMillin, 1979: The TIROS-N operational vertical sounder. *Bull. Amer. Meteor. Soc.*, **60**, 1127-1150.

Soden, B. J. and F. P. Bretherton, 1993: Upper tropospheric relative humidity from the GOES 6.7 micron channel: method and climatology for July 1987, *J. Geo. Res.*, **98**, 16669-16688.

Stephens, G. L., 1990: On the relationship between water vapor over the oceans and sea surface temperature, *J. Climate*, **3**, 634-645.

Stephens, G. L. and T. J. Greenwald, 1991: The Earth's radiation budget and its relation to atmospheric hydrology: 1. Observations of the clear-sky greenhouse effect. *J Geophys Res*, **96**, 15325-15340.

Stowe, L. L., E. P. McClain, R. Carey, P. Pellegrino, G. Gutman, P. Davis, C. Long and S. Hart, 1991: Global distribution of cloud cover derived

from NOAA/AVHRR operational satellite data. *Advan. Space Res.*, **11**, 51-54.

Strabala, K. I., S. A. Ackerman, and W. P. Menzel, 1994: Cloud properties inferred from 8-12-μm data. *J. Appl. Meteor.*, **33**, 212-229.

Suomi, V. E., R. J. Fox, S. S. Limaye, and W. L. Smith, 1983: McIDAS III, a modern interactive data analysis facility. *J. Appl. Meteor.*, **22**, 766-788.

Wade, G. S., 1993: Personal correspondance.

Webb, M. J., A. Slingo and G. L. Stephens, 1993: Seasonal variation of the clear-sky greenhouse effect: the role of changes in atmospheric temperatures and humidities. *Climate Dynamics*, **9**, 117-129.

Wetherald, R. T., V. Ramaswamy, and S. Manabe, 1991: A comparative study of the observations of high clouds and simulations by an atmospheric general circulation model. *Climate Dyn.*, **5**, 135-143.

Wylie, D. P., W. P. Menzel, H. M. Woolf and K. I. Strabala, 1994: Four years of global cirrus cloud statistics using HIRS. *J. Climate*, **7**, 1972-1986.

8 Acknowledgments

9 Table and Figure Captions

Table 1. HIRS/2 channel spectral responses and descriptions (after Kidwell, 1991).

Table 2. AVHRR channel spectral responses and descriptions (after Kidwell, 1991).

Figure 1a. Histogram of AVHRR (GAC) 11μm brightness temperatures from an entire ISCCP region centered at 26.3 N latitude and 90.7 W longitude.

Figure 1b. Histogram of AVHRR (GAC) 11μm brightness temperatures taken from collocated HIRS/2 footprints. Region is centered at 26.3 N latitude and 90.7 W longitude.

Figure 2. Regional histogram of AVHRR 11μm brightness temperatures.

Figure 3. Histogram of AVHRR 11μm observations which met the "possibly clear-sky" criteria (see text).

Figure 4. Time series of Reynolds' blended SST, regional maxima of mean collocated AVHRR 11μm observations and first guess clear-sky threshholds for the month of January 1994. Region is centered at 18.75S, 107.13W.

Figure 5. Flowchart showing the steps in computing a regional clear-sky threshhold.

Figure 6. Flowchart showing the final clear-sky determination process for each collocated FOV.

Figure 7. Oceanic zonal mean spectral greenhouse parameter from CHAPS (solid lines) and NESDIS (dashed lines) at 6.7 μm (top), 7.3μm (middle) and 8.2 μm (bottom). CHAPS data are from January 1994 while that of NESDIS includes January data from 1981-1990.

Figure 8. Oceanic spectral greenhouse parameter from CHAPS (dots) and NESDIS (lines) at 6.7 μm (top), 7.3μm (middle) and 8.2 μm (bottom as a function of SST for January. Solid and dashed lines represent the mean and $\pm$1 standard deviation of the NESDIS values.

Figure 9. Frequency histogram of observed HIRS/2 oceanic clear-sky 8.2 μm brightness temperatures from 45N-55N latitude (top) and 20N-30N latitude (bottom). Dark wide bars indicate clear-sky determination using the CHAPS algorithm for January 1994 while lighter bars denote clear-sky determination using the NESDIS (TOVS) algorithm for January during 1981-1990.

Figure 10. Oceanic clear-sky brightness temperature. The thick and thin lines correspond to the zonal mean CHAPS January 1994 data and NESDIS 1981-1990 January data respectively. The dotted line represents zonal means of NESDIS gridbox mode values.

Figure 11. The spectral greenhouse parameter for wavelengths of 11, 8.2, 7.3 and 6.7 μm as a function of SST for July 1993.

Figure 12. The spectral greenhouse parameter for wavelengths of 11, 8.2, 7.3 and 6.7 μm as a function of SST for January 1994.

Figure 13. Brightness temperature of 8.2 and 6.7 μm ($BT_{8.2}$ and $BT_{6.7}$) as a function of SST for the month of January.

Figure 14a. Geographic distribution of the CHAPS derived January (top) and July (bottom) monthly mean values of $g_{6.7}$.

Figure 14b. Geographic distribution of the CHAPS derived January (top) and July (bottom) monthly mean values of $g_{8.2}$.

Figure 15a-d. Diagram of g_λ as a function of latitude (negative values are southern hemisphere) for HIRS/2 channel 8, 10, 11 and 12 (11, 8.2, 7.3 and 6.7 μm respectively). The center points represent the latitudinal mean and the boxes denote plus and minus the standard standard deviation. The solid circles represent January values and the open diamonds July measurements.

Figure 16. Latitudinal variations in the July and January spectral greenhouse parameter at 14.2 μm (see Figure 15).

Figure 17. Spectral greenhouse parameter as a function of SST. The circles and crosses represent the values of $g_{14.2}$ in the summer and winter hemispheres respectively, while the triangles and stars represent the corresponding values of $g_{13.6}$.

Figure 18. Relationship between the ERBE derived broadband greenhouse parameter and SST. The contoured regions represent the averaged values of $g_{6.7}$ (a) and $g_{14.0}$ (b) for the given interval of SST and g. See text for details.

Figure 19. Relationship between the ERBE derived broadband greenhouse parameter and SST. The contoured region represents the averaged values of upper tropospheric relative humidity (UTH) for the given interval of SST and g. See text for details.

Figure 20. Relationship between greenhouse parameter and precipitable water. Solid lines represent model output with dashed lines indicating variability. Circles and diamonds are derived NESDIS spectral greenhouse parameter values for $g_{6.7}$ and $g_{14.0}$. Triangles represent ERBE broadband g.

Table 1
NOAA-12 HIRS/2 Channel Spectral Responses

Channel #	Central Wavenumber (cm^{-1})	Central Wavelength (microns)	Appx. Peak in Wt. Function (mb)	Description
1	667.58	15.0	30	15 micron
2	680.18	14.7	60	CO$_2$ band
3	690.01	14.5	100	"
4 *	704.22	14.2	250	"
5 *	716.32	14.0	500	"
6 *	732.81	13.7	750	"
7 *	751.92	13.3	900	"
8 *	900.45	11.1	surface	Window
9	1026.66	9.7	25	Ozone
10 *	1223.44	8.2	900	Water
11	1368.68	7.3	600	vapor
12	1478.59	6.7	400	"
13	2190.37	4.6	950	4.3 micron
14	2210.51	4.52	850	CO$_2$ band
15	2236.62	4.47	700	"
16	2267.22	4.1	600	"
17	2361.44	4.2	5	"
18	2514.68	4.0	surface	"
19	2653.48	3.8	surface	Window
20	14500.00	0.69	–	Visible

Table 2
NOAA-12 AVHRR Channel Spectral Responses

Channel #	Central Wavenumber (cm^{-1})	Central Wavelength (microns)	Appx. Peak in Wt. Function (mb)	Description
1	15673.98	0.64	–	Visible
2 *	11997.60	0.83	–	Near-IR
3 *	2639.61	3.8	surface	Window
4 *	921.03	10.9	surface	Window
5 *	837.36	11.9	surface	Water vapor continuum

* Indicates a channel used in CHAPS cloud clearing

Complete AVHRR (GAC) Histogram over ISCCP Region

Number

11 micron Brightness Temperature

Partial AVHRR (GAC) Histogram over ISCCP Region

Collocated Pixels Only

Number

11 micron Brightness Temperature
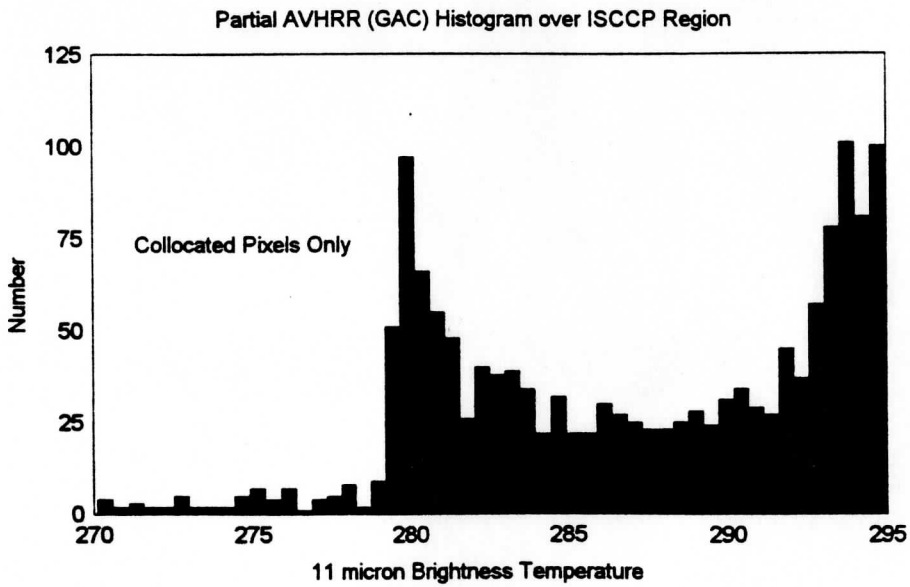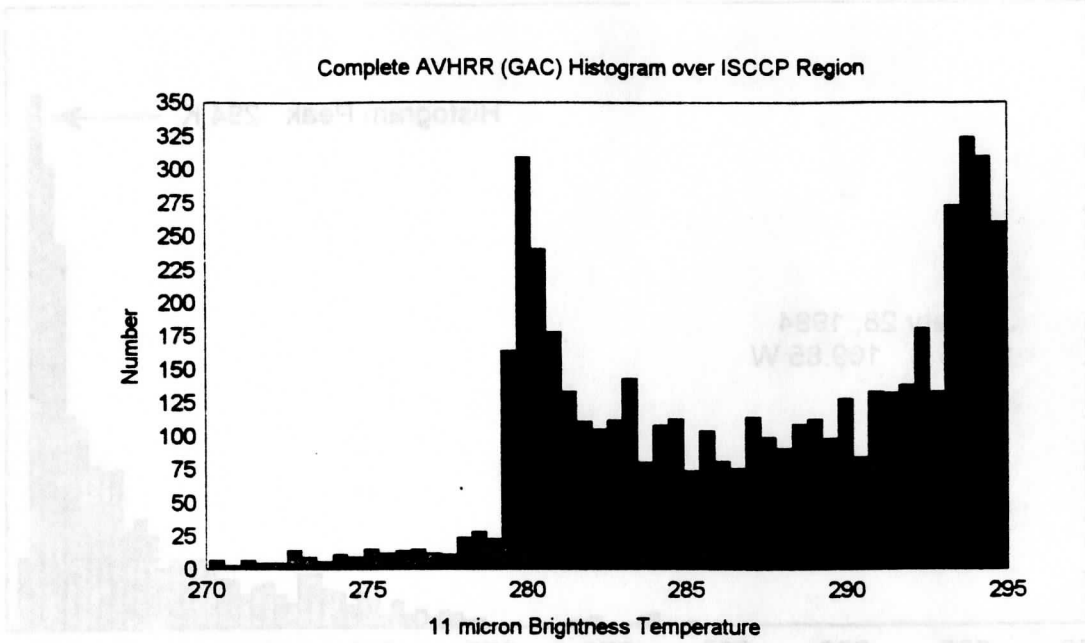
Regional AVHRR (GAC) Histogram

January 28, 1994
18.75 S   109.85 W

Histogram Peak   294 K →

11 micron Brightness Temperature
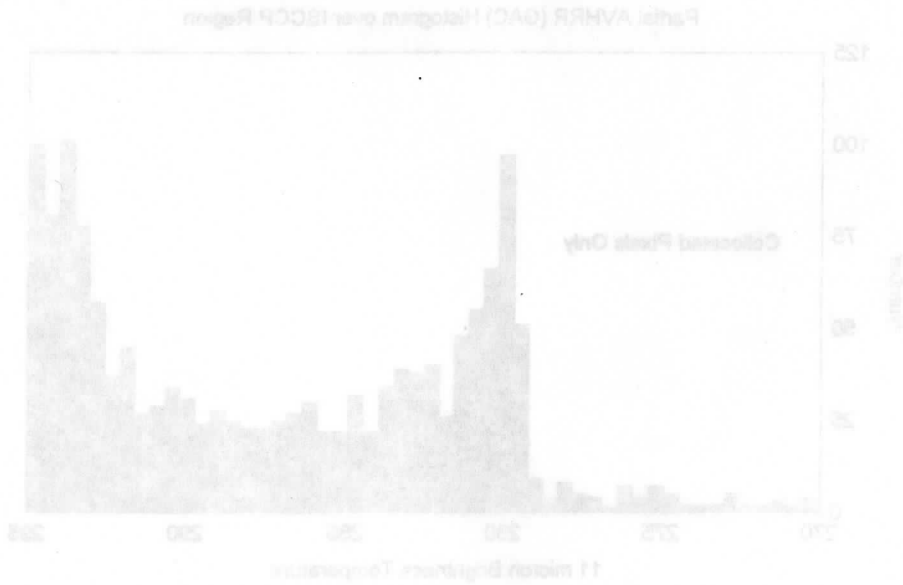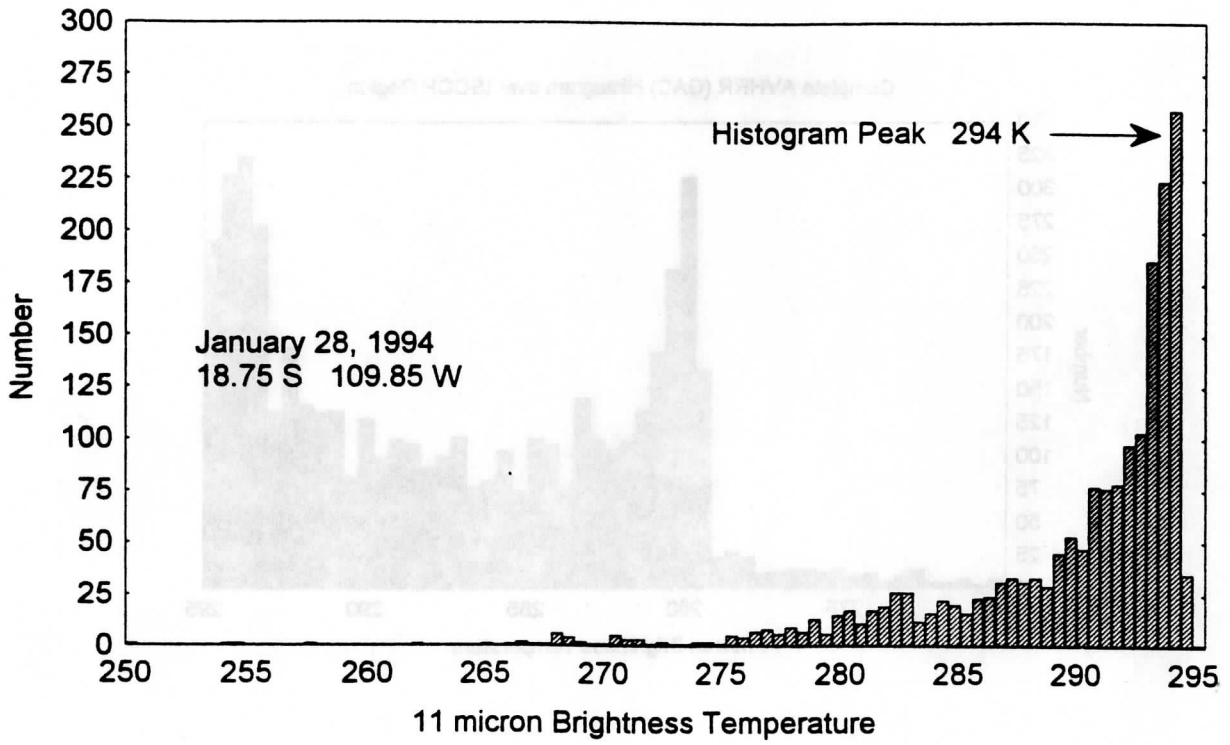
Clear Sky Histogram
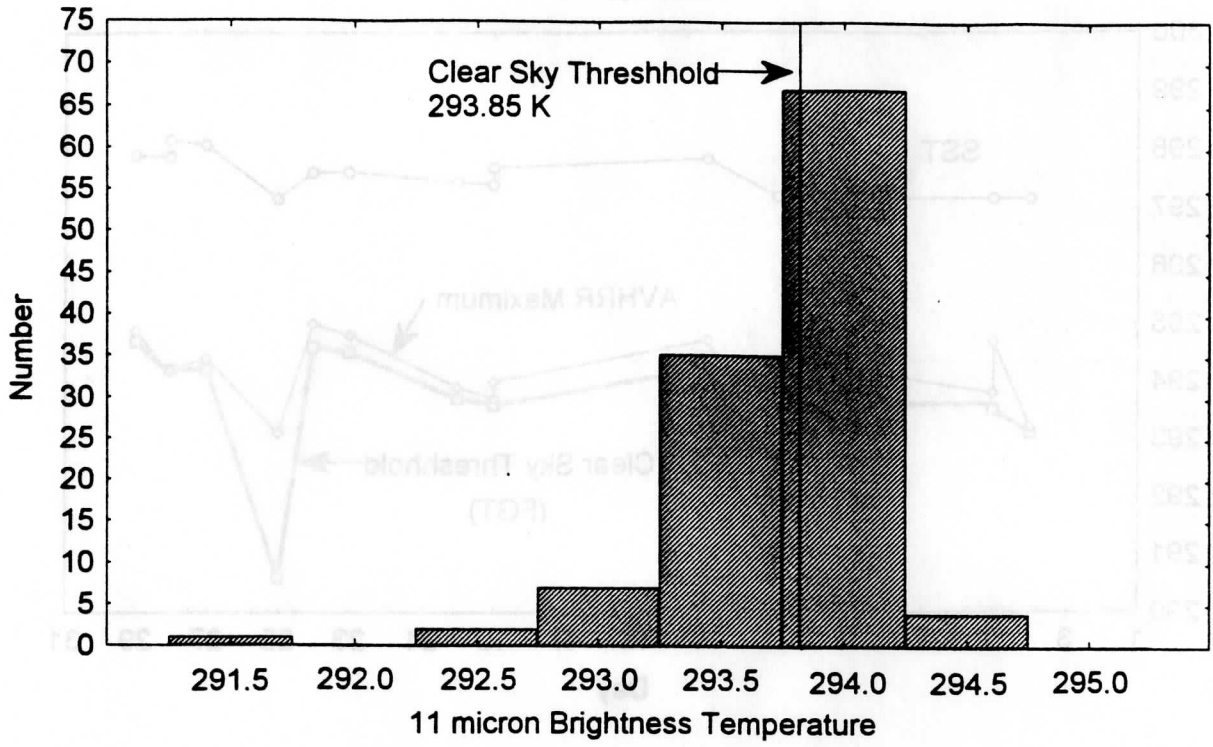
Time-Series of Clear Sky Threshhold
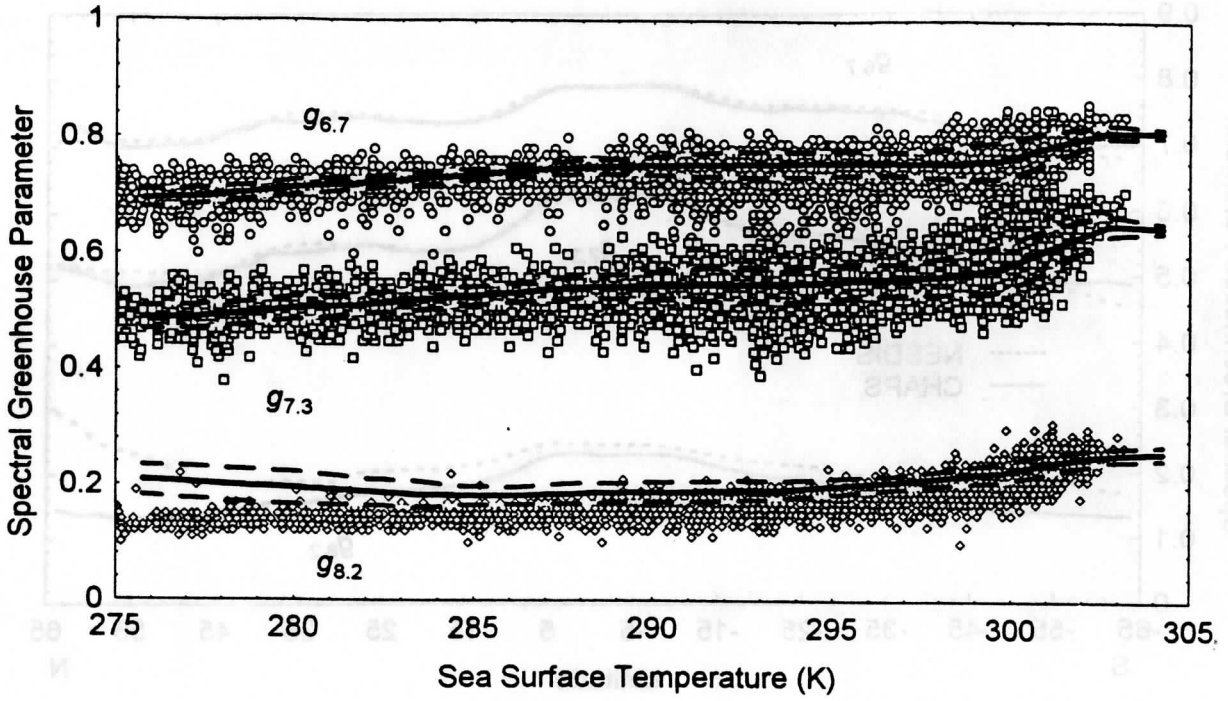January, 1994
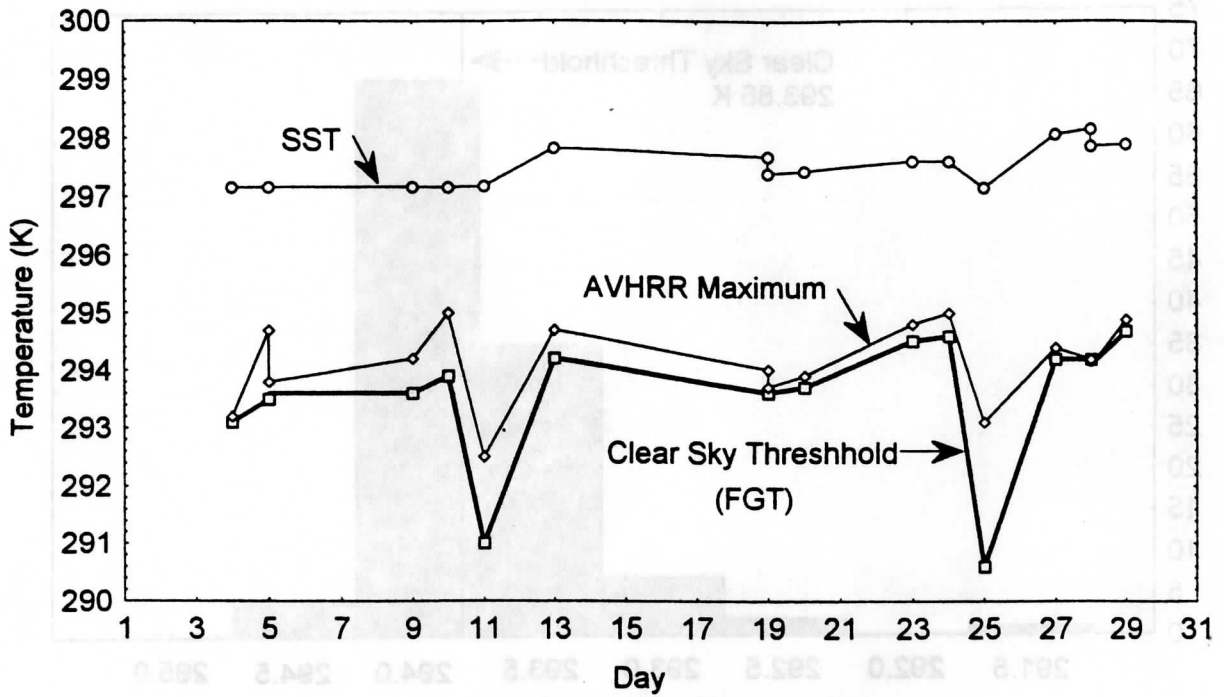
Generation of Regional Clear Sky Threshhold

For every collocated FOV in region

Compute first guess CST

AVHRR Ch 4 SD le 0.5 K — NO → Cloudy FOV

YES

For every pixel in FOV

DAY — NIGHT

AVHRR Ch 2 refl le 6.5 % — NO → Cloudy pixel

YES

AVHRR Ch 4 T_{bb} ge first guess CST — NO → Cloudy pixel

YES

Include pixel in regional CSH

Next pixel

Next FOV

Regional CST = CSH peak - AVHRR Ch 4 SD

Final Clear Sky Determination

For every collocated FOV in region

DAY — NIGHT

NO — Mean AVHRR Ch 2 refl le 6.5 %

NO — Mean AVHRR Ch 4 T_{bb} ge CST

NO — AVHRR Ch 3 SD le 0.5 K

NO — AVHRR Ch 4 SD le 0.5 K

NO — HIRS Ch 10 - Ch 8 T_{bb} lt -3.5 K

NO — Mean AVHRR Ch 4 - Ch 5 T_{bb} gt 0.5 K

NO — CO_2 slicing cloud height gt 500 mb

Clear FOV

Cloudy FOV

Next FOV

January Derived Spectral Greenhouse Parameter from CHAPS and NESDIS
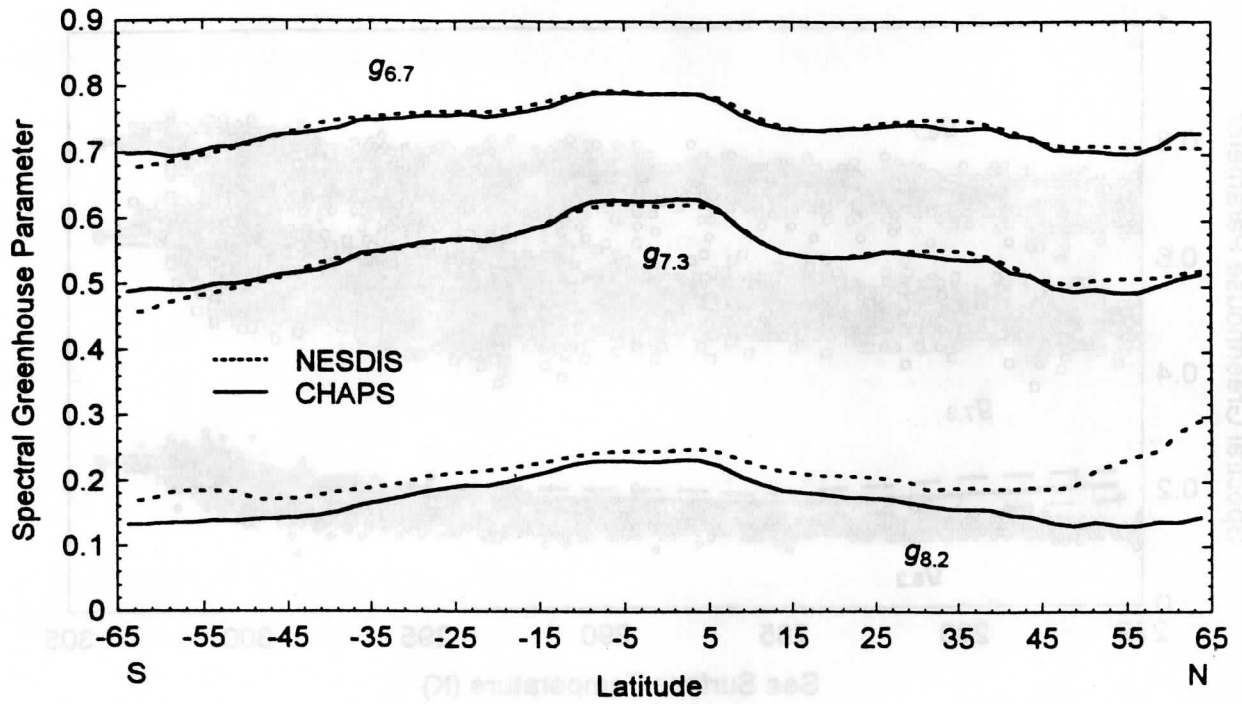
Derived Spectral Greenhouse Parameter from CHAPS and NESDIS
January Data

HIRS Clear Sky 8.2 micron Brightness Temperatures
January
Ocean Surfaces from 45 to 55 North Latitude

HIRS Clear Sky 8.2 micron Brightness Temperatures
January
Ocean Surfaces from 20 to 30 North Latitude
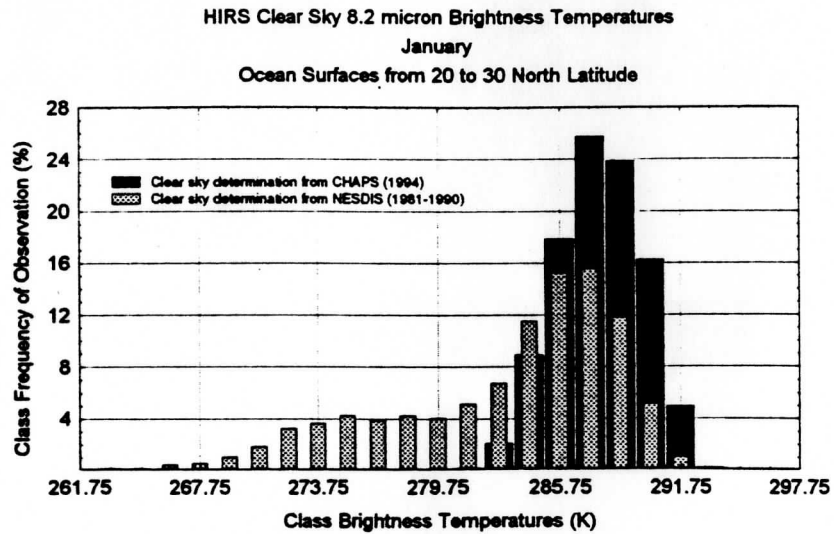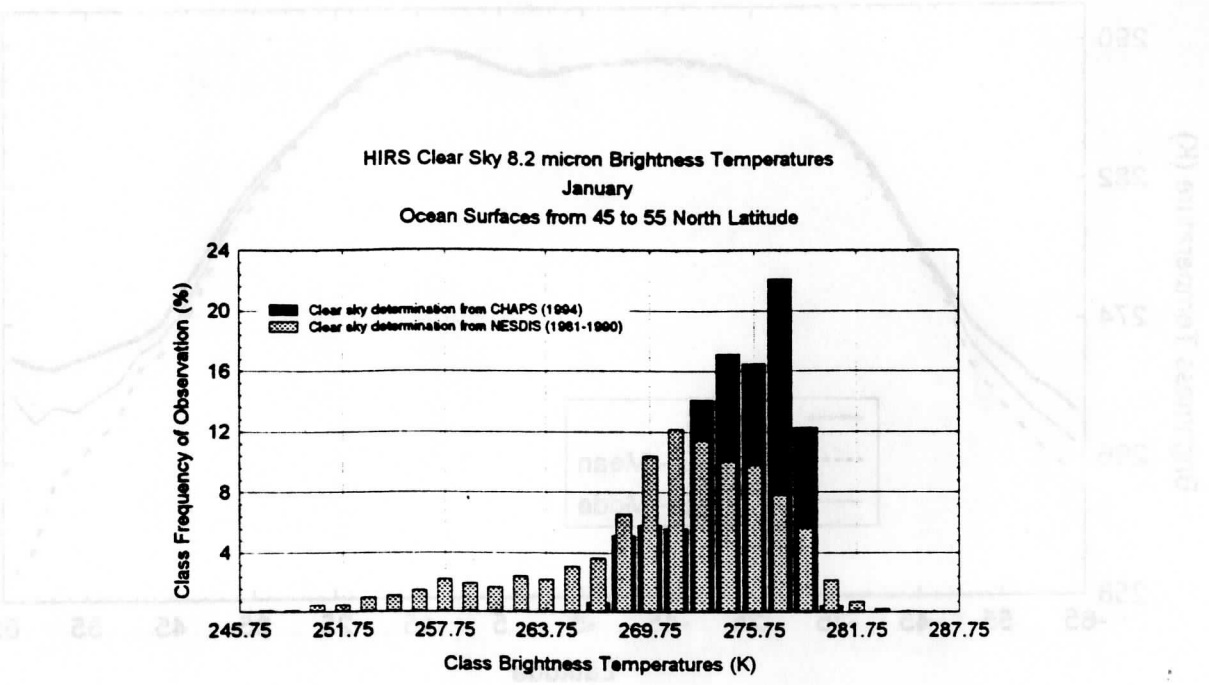
January Observed Brightness Temperatures from CHAPS and NESDIS
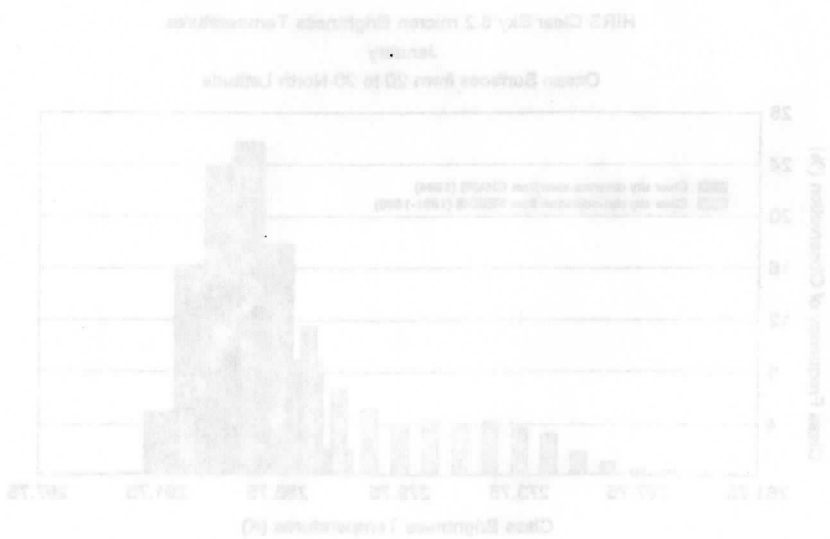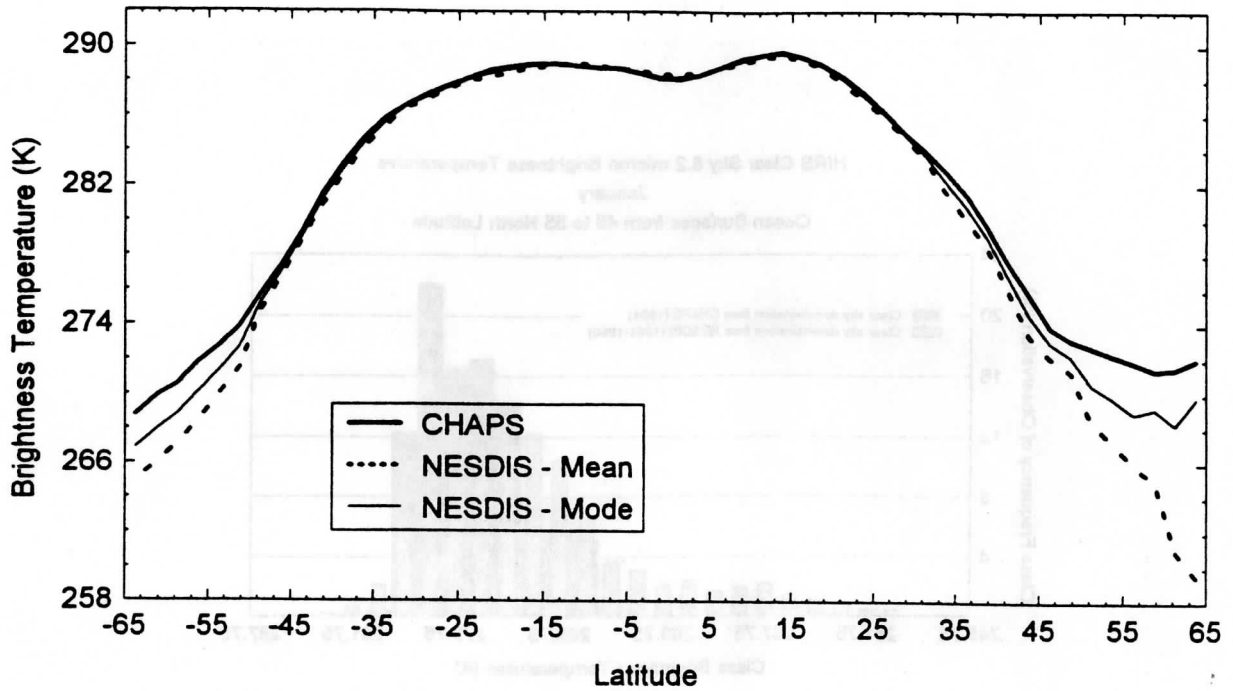
July 1993 Global Observations
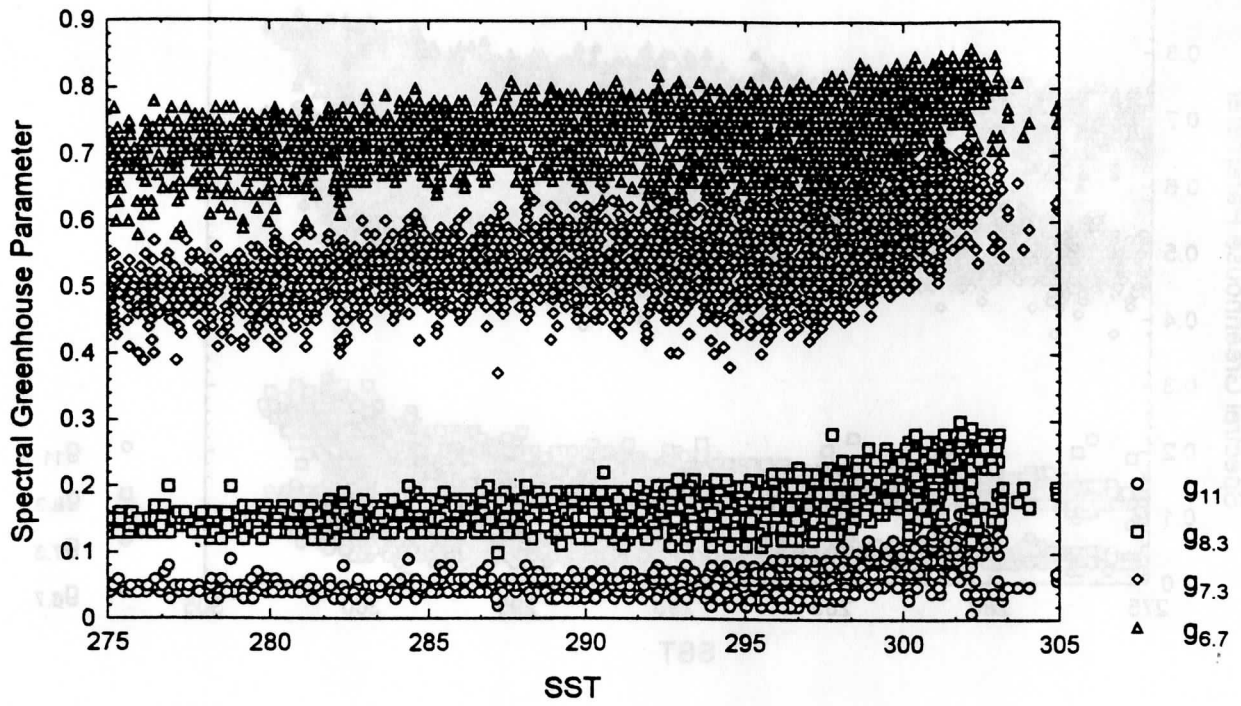
January 1994 Global Observations
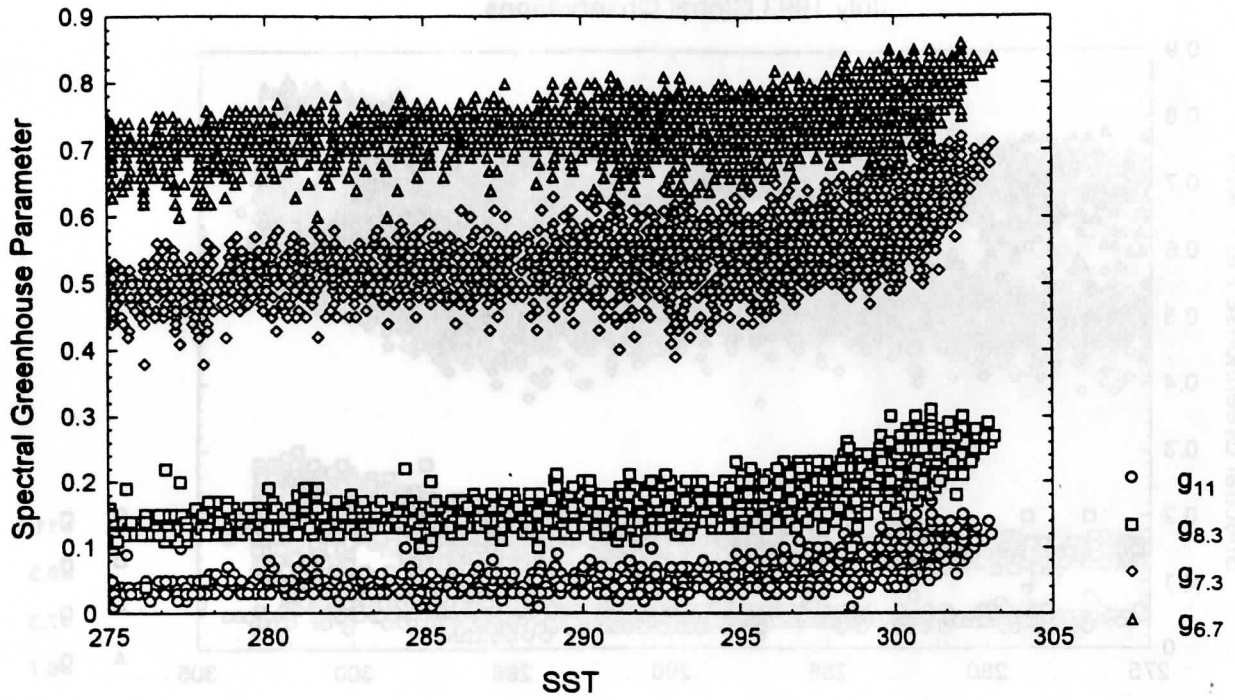
CHAPS Observed Brightness Temperatures from January 1994
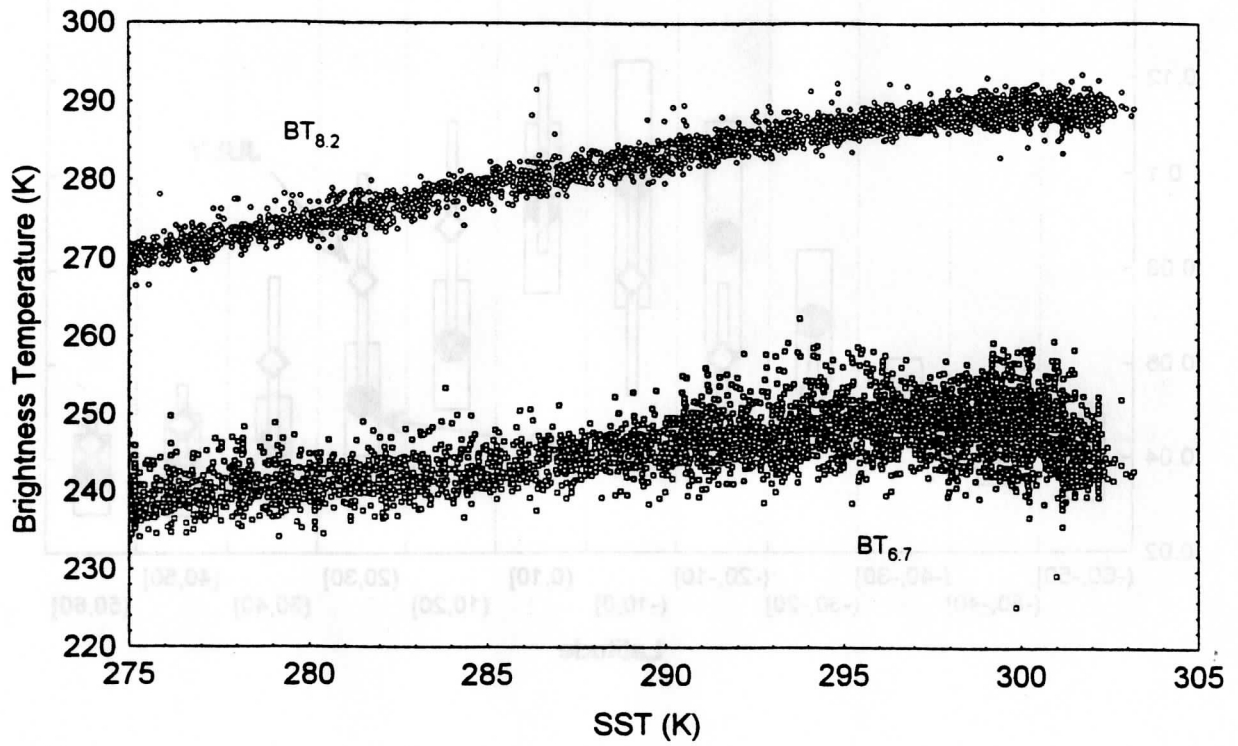
Spectral Greenhouse Parameter 11 microns
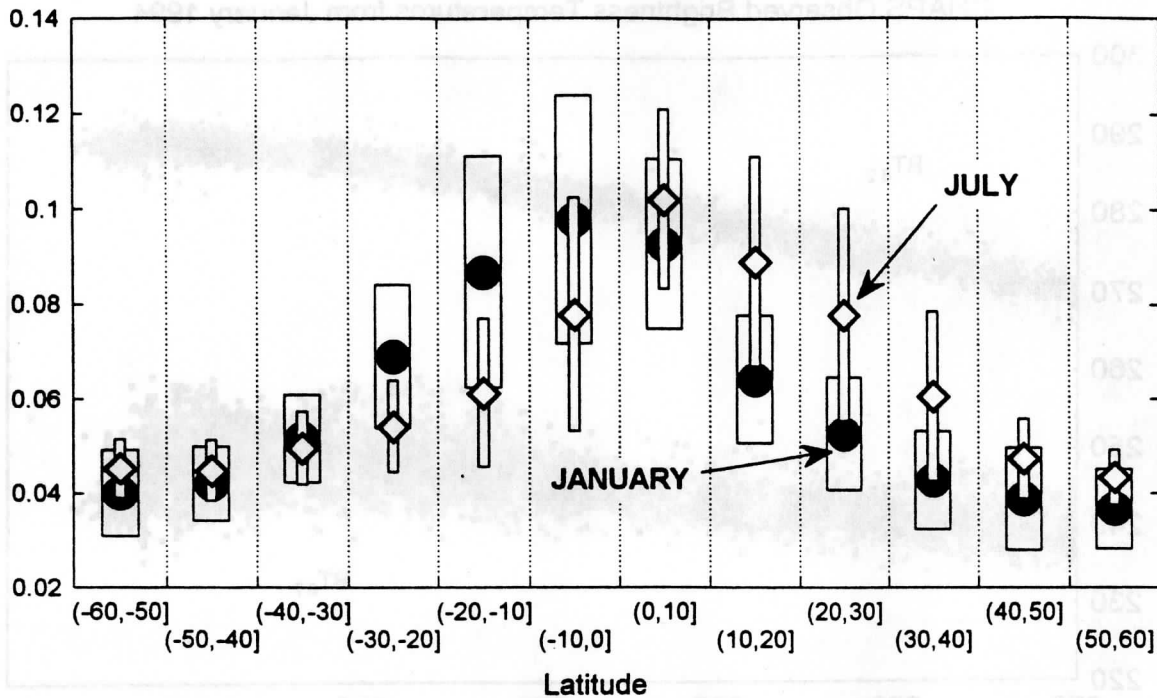
Spectral Greenhouse Parameter 8.2 microns
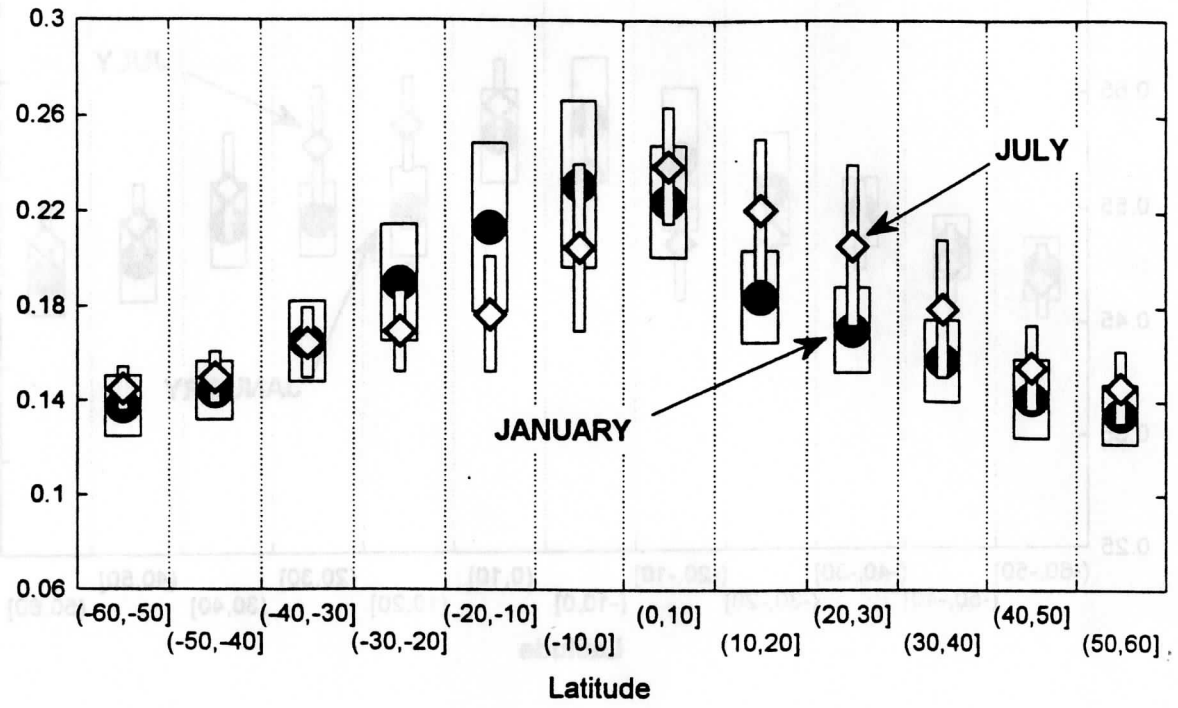
Spectral Greenhouse Parameter 7.3 microns
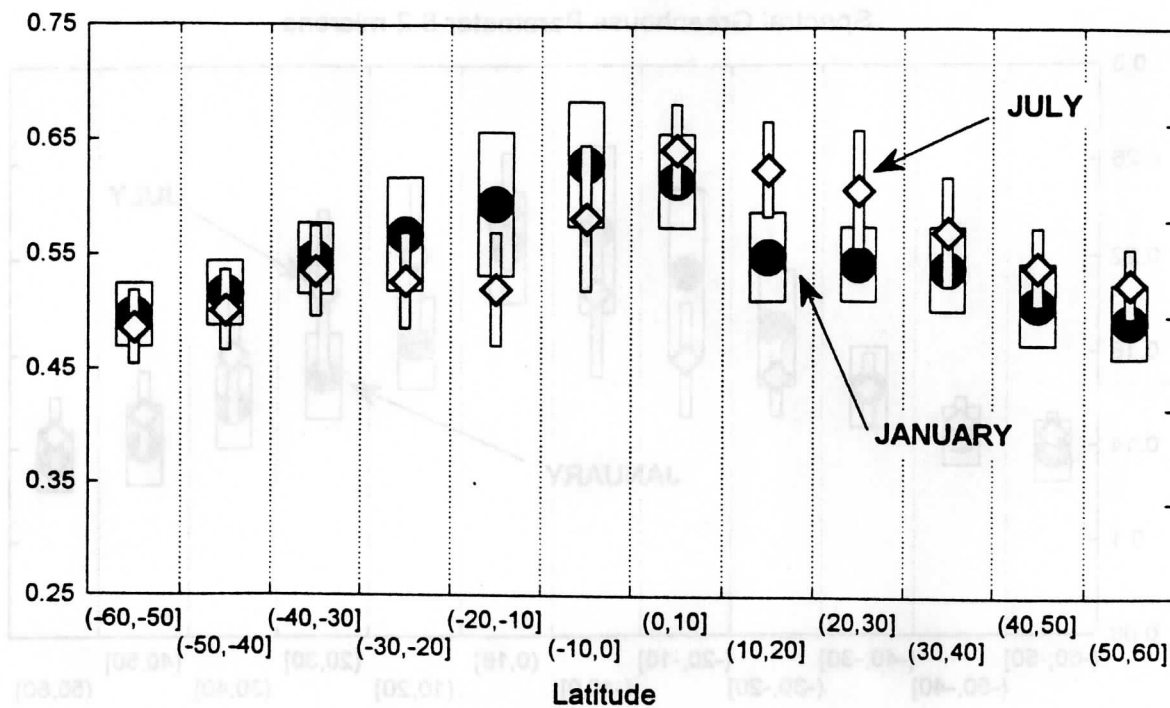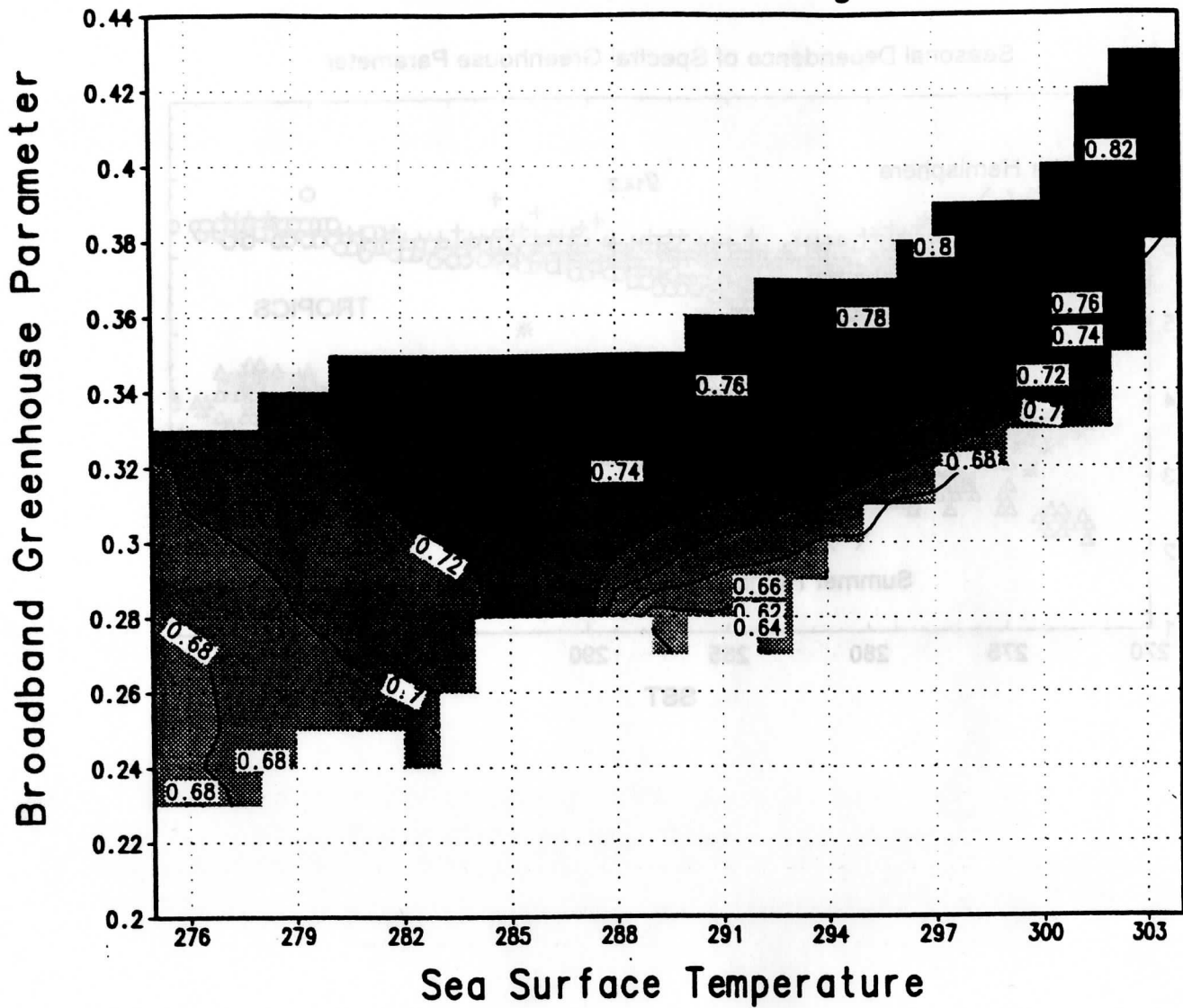
Spectral Greenhouse Parameter 6.7 microns
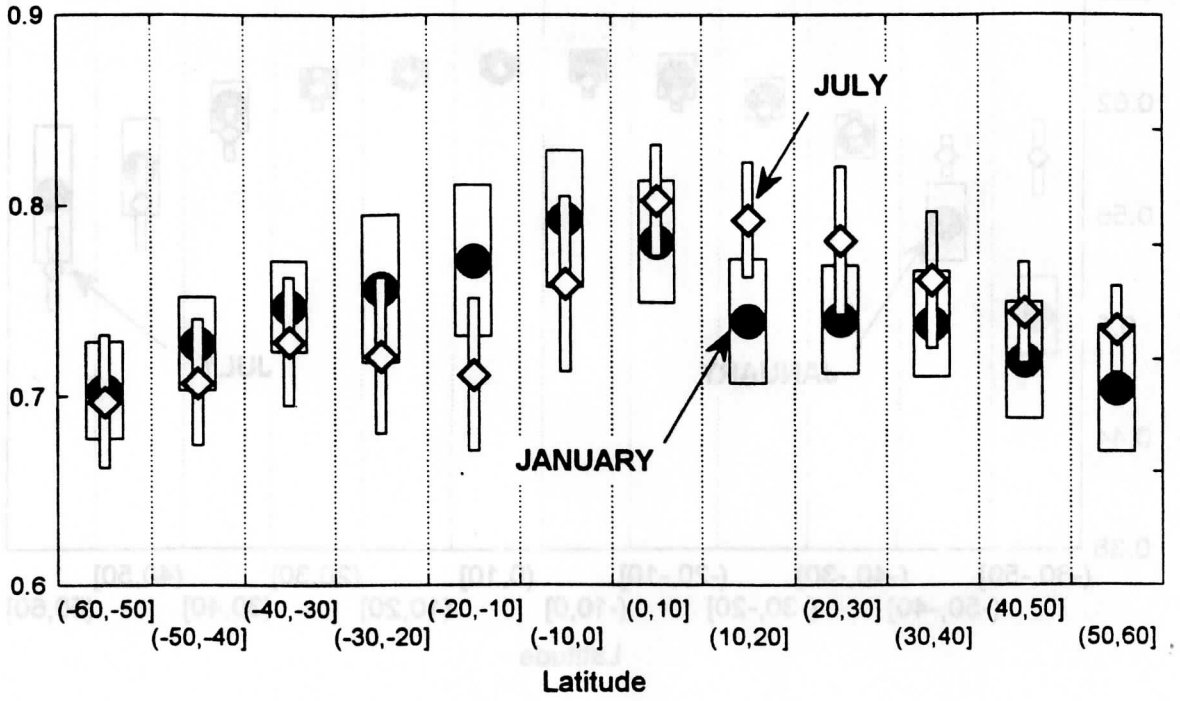
Spectral Greenhouse Parameter 14.2 microns (250 mb)
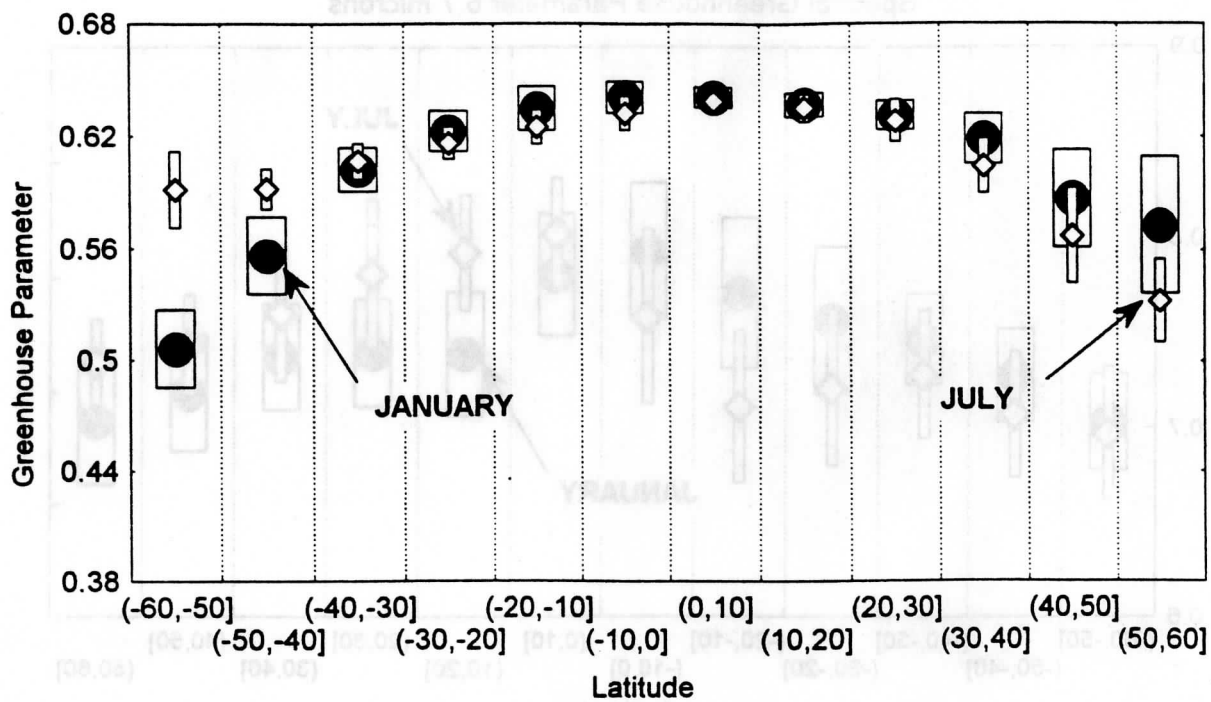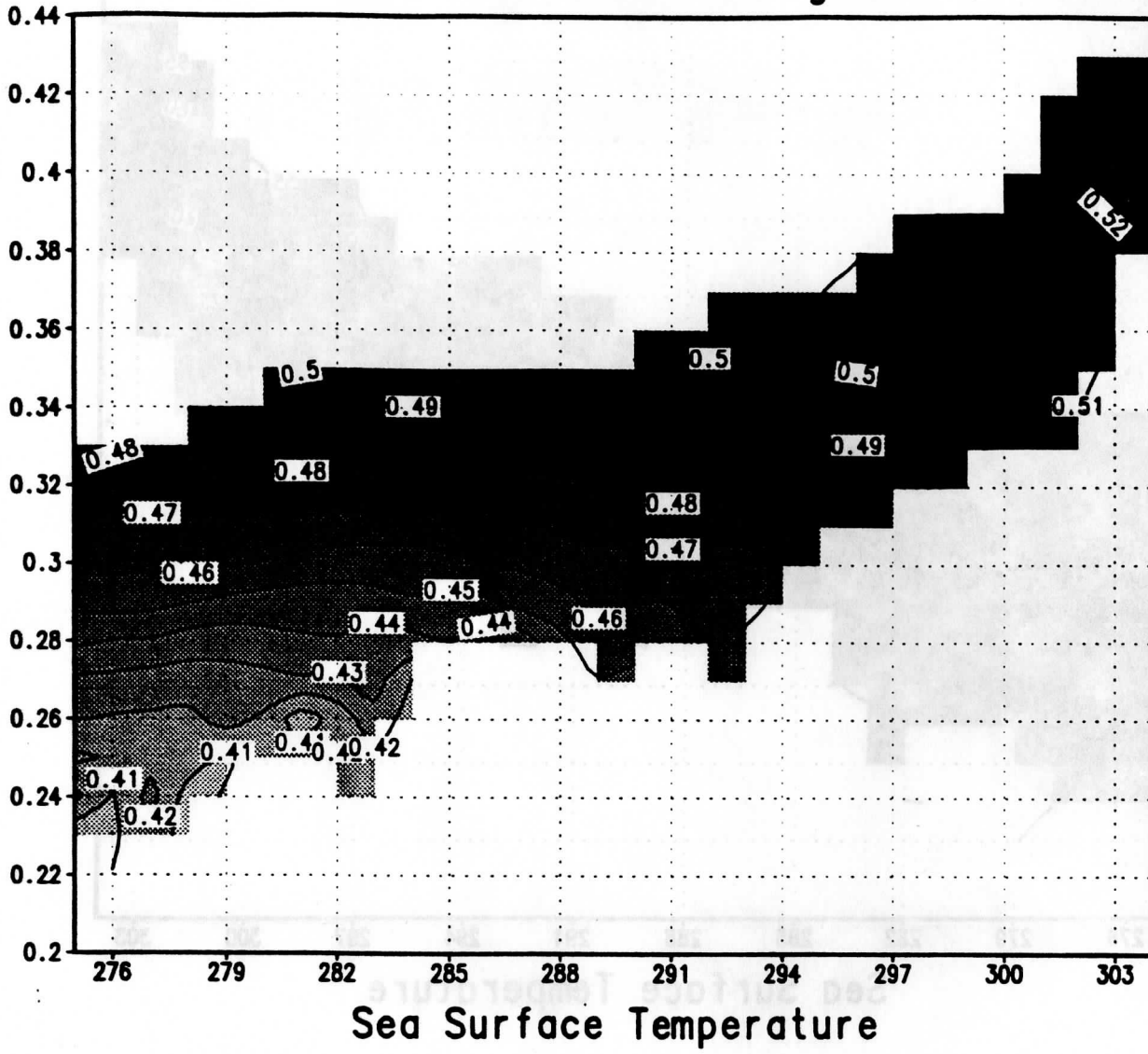
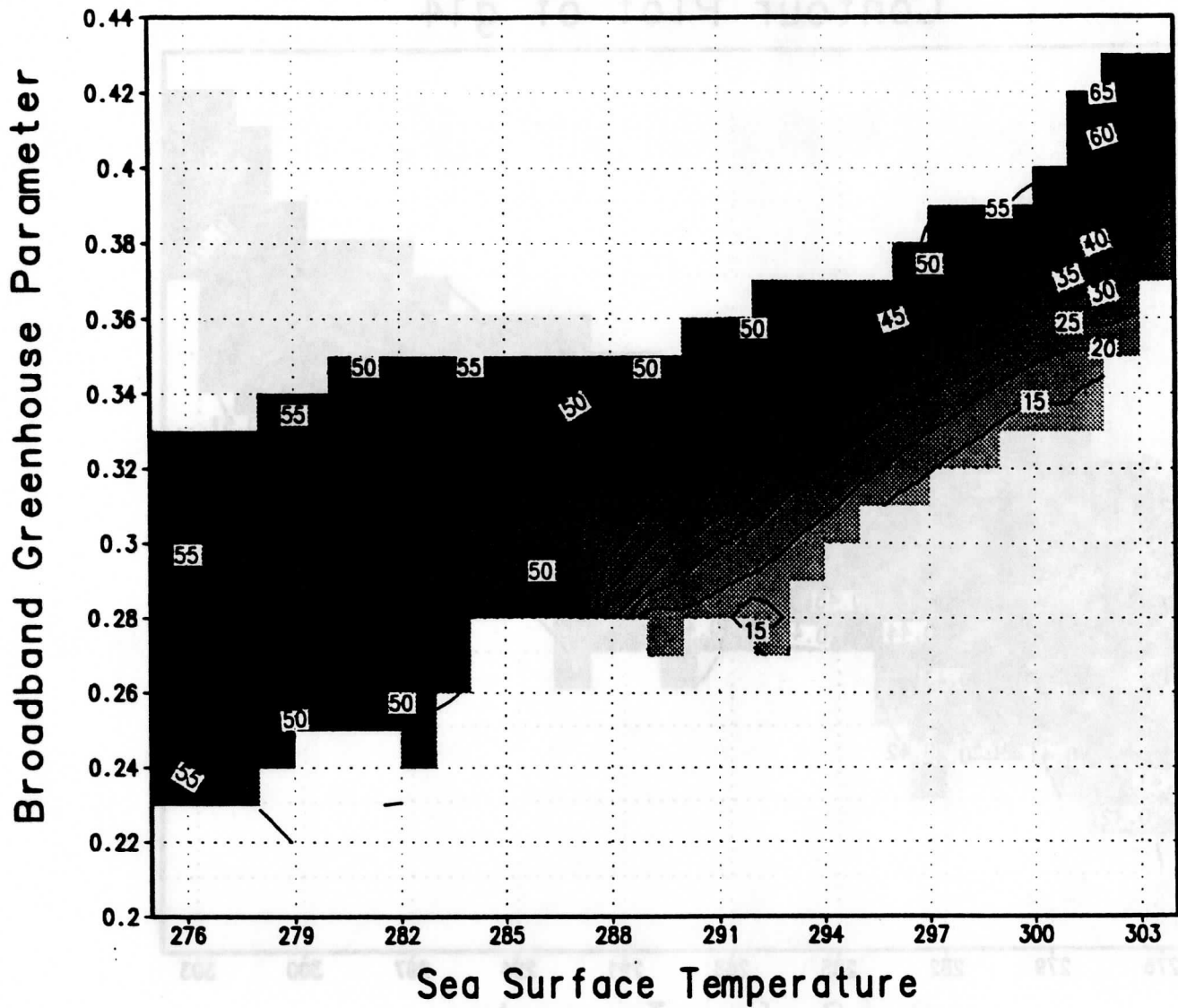Seasonal Dependence of Spectral Greenhouse Parameter
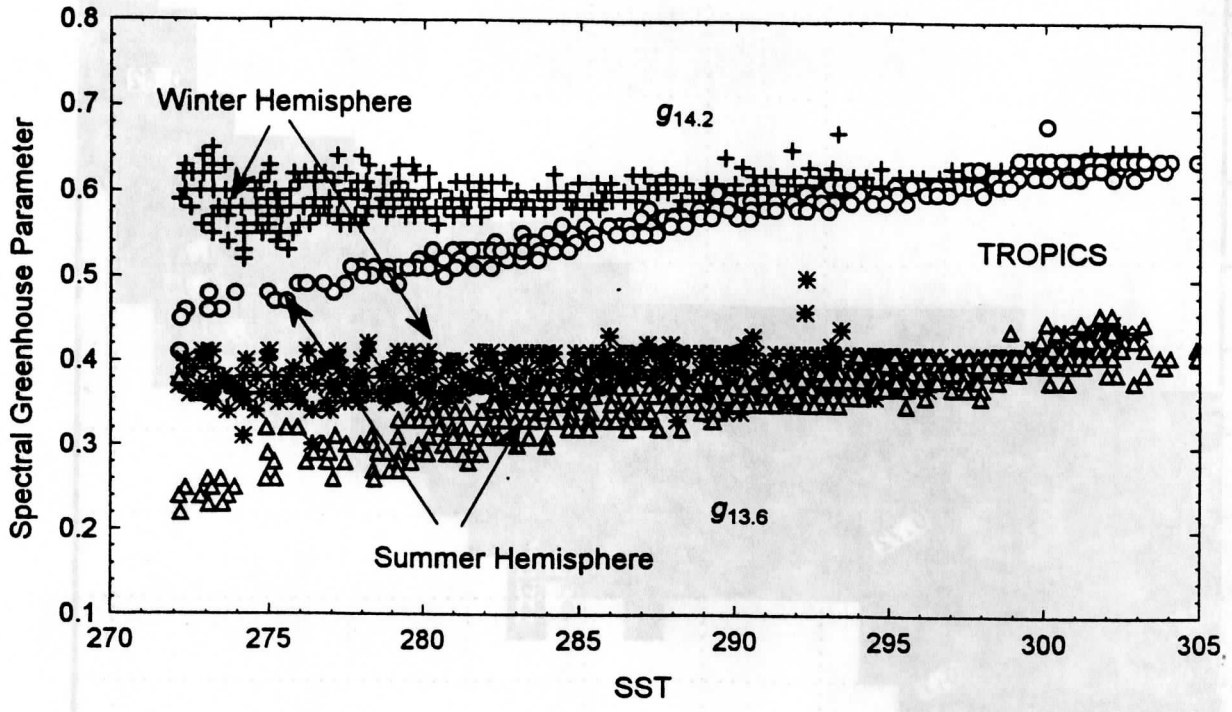
Contour Plot of g6.7

Contour Plot of g14

Contour Plot of UTH

Spectral Greenhouse Parameter from CHAPS, NESDIS, ERBE and GFDL